



**National Library  
of Canada**

**Bibliothèque nationale  
du Canada**

**Canadian Theses Service**

**Service des thèses canadiennes**

Ottawa, Canada  
K1A 0N4

## **NOTICE**

The quality of this microform is heavily dependent upon the quality of the original thesis submitted for microfilming. Every effort has been made to ensure the highest quality of reproduction possible.

If pages are missing, contact the university which granted the degree.

Some pages may have indistinct print especially if the original pages were typed with a poor typewriter ribbon or if the university sent us an inferior photocopy.

Reproduction in full or in part of this microform is governed by the Canadian Copyright Act, R.S.C. 1970, c. C-30, and subsequent amendments.

## **AVIS**

La qualité de cette microforme dépend grandement de la qualité de la thèse soumise au microfilmage. Nous avons tout fait pour assurer une qualité supérieure de reproduction.

S'il manque des pages, veuillez communiquer avec l'université qui a conféré le grade.

La qualité d'impression de certaines pages peut laisser à désirer, surtout si les pages originales ont été dactylographiées à l'aide d'un ruban usé ou si l'université nous a fait parvenir une photocopie de qualité inférieure.

La reproduction, même partielle, de cette microforme est soumise à la Loi canadienne sur le droit d'auteur, SRC 1970, c. C-30, et ses amendements subséquents.

THE UNIVERSITY OF ALBERTA

MESOSCALE VERTICAL VELOCITY FIELDS IN THE LEE OF THE  
ALBERTA ROCKIES: A CASE STUDY

BY

ROBERT W. HONCH



A THESIS

SUBMITTED TO THE FACULTY OF GRADUATE STUDIES AND  
RESEARCH IN PARTIAL FULFILMENT OF THE REQUIREMENTS FOR

THE DEGREE OF

MASTER OF SCIENCE

IN

METEOROLOGY

DEPARTMENT OF GEOGRAPHY

EDMONTON, ALBERTA

SPRING 1989



National Library  
of Canada

Bibliothèque nationale  
du Canada

Canadian Theses Service

Service des thèses canadiennes

Ottawa, Canada  
K1A 0N4

The author has granted an irrevocable non-exclusive licence allowing the National Library of Canada to reproduce, loan, distribute or sell copies of his/her thesis by any means and in any form or format, making this thesis available to interested persons.

The author retains ownership of the copyright in his/her thesis. Neither the thesis nor substantial extracts from it may be printed or otherwise reproduced without his/her permission.

L'auteur a accordé une licence irrévocable et non exclusive permettant à la Bibliothèque nationale du Canada de reproduire, prêter, distribuer ou vendre des copies de sa thèse de quelque manière et sous quelque forme que ce soit pour mettre des exemplaires de cette thèse à la disposition des personnes intéressées.

L'auteur conserve la propriété du droit d'auteur qui protège sa thèse. Ni la thèse ni des extraits substantiels de celle-ci ne doivent être imprimés ou autrement reproduits sans son autorisation.

ISBN 0-315-53011-1

THE UNIVERSITY OF ALBERTA

RELEASE FORM

NAME OF AUTHOR: ROBERT WAYNE HONCH

TITLE OF THESIS: MESOSCALE VERTICAL VELOCITY FIELDS IN THE  
LEE OF THE ALBERTA ROCKIES: A CASE STUDY

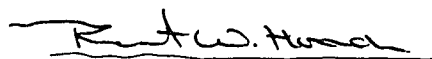
DEGREE: MASTER OF SCIENCE

YEAR THIS

DEGREE GRANTED: SPRING 1989

Permission is hereby granted to the UNIVERSITY OF ALBERTA LIBRARY to reproduce single copies of this thesis and to lend or sell such copies for private, scholarly or scientific research purposes only.

The author reserves other publication rights, and neither the thesis nor extensive extracts from it may be printed or otherwise reproduced without the author's written permission.

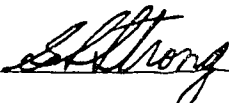
A handwritten signature in dark ink, appearing to read "Robert W. Honch", is written over a horizontal line.


7204 33<sup>rd</sup> Avenue  
Edmonton, Alberta  
T6K 1K3

Date: April 14, 1989

THE UNIVERSITY OF ALBERTA  
FACULTY OF GRADUATE STUDIES AND RESEARCH

The undersigned certify that they have read, and recommend to the Faculty of Graduate Studies and Research for acceptance, a thesis entitled Mesoscale Vertical Velocity Fields in the Lee of the Alberta Rockies: A Case Study submitted by Robert W. Honch in partial fulfilment of the requirements for the degree of Master of Science in Meteorology.

  
\_\_\_\_\_  
Supervisor

  
\_\_\_\_\_

  
\_\_\_\_\_

  
\_\_\_\_\_

Date: October 25, 1988

## ABSTRACT

The purpose of this study is to investigate the mesoscale vertical velocity and surface convergence fields during periods of summer convection in the lee of the Alberta Rockies. The study involves a limited review of the mesoscale, and is followed by a discussion on the importance of vertical motion in the atmosphere. The author pays particular attention to the mesoscale vertical velocity fields in the pre-thunderstorm environment.

Two common methods of calculating the mesoscale vertical velocity are described: the adiabatic technique, based on the first law of thermodynamics, and the kinematic technique, based on the conservation of mass. The advantages and disadvantages of both methods are examined. This is followed by a discussion on the importance of surface convergence in the lower troposphere. The author explores the primary role of surface convergence in the pre-thunderstorm environment, and describes a simple method of measurement. The theoretical relationship between vertical velocity and low-level convergence is also examined.

Embedded throughout this discussion is the premise that under certain conditions, strong vertical lift can result in the liberation of latent instability in the lower atmosphere. To facilitate this postulate, a brief review of static stability and methods of measuring stability are included.

The case study uses a mesoscale data set obtained in the summer of 1985 during the Limestone Mountain Experiment (LIMEX-85). A brief description of this mesoscale experiment, conducted by the Alberta Research Council, is included.

The case study involves a brief diagnostic assessment of the synoptic scale environment prior to and during a thunderstorm event. Attention is focused on the dynamic features that tend to determine the synoptic scale vertical motion in the atmosphere. The static stability of the pre-thunderstorm environment is assessed over the mesoscale network. The development, evolution and motion of thunderstorms are then examined using PPI summaries from an S-band research radar. Cloud patterns in both the pre-thunderstorm and thunderstorm period are observed using satellite imagery. Finally, the mesoscale vertical velocity and divergence fields are diagnosed. Observations are made on the temporal and spatial continuity of these fields and their inter-relationship.

## **ACKNOWLEDGEMENTS**

In the field of scientific research it has been wisely written that we advance upon the shoulders of our predecessors. This mesoscale research study is based upon the previous works of several scientists who are acknowledged throughout this dissertation. In particular, I would like to acknowledge Dr. Geoff S. Strong who provided expert advice and constructive criticism. It was a privilege to work with Dr. Strong and have him take time from a busy schedule to serve on the examining committee.

Professors E.P. Lozowski and J.D. Wilson of the Meteorology Division and Dr. G. Swaters of the Mathematics Department also served on the examining committee. I am grateful for the suggestions and encouragement they offered and was honoured to have them serve on the committee.

The opportunity to pursue this study was rendered by the Atmospheric Environment Service. The moral support and understanding of Mr. Hans VanLeeuwen and Mr. Rick Tone was appreciated during a difficult final year.

The data and computer resources were furnished by the management of the Resource Technologies Division of the Alberta Research Council. Valuable computer assistance was provided by Mark Johnson, Bill Korendyk, Robert Booth and Andrew Krol.

I sincerely believe that none of this would have been possible without the encouragement and love of my wife and friend Joanne. She has truly been a gracious gift from God and it is to her that I dedicate this work.



# Contents

|          |   |           |
|----------|---|-----------|
| <b>1</b> | <b>Introduction</b>   | <b>1</b>  |
| 1.1      | The Mesoscale . . . . .   | 1         |
| 1.2      | Vertical Motion in the Atmosphere . . . . .   | 5         |
| 1.2.1    | Mesoscale Vertical Velocity Fields in the Pre-Thunderstorm<br>Environment . . . . . | 8         |
| 1.3      | Divergence in the Lower Troposphere . . . . .                                       | 9         |
| 1.3.1    | The Relationship Between Vertical Velocity and Divergence .                         | 11        |
| 1.3.2    | The Role of Surface Convergence in the Pre-Thunderstorm<br>Environment . . . . .    | 11        |
| 1.4      | The Objectives of this Study . . . . .  | 13        |
| <b>2</b> | <b>Data Sources and Analysis Procedures</b>   | <b>16</b> |
| 2.1      | The LIMEX-85 Data Set . . . . .   | 16        |
| 2.1.1    | Spatial Resolution of the LIMEX-85 Data . . . . .                                   | 16        |
| 2.1.2    | Temporal Resolution of the LIMEX-85 Upper Air Data . . .                            | 18        |
| 2.1.3    | Temporal Resolution of the LIMEX-85 Surface Data . . . . .                          | 18        |
| 2.1.4    | Other Data Sources . . . . .  | 19        |
| 2.1.5    | Remarks . . . . .   | 19        |

|          |  |           |
|----------|--|-----------|
| 2.2      | Data Analysis and Fields Investigated . . . . .                      | 20        |
| 2.3      | Methods of Measuring Vertical Velocity . . . . .                     | 21        |
| 2.3.1    | The Adiabatic Method . . . . .                                       | 22        |
| 2.3.2    | The Kinematic Method . . . . .                                       | 25        |
| 2.3.3    | Comparison of the Adiabatic and Kinematic Techniques . . .           | 26        |
| 2.3.4    | The Modified Adiabatic Method of Computing Vertical Velocity         | 27        |
| 2.3.5    | Importance of the Horizontal Temperature Advection Term .            | 31        |
| 2.3.6    | Disadvantages of the Modified Adiabatic Technique . . . . .          | 33        |
| 2.4      | Method of Measuring the Divergence . . . . .                         | 35        |
| 2.4.1    | The Significance of Mesoscale Surface Convergence . . . . .          | 38        |
| 2.5      | Measuring the Stability . . . . .                                    | 39        |
| 2.5.1    | Static Stability . . . . .   | 39        |
| 2.5.2    | Stability Indices . . . . .  | 39        |
| 2.6      | Mesoscale Objective Map Analysis . . . . .                           | 43        |
| 2.6.1    | Methodology . . . . .  | 43        |
| 2.6.2    | Objective Map Analysis of LIMEX-85 Data . . . . .                    | 48        |
| 2.7      | Summary . . . . .  | 51        |
| <b>3</b> | <b>Error Analysis</b>  | <b>52</b> |
| 3.1      | Definitions . . . . .  | 52        |
| 3.2      | LIMEX-85 Data Uncertainty . . . . .                                  | 53        |
| 3.3      | Uncertainty of Upper Air Data . . . . .                              | 53        |
| 3.4      | Uncertainty in the Modified Adiabatic Vertical Velocity Computations | 58        |

|          |   |            |
|----------|---|------------|
| 3.5      | Uncertainty in Horizontal Divergence Calculations . . . . . | 60         |
| <b>4</b> | <b>Case Study: 11 July 1985</b>                             | <b>61</b>  |
| 4.1      | The Synoptic Situation . . . . .                            | 61         |
| 4.2      | Mesoscale Stability Analysis . . . . .                      | 69         |
| 4.3      | S-band Radar PPI Summaries . . . . .                        | 72         |
| 4.4      | Mesoscale Analysis of Satellite Imagery . . . . .           | 86         |
| 4.5      | Mesoscale Vertical Motion Fields . . . . .                  | 88         |
| 4.5.1    | Summary . . . . .   | 101        |
| 4.6      | Meso-beta 800 mb Divergence Fields . . . . .                | 102        |
| 4.7      | Meso-gamma Surface Divergence Fields . . . . .              | 102        |
| 4.7.1    | The Utility of Existing Sub-Synoptic Data Sources . . . . . | 106        |
| 4.7.2    | Summary . . . . .   | 107        |
| <b>5</b> | <b>Conclusions and Recommendations</b>                      | <b>109</b> |
| 5.1      | Summary and Conclusions . . . . .                           | 109        |
| 5.2      | Recommendations . . . . .                                   | 111        |
|          | <b>Bibliography</b>   | <b>113</b> |
| <b>A</b> | <b>Assessment of Spatial Analysis Scheme</b>                | <b>117</b> |
| A.1      | Method . . . . .  | 117        |
| A.2      | Results . . . . .   | 119        |
| A.3      | Conclusions . . . . .                                       | 125        |

## List of Figures

|     |   |    |
|-----|---|----|
| 2.1 | LIMEX-85 station sites . . . . .  | 17 |
| 2.2 | The modified adiabatic method . . . . .                                 | 30 |
| 2.3 | A simple analysis grid for estimating divergence . . . . .              | 36 |
| 2.4 | Stability of a physical system . . . . .                                | 40 |
| 2.5 | Potential stability of a physical system . . . . .                      | 41 |
| 2.6 | Determining the value of the weighting function . . . . .               | 44 |
| 2.7 | Graph of distance-dependent weight factor . . . . .                     | 45 |
| 2.8 | Location of LIMEX-85 mesoscale analysis grid . . . . .                  | 49 |
| 2.9 | LIMEX-85 mesoscale analysis grid . . . . .                              | 50 |
| 3.1 | Error in calculating the adiabatic vertical velocity . . . . .          | 56 |
| 3.2 | Error in calculating the adiabatic vertical velocity . . . . .          | 57 |
| 4.1 | CMC upper-troposphere objective analyses for July 11, 1985 . . . . .    | 63 |
| 4.2 | CMC lower-troposphere objective analyses for July 11, 1985 . . . . .    | 64 |
| 4.3 | 500 mb absolute vorticity analyses for July 11, 1985 . . . . .          | 66 |
| 4.4 | CMC synoptic analyses for 0000 UTC July 12, 1985 . . . . .              | 68 |
| 4.5 | Lifted Index objective analysis, valid 1500 UTC July 11, 1985 . . . . . | 70 |
| 4.6 | Lifted Index objective analysis, valid 1800 UTC July 11, 1985 . . . . . | 71 |

|      |   |     |
|------|---|-----|
| 4.7  | S-band radar PPI summary for 2200 UTC July 11, 1985 . . . . .         | 73  |
| 4.8  | S-band radar PPI summary for 2230 UTC July 11, 1985 . . . . .         | 74  |
| 4.9  | S-band radar PPI summary for 2300 UTC July 11, 1985 . . . . .         | 75  |
| 4.10 | S-band radar PPI summary for 2330 UTC July 11, 1985 . . . . .         | 76  |
| 4.11 | S-band radar PPI summary for 0000 UTC July 12, 1985 . . . . .         | 77  |
| 4.12 | S-band radar PPI summary for 0030 UTC July 12, 1985 . . . . .         | 78  |
| 4.13 | S-band radar PPI summary for 0100 UTC July 12, 1985 . . . . .         | 79  |
| 4.14 | S-band radar PPI summary for 0130 UTC July 12, 1985 . . . . .         | 80  |
| 4.15 | S-band radar PPI summary for 0200 UTC July 12, 1985 . . . . .         | 81  |
| 4.16 | S-band radar PPI summary for 0230 UTC July 12, 1985 . . . . .         | 82  |
| 4.17 | S-band radar PPI summary for 0300 UTC July 12, 1985 . . . . .         | 83  |
| 4.18 | S-band radar PPI summary for 0330 UTC July 12, 1985 . . . . .         | 84  |
| 4.19 | Time series of NOAA satellite imagery for July 11, 1985 . . . . .     | 87  |
| 4.20 | Mesoscale vertical velocity fields for 1700 UTC July 11, 1985 . . . . | 90  |
| 4.21 | Serial soundings from CARL and CARM . . . . .                         | 91  |
| 4.22 | Mesoscale vertical velocity fields for 1900 UTC July 11, 1985 . . . . | 92  |
| 4.23 | Mesoscale vertical velocity fields for 2100 UTC July 11, 1985 . . . . | 94  |
| 4.24 | Mesoscale vertical velocity fields for 2300 UTC July 11, 1985 . . . . | 95  |
| 4.25 | Serial soundings from Mountaineer Lodge . . . . .                     | 96  |
| 4.26 | Mesoscale vertical velocity fields for 0100 UTC July 12, 1985 . . . . | 97  |
| 4.27 | Serial soundings from Caroline, 1604 to 2001 UTC . . . . .            | 100 |
| 4.28 | 800 mb divergence fields for July 11, 1985 . . . . .                  | 103 |
| 4.29 | Surface divergence fields for July 11, 1985 . . . . .                 | 105 |

|   |     |
|---|-----|
| 4.30 Surface divergence (LIMEX-85 versus AES) . . . . .           | 107 |
| A.1 Spatial Analyses of Sinusoidal Equation ( $n = 1$ ) . . . . . | 120 |
| A.2 Spatial Analyses of Sinusoidal Equation ( $n = 2$ ) . . . . . | 122 |
| A.3 Spatial Analyses of Sinusoidal Equation ( $n = 3$ ) . . . . . | 124 |

## List of Tables

|     |   |    |
|-----|---|----|
| 1.1 | Horizontal scales of motion . . . . .                                   | 4  |
| 1.2 | Characteristic magnitudes of vertical velocity and divergence . . . .   | 6  |
| 2.1 | Characteristic Lifted Index values . . . . .                            | 43 |
| 3.1 | Estimated RMS error in the SESAME rawinsonde data . . . . .             | 54 |
| 3.2 | Estimated RMS error in the SESAME rawinsonde wind data . . . .          | 55 |
| 3.3 | Uncertainties in modified adiabatic vertical velocity estimations . . . | 58 |

## **ABBREVIATIONS USED IN THIS DOCUMENT**

|                    |   |
|--------------------|---|
| AES                | Atmospheric Environment Service (of Environment Canada)     |
| AHP                | ARC Hail Project, Red Deer, Alberta                         |
| ARC                | Alberta Research Council, Edmonton, Alberta                 |
| AVE                | Area Variability Experiment (SESAME)                        |
| °C                 | degrees Celsius   |
| CB                 | cumulonimbus cloud  |
| CMC                | Canadian Meteorological Centre (of AES)                     |
| cm s <sup>-1</sup> | centimetres/second  |
| GMT                | Greenwich Mean Time, abbreviated Z, now known as UTC        |
| K                  | degrees Kelvin  |
| km                 | kilometre(s)  |
| LI                 | Lifted Index  |
| LIMEX-85           | Limestone Mountain Experiment 1985 (of AHP)                 |
| mb                 | millibar(s)   |
| MDT                | Mountain Daylight Time (UTC – 6 hours)                      |
| m s <sup>-1</sup>  | metre(s)/second   |
| NCAR               | National Centre for Atmospheric Research, Boulder, Colorado |
| NOAA               | National Oceanic and Atmospheric Administration             |
| NVA                | negative vorticity advection                                |
| PPI                | plan-position indicator                                     |
| PVA                | positive vorticity advection                                |



|                            |  |
|----------------------------|--|
| <b>RMS</b>                 | root-mean-square (error)                             |
| <b>s<sup>-1</sup></b>      | 1./second  |
| <b>SESAME</b>              | Severe Environmental Storms and Mesoscale Experiment |
| <b><math>\theta</math></b> | potential temperature (theta)                        |
| <b>UTC</b>                 | Universal Coordinated Time, formerly GMT or Z        |
| <b>Z</b>                   | abbreviation on maps for UTC                         |

## Chapter 1

### Introduction

#### 1.1 The Mesoscale

Two and a half centuries ago George Hadley (1735) followed a rational argument endeavouring to explain the causes of the trade winds. The early pioneers of meteorology advanced upon his shoulders. In the years that followed, new theories evolved, meteorological data networks were expanded, and technological advances served as a spring board to accelerate the science of meteorology. In spite of this growth, progress was slow in relating theory to the complexities of the real atmosphere. This slow progress is reflected in the following statement by Carl-Gustaf Rossby (1942):

*The science of meteorology does not yet have a universally accepted, coherent picture of the mechanics of the general circulation of the atmosphere.*

Rossby gives several possible reasons for this apparent lack of understanding.

- *“Observational data from the upper atmosphere still are very incomplete.”* Today, there still appears to be a lack of data of sufficient resolution and accuracy

to faithfully diagnose the atmosphere, especially mesoscale features.

- *“Our theoretical tools for the analysis of atmospheric motions are inadequate.”*
- *“In ordinary laboratory physics it is always possible to set up an experiment, vary one factor at a time, and study the consequences. Meteorologists have to contend with such variations as nature may offer, and these variations are seldom so clean-cut as to permit the establishment of well-defined relationships between cause and effect.”*

The complexity of the atmosphere becomes apparent when one considers its physical characteristics. In simple terms, the atmosphere can be envisioned as a turbulent stratified fluid, influenced by strong thermal or radiational effects. This fluid is moving over a complex topographical surface; and to further complicate matters, that surface is rotating. A full explanation of the mechanics of this complicated fluid is not a trivial matter.

In an attempt to understand the complicated motion of the atmosphere, Ligda (1951) introduced the traditional threefold classification of macroscale, mesoscale, and microscale. This partitioning is based on the concept that individual parts are more easily analyzed, diagnosed, and investigated. Once we understand the parts, we will be better equipped to comprehend the whole. In the atmosphere, these partitions are motion systems, and the method of classification is based upon the time and space scale of the motion system.

The classification of atmospheric scales of motion, from the synoptic scale, through the mesoscale to the microscale, appears to be an ongoing and ever chang-

ing element of meteorology. Since 1951, when the term *mesoscale* was initially introduced by Lidgda, several classification schemes have been proposed. The proposed schemes are based on the characteristic time and space scale of various motion systems. Two of the more popular schemes accepted by mesoscale meteorologists were proposed by Orlanski (1975) and Fujita (1981). Both have quantized Lidga's single mesoscale into several subdivisions. A comparison of these three classification schemes is presented in Table 1.1. Orlanski subdivided the single mesoscale into the meso- $\alpha$ , meso- $\beta$ , and meso- $\gamma$  scales. Fujita redefined the entire spectrum of motions. All three methods of classification are based on orders of magnitude of the space and time scales involved.

It is important to realize that these classification schemes do not imply that the atmosphere can be quantized into discrete scales. In fact, the entire extent of atmospheric motions is a continuum. This is eloquently phrased by L.F. Richardson who, in 1922, wrote:

*Big whirls have little whirls that feed on their velocity  
and little whirls have lesser whirls, and so on to viscosity.*

Dr. K. A. Emanuel (1986) appears to take a dim view of the high degree of subdivision appearing in the current literature. He writes:

*Today it seems that the degree of quantization of the mesoscale is limited  
only by the human imagination and the length of the Greek alphabet.*

Both Orlanski and Fujita base their classification schemes on an order of magnitude argument. These "cut and dried" schemes are somewhat arbitrary and

| TYPE OF FEATURE               | APPROX. LENGTH SCALE | LIGDA 1951 | ORLANSKI 1975  | FUJITA 1981                  |
|-------------------------------|----------------------|------------|----------------|------------------------------|
| LONG WAVE                     | 40,000 km<br>↓       | SYNOPTIC   | MACRO          | $\alpha$                     |
| CYCLONE<br>or<br>ANTI-CYCLONE | 10,000 km<br>↓       |            | MESO $\alpha$  | —MASO—<br>(macro)<br>$\beta$ |
|                               | 1,000 km<br>↓        |            |                |                              |
| MESOCYCLONE<br>MESOHIGH       | 100 km<br>↓          | MESO       | MESO $\beta$   | $\alpha$                     |
| THUNDERSTORM                  | 10 km<br>↓           |            | MESO $\gamma$  | —MESO—<br>(meso)<br>$\beta$  |
| TORNADO                       | ↓<br>1 km            | MICRO      | MICRO $\alpha$ | $\alpha$                     |
| DUSTDEVIL                     | ↓<br>100 m           |            | MICRO $\beta$  | —MISO—<br>(micro)<br>$\beta$ |
|                               | ↓<br>10 m            |            | MICRO $\gamma$ | $\alpha$                     |
|                               | ↓<br>1 m             |            |                | —MOSO—<br>(- - -)<br>$\beta$ |
| SUCTION VORTEX                |                      |            |                | MUSO<br>(- - -)              |

Table 1.1: The horizontal scales of atmospheric disturbances in relation to the scales proposed by Ligda (1951), Orlanski (1975), and Fujita (1981). Note that a cyclone is the parent storm of a mesocyclone, which in turn is the parent storm of a tornado, an inducer of the suction vortex. Scales of these parent cyclonic storms are separated by approximately 2 orders of magnitude. (Adapted from Fujita, 1986).

can result in confusion and misconception. In an attempt to clarify this problem, Doswell (1987) gives a fresh new perspective to the scaling problem. He defines the large-scale processes as those which are quasi-geostrophic. In contrast, mesoscale processes are those which are linked to processes occurring on both larger and smaller scales. He states that one cannot begin to understand the mesoscale processes without considering both the large scale and the microscale processes together. In essence, he implies that a meteorologist should not investigate mesoscale phenomena without examining processes operating on the larger and smaller scales.

## 1.2 Vertical Motion in the Atmosphere

Scientists involved in the study of meteorological processes have long recognized the importance of vertical motion in the generation of weather phenomena, especially of clouds and precipitation. When an airmass rises in the atmosphere, it encounters lower pressure aloft, and consequently expands and cools adiabatically. As the airmass cools, the relative humidity rises. Sufficient cooling can eventually result in condensation, cloud formation, and precipitation. It can be shown that sustained upward (positive) vertical motion of air can eventually produce saturated conditions in an airmass that was initially relatively dry. Positive vertical motion can also cause destabilization of lapse rates and allow the liberation of latent instability.<sup>1</sup>

The magnitude, areal extent, and time scale of the vertical velocity field is a

---

<sup>1</sup> If a parcel of air in the lower troposphere is sufficiently displaced in the vertical as to acquire a positive excess temperature (i.e. it becomes warmer than the environment), the parcel will then acquire upward acceleration; then the basic state in the layer where the parcel originated is said to possess *latent instability* (Chen, 1982). That is, the parcel will experience free convection if its vertical displacement is sufficient.

|   | HORIZONTAL<br>AREA<br>SCALE<br>(km <sup>2</sup> ) | APPROX.<br>TIME<br>SCALE<br>(min) | DURATION<br>AT A FIXED<br>POINT<br>(min) | APPROX.<br>DIVG.<br>( $\nabla \cdot \vec{V}$ )<br>(s <sup>-1</sup> ) | APPROX.<br>VERTICAL<br>VELOCITY<br>(cm s <sup>-1</sup> ) |
|---|---|-----------------------------------|--|--|--|
| Cyclone<br>scale                        | $0(10^6 - 10^7)$                                  | $0(10^4)$                         | $0(10^3)$                                | $0(10^{-5})$   | $0(1)$   |
| Frontal<br>scale                        | $0(10^5)$   | $0(10^3)$                         | $0(10^2)$                                | $0(10^{-4})$   | $0(10)$  |
| Large<br>Mesoscale<br>(meso- $\alpha$ ) | $0(10^3 - 10^4)$                                  | $0(10^2)$                         | $0(10)$                                  | $3 \times 10^{-4}$<br>$-0(10^{-3})$                                  | $0(10^2)$  |
| Small<br>Mesoscale<br>(meso- $\beta$ )  | $0(10) - 0(10^3)$                                 | $0(1) - 0(10^2)$                  | 1 - 20                                   | $3 \times 10^{-4}$<br>$-0(10^{-3})$                                  | $0(10^2)$<br>$-0(10^3)$                                  |
| Cumulus<br>scale<br>(meso- $\gamma$ )   | $0(1) - 0(10)$                                    | 3 - 50                            | few                                      | $0(10^{-3})$   | $0(10^2)$  |

Table 1.2: Characteristic dimensions and durations of cloud, precipitation, and dynamical features organized on various scales in extratropical cyclones, and magnitudes of horizontal divergence fields and vertical air motions associated with the features.  $0( )$  indicates "on the order of". (Adapted from Hobbs, 1981).

function of the scale of motion being investigated. For synoptic scale features, the vertical motion field is generally of the order of a few centimetres per second, (see Table 1.2). In sharp contrast, the vertical velocity field associated with mesoscale (meso- $\beta$  or smaller) thunderstorm "cells" is of the order of tens of metres per second.

In a convectively unstable atmosphere, positive vertical motion establishes a conducive environment for the production of deep convection. The positive vertical motion provides the required lift to liberate the latent instability in the lower

troposphere. In the absence of this lift, the production of deep convection will generally not occur. This is due to the fact that the atmosphere is never sufficiently unstable that convective overturning can begin spontaneously. The only situation that would allow convective overturning in the absence of lift is an environment that has a super-adiabatic lapse rate; such lapse rates do not readily occur in the atmosphere, except in extremely shallow layers near the surface.

In order for a rising parcel to reach its level of free convection (LFC), it usually must overcome a substantial layer in which it is negatively buoyant. As noted in Doswell (1987), the origins of this required lift are not likely to be found in large scale ascent. The magnitude of synoptic or large scale vertical velocity (on the order of a few centimetres per second) is simply too small to accomplish the needed lift in a reasonable time. Barnes (1976), in support of this theory, indicates that even in the presence of large scale ascent, some sort of triggering mechanism is a necessary ingredient for thunderstorm development. This triggering mechanism is, in essence, a method of lifting an air parcel to its LFC. It is noted by Doswell (1987), that *mesoscale processes tend to supply the required lift to initiate this type of convective activity.*<sup>2</sup>

The most common lifting mechanisms which initiate vertical motion in the atmosphere are frontal lift, orographic lift, and surface convergence. On the mesoscale, the orographically induced vertical velocity, resulting from flow over irregular topography, can be of sufficient strength to initiate deep convection when the static

---

<sup>2</sup> Strong (personal communication) speculates that "the mesoscale process which can initiate the required lifting for convection may itself be initiated as a result of downscaling eddy dissipation of energy from synoptic scale processes".



stability is only marginally conducive to convective activity.

It is somewhat ironic that, being the most important single parameter in the generation of weather events, the environmental vertical velocity is not measured directly in operational forecasting. However, a variety of methods have been developed to assess the magnitude of this parameter from atmospheric variables that are directly measured. The technique one uses generally depends upon the scale of motion being investigated, and the validity of the assumptions involved in that method. Holton (1979) states that the two commonly used methods for inferring the vertical motion field are the kinematic method and the adiabatic method.

The adiabatic technique is based on the thermodynamic energy equation. It also assumes that atmospheric motion is adiabatic, and that all temperature changes in the atmosphere are due to vertical motion and horizontal advection of the temperature field. The kinematic method is based on the continuity equation which expresses the principle of conservation of mass.

#### **1.2.1 Mesoscale Vertical Velocity Fields in the Pre-Thunderstorm Environment**

Though vertical motion has long been recognized as a primary ingredient of significant convective cloud development, its mesoscale structure has received limited attention. Prior to 1979, few mesoscale research experiments involved the investigation of environmental vertical velocity in the pre-thunderstorm environment. The primary reason for this apparent deficiency of research is likely due to the shortage of operational rawinsonde networks of sufficient density to permit such studies.

Initiated in 1979, the Atmospheric Variability Experiment - Severe Environmental Storms and Mesoscale Experiments (AVE-SESAME) I through VI conducted over Oklahoma-Kansas, provided scientists with comprehensive meso- $\alpha$  and meso- $\beta$  scale data sets. The AVE-SESAME I-III data came from 40 rawinsonde stations having an average spacing of 250 kilometres (km), providing data at 3 hour intervals, while AVE IV through VI had 20 stations in Oklahoma with an average spacing of 80 km. Moore (1986) used the data set to study vertical motion in a severe storm environment. Although these data sets were not ideal for the study of smaller scale convective storms, Moore found that the evolution of the adiabatic vertical motion field agreed with the movement and intensity of strong convective areas.

Sikdar and Fox (1983) investigated an evolving severe storm complex during SESAME. Using the kinematic technique, they found well organized positive vertical motion fields 90 minutes before radar echoes appeared. They also noted that as the storm intensified so did the vertical velocity field. Strong (1986) also used the SESAME data (AVE IV and V) to investigate adiabatic vertical velocity in the pre-storm period. His results indicate that low-level mesoscale ascent was present in the pre-storm environment for at least six hours prior to the first radar echoes.

### **1.3 Divergence in the Lower Troposphere**

In the Ekman layer, friction (drag) has a significant effect on the surface wind. The presence of a frictional drag force results in the development of a cross isobaric component in the large-scale surface wind field. The consequence of this cross isobaric

component is a converging or diverging of the wind field, depending on whether the flow is cyclonic or anticyclonic. *Horizontal divergence* measures the magnitude of the spreading out or expansion of the wind velocity field; while *convergence* measures the magnitude of the contraction of the wind velocity field. The Cartesian form of the horizontal divergence of the horizontal wind vector  $\vec{V}_H$  is abbreviated by the symbol  $\nabla_H \cdot \vec{V}_H$ . Where the operator  $\nabla_H$  is defined as:

$$\nabla_H \equiv \hat{i} \frac{\partial}{\partial x} + \hat{j} \frac{\partial}{\partial y} \quad (1.1)$$

where  $\hat{i}$  and  $\hat{j}$  are the unit vectors in the  $x$  and  $y$  directions respectively. Therefore, the horizontal divergence of the horizontal wind can be written:

$$\nabla_H \cdot \vec{V}_H = \frac{\partial u}{\partial x} + \frac{\partial v}{\partial y} \quad (1.2)$$

From the continuity equation it can be shown that

$$\frac{\partial u}{\partial x} + \frac{\partial v}{\partial y} = \frac{1}{A} \frac{dA}{dt}, \quad (1.3)$$

where  $A$  is the initial area of the fluid element and  $dA/dt$  is the rate of change of area with time. Thus, the horizontal divergence at a point is equal to the fractional rate of change of the area enclosed by a small chain of fluid particles surrounding the point.

Chen (1982) indicates that “low-level convergence is produced as a net effect of a dynamically driven circulation interacting with the terrain”. He goes on to cite the following features that tend to be associated with areas of convergence:

- surface low pressure centres;
- upslope wind components;

- confluent and convergent streamlines;
- surface isobaric troughing, surface fronts, thunderstorm outflow boundaries, and sea-breeze fronts.

### **1.3.1 The Relationship Between Vertical Velocity and Divergence**

In the lower troposphere, vertical velocity fields are intimately associated with areas of surface divergence and convergence. Air converging at low levels over an area must ultimately be forced upward above the zone of convergence. Thus, low-level convergence is usually associated with positive (upward) vertical motion, or ascent. Conversely, low-level divergence is associated with negative vertical motion, or subsidence.

In essence, we are able to infer the sign and relative magnitude of the lower-tropospheric vertical velocity field from the relative size and magnitude of the divergence pattern. This simple relationship stresses the importance of obtaining accurate measurements of the surface divergence fields and helps one understand why surface convergence is such an important parameter in forecasting (McNulty, 1985).

### **1.3.2 The Role of Surface Convergence in the Pre-Thunderstorm Environment**

In an unstable environment, *mesoscale convergence* plays a major role in the development of thunderstorms. Previous studies have found that significant surface convergence precedes the storm event. Byers and Braham (1949) conducted mesoscale research experiments in Florida and Ohio using weather radar. They found that surface convergence was observed at least 30 minutes prior to the storm event. In a

more recent mesoscale experiment in Florida, Ulanski and Garstang (1978) set out to determine the role that surface convergence plays in the formation, maintenance and decay of convective storms. They found that strong surface convergence developed at least ninety minutes prior to the first radar echoes. They also concluded that surface convergence is a cause of the convective storm and not an effect.

In recent years, several mesoscale experiments have been conducted in the drier regions of the northern States. Doneaud et al. (1983) investigated the structure and evolution of surface convergence as it relates to the development of convective storms. Their study confirmed earlier findings that the development of cells of convergence precedes radar echoes, and is directly related to the convective event. Cotton et al. (1983) investigated the formation of a mesoscale convective complex over a broad basin in the Colorado Rockies. They were able to conclude that the dominant feature which influenced the development and early growth of the storm was low-level, convergent, upslope flow. Sidkar and Fox (1983), studied the evolution of a severe storm complex during SESAME. They examined the kinematic structure of the pre-thunderstorm environment and found distinct cells of surface convergence four hours preceding initial radar echoes.

A decade earlier, Henz (1973) suggested that certain areas in the foothills of the Colorado Rockies were favorable for the development of convective cloud. He coined the term "hot spot" or "genesis zone" to describe these regions that repeatedly produce thunderstorms. Barker and Banta (1982) went on to suggest a physical reason for the existence of these hot spots or genesis zones. Through a careful study, they were able to conclude that one of the primary mechanisms for the development

of thunderstorms along the Colorado Rocky Mountains is leeside convergence.

These studies, and others, indicate the importance of strong surface convergence as an ingredient necessary for the occurrence of significant convection. Provided that the environment is conditionally unstable, strong surface convergence (producing localized upward vertical velocities), can generate the required lift to liberate latent instability, initiating thunderstorm development.

#### 1.4 The Objectives of this Study

In late spring and early summer, large fluxes of heat and moisture enter the atmosphere from the earth's surface. In response, the atmosphere may redistribute this imbalance of moisture and heat through convective overturning. If atmospheric conditions are favorable, this convective overturning will result in the development of a thunderstorm. The thunderstorm, in turn, becomes a vehicle for further redistribution of excess heat and moisture.

Over western Alberta, along the leeward slopes of the Rocky Mountains, thunderstorms are a frequent event. Meteorologists have often suggested that there are preferred areas of thunderstorm initiation along the Alberta foothills. The development of these thunderstorms is dependent upon the stability of the atmosphere, the amount of moisture available, and the presence of various lifting mechanisms (including localized orographic lift), to liberate the latent instability. On the mesoscale, it has been hypothesized (Doswell, 1987) that low-level forcing provides the required lift to generate the thunderstorms. Meteorologists investigating thunderstorms in the lee of the Rockies have long recognized the significance of strong surface conver-

gence along the foothills (Barker and Banta, 1984, 1985). Under proper conditions, the combination of strong surface convergence and orographic upslope flow produces the lift required to initiate deep convection.

The relationship between surface convergence and vertical motion in the lower atmosphere is a fundamental concept of meteorology. The conceptual model of the relationship between surface convergence and vertical motion is easily observed on the synoptic scale. However, until recently, mesoscale diagnostics of this fundamental concept were not possible in Canada because of the lack of adequate surface and upper air data sets at the mesoscale. Such mesoscale studies are now possible with data from a series of mesoscale experiments, collectively called the Limestone Mountain Experiments (LIMEX), which were conducted over the Alberta foothills since 1980 by G.S. Strong of the Alberta Research Council (ARC).

The LIMEX activities, as described by Strong (1985), culminated with LIMEX-85, carried out during July 08-23, 1985. This first major mesoscale surface and upper air experiment in Canada involved nine special upper air sounding sites, eight automated surface data sites, a sonic sounding unit (SODAR), special sounding flights by a sophisticated research aircraft, and an extensive cloud photography component. Strong gave the following primary goals for LIMEX-85:

1. to diagnose the mesoscale dynamics of the pre-storm and storm environments of Alberta hailstorms, with special emphasis on interactions with synoptic scale processes, and on the creation, breakdown, and role of the capping lid<sup>3</sup>

---

<sup>3</sup> The capping lid is a stable layer, generally between the 850 and 700 mb levels. It tends to act as a quasi-horizontal barrier confining the air below. Consequently the latent instability of the lower atmosphere is allowed to increase (through horizontal advection, diabatic heating, and evaporation). Shallow convective clouds that form below the lid are capped at the inversion. When the cap is

in storm initiation;

2. to obtain high resolution surface and upper air data sets in order to test storm prediction techniques, particularly the Synoptic Index of Convection (Strong and Wilson, 1983).

Strong (1986) describes a conceptual model of thunderstorm genesis based on the capping lid, and tested some aspects of this model using LIMEX-80 data from Alberta, and SESAME data from the Oklahoma experiments. The current study will utilize LIMEX-85 data to test other aspects of Strong's model over Alberta. In particular, the objectives of the current study are:

1. to diagnose the temporal and spatial evolution of the vertical velocity and surface convergence fields in the pre-thunderstorm environment;
2. to test the theory that suggests that strong surface convergence is a precursor to deep convection;<sup>4</sup>
3. to test the theory that significant vertical motion is present in the lower atmosphere several hours prior to thunderstorm development;
4. to investigate the importance of the advection term in the adiabatic method of measuring vertical velocity;
5. to determine the operational utility of existing sub-synoptic data sources;
6. to make recommendations for further scientific field research activities.

---

removed, deep convection can develop.

<sup>4</sup> The vertical motion associated with the strong surface convergence ( $\frac{\partial \omega}{\partial z} \simeq -\nabla_H \cdot \vec{V}_H$ ) is "trapped" by a stable T-gradient (capping lid) and a local distortion of the hydrostatic gradient builds up, which eventually leads to "bursting" through the lid.



## **Chapter 2**

# **Data Sources and Analysis Procedures**

### **2.1 The LIMEX-85 Data Set**

The Limestone Mountain Experiment (LIMEX-85) was one of several field research activities carried out by the Alberta Research Council (ARC) in 1985. LIMEX-85 was performed over southwestern Alberta, in the western half of the Alberta Hail Project region. The terrain in this area is characterized by rolling foothills rising gently westward to the Rocky Mountains (see Figure 2.1).

#### **2.1.1 Spatial Resolution of the LIMEX-85 Data**

A high density measurement network was set up in an area of approximately 26,000 square kilometres (km). Nine upper air stations were located with an average spacing of around 50 km. This high resolution upper air network was augmented with eight automatic surface sites deployed by the Alberta Research Council, three standard Atmospheric Environment Service (A.E.S.) surface weather stations, and seventeen Alberta Forestry sites. The consolidation of data from these stations resulted in a data network in which the average spacing between stations was about 25 km. The LIMEX-85 soundings were augmented further by special morning (pre-

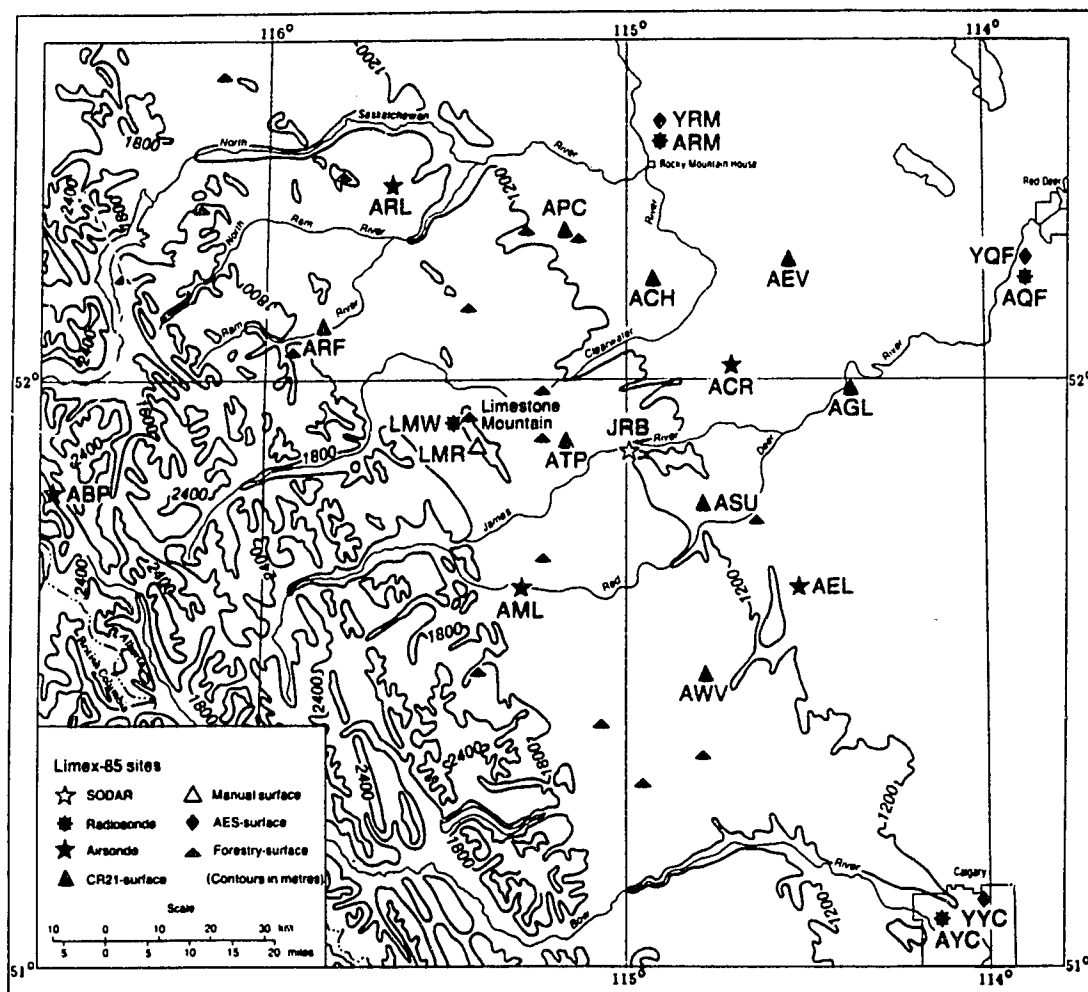


Figure 2.1: Limestone Mountain Experiment Area. The five- or eight-point stars indicate the nine upper air stations involved in LIMEX-85. Legend: ABP-Bow Pass; ACR-Caroline; AEL-Elkton; AML-Mountaineer Lodge; AQF-Red Deer; ARL-Ram Lookout; ARM-Rocky Mountain House; AYC-Calgary; LMW-Limestone Mountain. (Adapted from the Alberta Research Council Field Report, 1985; reproduced with permission).

storm) sounding flights by the AHP research aircraft, and a sonic sounding device (SODAR). However, these additional data have not been processed by the ARC, and are therefore not included in the analysis to follow.

### **2.1.2 Temporal Resolution of the LIMEX-85 Upper Air Data**

The upper air stations released serial soundings at two hour intervals. Initial soundings were released at 0800 MDT (1400 UTC), with two sites making an additional 1300 UTC release for forecasting purposes. The number of successive soundings released thereafter depended upon weather conditions. During days when conditions appeared favourable for deep convection, balloons would continue to be released until 2000 MDT (0200 UTC). However, on days in which little or no convective activity was forecast, operations were discontinued at any time following the 1000 MDT release.

### **2.1.3 Temporal Resolution of the LIMEX-85 Surface Data**

Hourly surface conditions were recorded manually at seven of the nine LIMEX upper air stations. In addition, eight automatic surface dataloggers, Campbell Scientific CR21 units, were programmed to record five minute averages of temperature, humidity, wind direction and wind speed. These data were available at five-minute intervals twenty-four hours a day. Normal hourly and special surface reports were also available from the A.E.S. surface network. Alberta Forestry surface observations, taken twice daily at 1300 and 1900 UTC, are also included in the LIMEX-85 data archive, as well as a once-daily (1800 UTC) observation from an Alberta

Forestry automated recorder at 40-Mile Flats.

#### **2.1.4 Other Data Sources**

The following data were also collected during the Limestone Mountain Experiment:

- National Oceanic and Atmospheric Administration (NOAA) polar orbiting satellite imagery; unfortunately these data were not archived in digital form and only a few operational photographs were salvaged;
- ARC S-band research radar plan-position indicator (PPI) summaries;
- AES surface and upper air synoptic analyses;
- ARC high spatial resolution aircraft data for investigating the capping-lid (not processed to date);
- ARC high temporal resolution SODAR data (not processed to date);
- ARC ground-based photographs of significant convection cloud development.

#### **2.1.5 Remarks**

It is somewhat unfortunate, that after careful planning of this experiment, allocating resources, and implementing the logistics, the one uncontrollable factor did not co-operate. During a period that is climatologically ideal for significant thunderstorm activity in the Alberta Hail Project area, conditions were simply not favourable for deep convective cloud development. Throughout the LIMEX-85 research period, only one deep convection event occurred in the immediate area during days in which all surface and upper air sites were in full operation (July 11, 1985).

Ironically, on that day, most of the heavy thunderstorms developed and moved just north of the mesoscale network. However, a few smaller storms did develop and track over northern sections of the experimental area.

## **2.2 Data Analysis and Fields Investigated**

This diagnostic investigation will focus on the mesoscale structure and evolution of two important parameters generally thought to be required for deep convection, surface convergence and low-level ascent. The mesoscale structure of these fields will be resolved using the LIMEX-85 data set. In addition to the mesoscale data available from LIMEX-85, synoptic and sub-synoptic scale data from a number of different sources will also be employed in this investigation. The main analyses used in this study are:

1. a diagnosis of the synoptic scale setting prior to and during the convective event, using synoptic scale surface and upper air charts from the Canadian Meteorological Centre (CMC);
2. a diagnosis of the meso- $\gamma$  scale convective events as detected by the Alberta Research Council (ARC) S-band radar and NOAA satellite imagery;
3. a diagnosis of the meso- $\beta$  scale vertical velocity and divergence fields in the lower troposphere, including the spatial and temporal evolution of these two fields, using the LIMEX-85 data set;
4. a diagnosis of the stability of the atmosphere prior to the convective events.

This diagnostic study is by no means exhaustive. The various fields analyzed, though somewhat limited, are expected to provide operational and research meteorologists with a beneficial, preliminary understanding of the mesoscale vertical velocity and surface convergence patterns in the lee of the Alberta Rockies (in a pre-thunderstorm environment). Terrain-induced vertical velocity and the moisture convergence fields are examples of two other fields worthy of further study.

### **2.3 Methods of Measuring Vertical Velocity**

Tucker (1972) indicates that synoptic scale vertical velocities are two or three orders of magnitude smaller than horizontal velocities, and that they can be highly variable in space. For this reason, all estimates of large scale vertical velocities are based on indirect methods. Two commonly used methods for inferring the vertical motion field are the kinematic method and the adiabatic method (Holton, 1979).

The adiabatic technique is based on the assumption that the thermodynamic energy of a fluid element remains constant along a trajectory. For adiabatic atmospheric motion there is no exchange of heat between the system and its environment, no latent heating, no radiative heating, etc. Consequently, all temperature changes in the atmosphere are assumed to be due to vertical motion and horizontal advection of the temperature field. The kinematic method is based on the continuity equation which expresses the principle of conservation of mass.

### 2.3.1 The Adiabatic Method

The derivation of the adiabatic vertical velocity equation begins with the first law of thermodynamics. Starting with the first law of thermodynamics in the form:

$$c_p dT - \alpha dp = dq, \quad (2.1)$$

where  $dT$  is the temperature change,  $p$  is the pressure change,  $c_p$  is the specific heat of air at constant pressure,  $\alpha$  is specific volume, and  $dq$  is the heat absorbed or lost due to diabatic processes. The change is measured along the fluid element trajectory (i.e. following the fluid element). Dividing by the time interval  $dt$  over which the changes occur, equation (2.1) can also be written as

$$c_p \frac{dT}{dt} - \alpha \frac{dp}{dt} = \frac{dq}{dt} = \dot{q}. \quad (2.2)$$

Now let us assume that we are dealing with an adiabatic situation, i.e.  $\dot{q} = 0$ . Recalling that the vertical velocity in pressure coordinates is defined by  $\omega = dp/dt$ , we have:

$$\frac{dT}{dt} = \frac{\alpha \omega}{c_p}. \quad (2.3)$$

Expanding the Lagrangian temperature change:

$$\frac{dT}{dt} = \frac{\partial T}{\partial t} + \vec{V}_H \cdot \nabla_H T + \omega \frac{\partial T}{\partial p} = \frac{\alpha \omega}{c_p}, \quad (2.4)$$

where  $\vec{V}_H$  is the horizontal velocity vector,  $\nabla_H$  is the horizontal gradient operator, and  $p$  is the vertical coordinate. This may be rewritten as

$$\frac{\partial T}{\partial t} + \vec{V}_H \cdot \nabla_H T = \omega \left[ \frac{\alpha}{c_p} - \frac{\partial T}{\partial p} \right]. \quad (2.5)$$

Using the definition of potential temperature:

$$\theta = T \left( \frac{p_0}{p} \right)^{R/c_p}, \quad (2.6)$$

taking the logarithms:

$$\ln \theta = \ln T + \frac{R}{c_p} (\ln p_o - \ln p), \quad (2.7)$$

and differentiating with respect to pressure we find:

$$\frac{1}{\theta} \frac{\partial \theta}{\partial p} = \frac{1}{T} \frac{\partial T}{\partial p} + \frac{R}{c_p} \left( -\frac{1}{p} \right). \quad (2.8)$$

Now multiplying by  $T$ , equation (2.8) may be written:

$$\frac{\partial T}{\partial p} = \frac{T}{\theta} \frac{\partial \theta}{\partial p} + \frac{RT}{pc_p}. \quad (2.9)$$

From the Equation of State,  $RT/p = \alpha$ ; therefore:

$$-\frac{T}{\theta} \frac{\partial \theta}{\partial p} = \frac{\alpha}{c_p} - \frac{\partial T}{\partial p}. \quad (2.10)$$

Substituting equation (2.10) into equation (2.5) and letting:

$$-\frac{T}{\theta} \frac{\partial \theta}{\partial p} = S_p, \quad (2.11)$$

where  $S_p$  is the static stability parameter, we find:

$$\omega = S_p^{-1} \left[ \frac{\partial T}{\partial t} + \bar{V}_H \cdot \nabla_H T \right]. \quad (2.12)$$

The static stability parameter can also be expressed in terms of the temperature lapse rate. This can be shown differentiating equation (2.7) with respect to height:

$$\frac{1}{\theta} \frac{\partial \theta}{\partial z} = \frac{1}{T} \frac{\partial T}{\partial z} + \frac{R}{c_p} \left( -\frac{1}{p} \frac{\partial p}{\partial z} \right). \quad (2.13)$$

Assuming hydrostatic equilibrium,<sup>1</sup> ( $dp/dz = -g/\alpha$ ), equation (2.13) can be written as:

$$\frac{T}{\theta} \frac{\partial \theta}{\partial z} = \frac{\partial T}{\partial z} + \frac{RT}{p\alpha} \frac{g}{c_p}. \quad (2.14)$$

---

<sup>1</sup> The author verified the validity of utilizing the hydrostatic equation on the mesoscale by applying a method of scale analysis as outlined in Holton (1979). The results confirmed Holton's statement that "only for intense small-scale systems such as squall lines and tornadoes is it necessary to consider departures from hydrostatic balance."



Recalling the ideal gas law  $p\alpha = RT$ , we have:

$$\frac{T}{\theta} \frac{\partial \theta}{\partial z} = \frac{\partial T}{\partial z} + \frac{g}{c_p}. \quad (2.15)$$

By definition,  $-\partial T/\partial z$  is the actual *environment lapse rate* ( $\Gamma$ ) and  $g/c_p$  is the *dry adiabatic lapse rate* ( $\Gamma_d$ ). Therefore, equation (2.15) can be written:

$$\frac{T}{\theta} \frac{\partial \theta}{\partial z} = (\Gamma_d - \Gamma) \quad (2.16)$$

or

$$\frac{T}{\theta} \frac{\partial \theta}{\partial p} \frac{\partial p}{\partial z} = (\Gamma_d - \Gamma). \quad (2.17)$$

Once again applying the hydrostatic equation

$$-\frac{T}{\theta} \frac{\partial \theta}{\partial p} = \frac{\Gamma_d - \Gamma}{\rho g}. \quad (2.18)$$

The left hand side of equation (2.18) is the definition of the Static Stability Parameter (equation (2.11)), which can therefore be written:

$$S_p = \frac{\Gamma_d - \Gamma}{\rho g}. \quad (2.19)$$

With the exception of  $\omega$ , all the terms in equation (2.12) can be measured; therefore, equation (2.12) can be used to compute  $\omega$ .

The obvious disadvantage of the adiabatic method is that the horizontal temperature advection must be evaluated at a point. Another disadvantage with this technique is that it will give large errors when the environmental lapse rate approaches the dry adiabatic lapse rate (i.e., small static stability). Since this method is based on the assumption that all changes in temperature are due to adiabatic processes, it should not be used to calculate vertical velocities in the diabatic heating layer (surface boundary layer) or in saturated conditions where non-adiabatic

processes are taking place. These disadvantages will be discussed in greater detail in Section 2.3.6 and in Chapter 3.

### 2.3.2 The Kinematic Method

The kinematic method is based on the principle of conservation of mass as expressed by the continuity equation. Let us consider the continuity equation in pressure coordinates (once again assuming hydrostatic equilibrium):

$$\nabla_p \cdot \vec{V}_H + \frac{\partial \omega}{\partial p} = 0. \quad (2.20)$$

Integration from pressure level  $p_o$  to level  $p$  yields

$$\omega(x, y, p) - \omega(x, y, p_o) = - \int_{p_o}^p \nabla_p \cdot \vec{V}_H dp. \quad (2.21)$$

or

$$\omega(x, y, p) - \omega(x, y, p_o) = - \int_{p_o}^p \left( \frac{\partial u}{\partial x} + \frac{\partial v}{\partial y} \right)_p dp \quad (2.22)$$

The primary advantage of the kinematic technique rests in its apparent simplicity. The only assumption made is hydrostatic balance, which is a reasonable assumption for most atmospheric processes (Holton, 1979). Another key advantage of this method is the absence of a time derivative in the continuity equation. This feature gives the kinematic technique the characteristic of being a purely diagnostic procedure; that is, there is no need for serial soundings.

The major disadvantage with the kinematic technique is that the horizontal divergence must be evaluated at a number of levels. Theoretically, this is a trivial process; however, the computation of the horizontal divergence is extremely sensitive to small errors and unresolved variability in wind speed and direction. Holton

(1979) indicates that a 10 percent error in the observed wind data could result in a 110 percent error in the divergence calculation.

Another noteworthy disadvantage of the kinematic technique is that errors in the vertical velocity computation will accumulate with height due to the method of integration. That is, since the integration is generally performed from the surface, (where the boundary conditions require  $\omega = 0$  or  $\omega =$  the computed terrain induced vertical velocity), to the top of the atmosphere (with boundary condition  $\omega = 0$ ), an error in the lower levels will contaminate all vertical velocity calculations above that level. That is, errors tend to accumulate with each integration, often resulting in unrealistic vertical velocities in the mid and upper troposphere.

Finally, it should also be noted that wind measurements are normally obtained from the elevation, azimuth and altitude of the balloon. Consequently, the accuracy of the calculated wind data will decrease with altitude, resulting in erroneous divergence values at higher elevations.

### **2.3.3 Comparison of the Adiabatic and Kinematic Techniques**

Fuelberg and Lee (1982), using the SESAME-AVE I data set, made a comparison of the adiabatic and kinematic techniques for calculating vertical velocity. After a detailed objective and subjective evaluation of both methods, they found that both techniques gave good results at the 700 mb level. At 500 mb, the kinematic result emerged superior. Strong (1986) has noted that in the case presented by Fuelberg and Lee, the deterioration of the adiabatic method at 500 mb is likely due to violation of the adiabatic assumption; that is, the latent heat associated with

convective cloud formation has also influenced the change in temperature.

Barnes (1976) documented that the strong up and down drafts associated with thunderstorms tend to act like a solid body to the upper winds. This blocking phenomena actually diverts the upper winds around the thunderstorm. This significantly affects the horizontal divergence field, which in turn influences the vertical velocity computation. Strong (1986) therefore suggests that kinematic vertical velocity values derived in the presence of this blocking phenomena require careful interpretation. One may no longer be looking at the environmental vertical velocity, but rather, at the storm scale vertical motion averaged over the grid cells. That is, the local divergence field in the vicinity of a thunderstorm is averaged over the area of the analysis grid cell. The resulting field is "contaminated" and is not a faithful representation of either the storm scale vertical motion or the vertical motion of the environment in which that storm is developing.

There is little doubt that the kinematic technique would be preferred over the adiabatic technique, were it not for the serious problem encountered in the vertical integration of the horizontal divergence.

#### **2.3.4 The Modified Adiabatic Method of Computing Vertical Velocity**

As noted in Section 1.3.2, the divergence term in the kinematic technique is extremely sensitive to small errors in the observed wind field. This disadvantage restricts application of the kinematic technique to cases where the data is both accurate and representative since point data is used to derive the divergence. In contrast, Petterssen (1956) points out that the adiabatic technique is less sensitive

to small errors in the observed wind data. He indicates that the gradient wind can be used to evaluate the advection term. Strong (1986) simplifies the method even further by suggesting that in the absence of fast moving fronts, the advection term can be neglected. Consequently, Strong eliminates the requirement for accurate wind data.

Strong's (1986) modification of the adiabatic technique involves the following steps. Let us start with equation (2.4) of Section 2.3.1:

$$\frac{\partial T}{\partial t} + \vec{V}_H \cdot \nabla_H T + \omega \frac{\partial T}{\partial p} = \omega \frac{\alpha}{c_p}. \quad (2.23)$$

If one neglects the horizontal advection term and applies the approximation<sup>2</sup>:

$$\omega \approx -\rho g w \quad (2.24)$$

to the right hand side of:

$$\frac{dT}{dt} = \frac{\partial T}{\partial t} + \vec{V}_H \cdot \nabla_H T + \omega \frac{\partial T}{\partial p} = \frac{\alpha \omega}{c_p}, \quad (2.25)$$

the following result is obtained:

$$\frac{\partial T}{\partial t} + \omega \frac{\partial T}{\partial p} \approx -\frac{g}{c_p} w. \quad (2.26)$$

But,  $g/c_p$  is the dry adiabatic lapse rate ( $\Gamma_d$ ). Therefore,

$$w \approx -\frac{1}{\Gamma_d} \left( \frac{\partial T}{\partial t} + \omega \frac{\partial T}{\partial p} \right). \quad (2.27)$$

---

<sup>2</sup> This approximation assumes hydrostatic equilibrium. It can be obtained by expanding  $\omega$  and comparing the orders of magnitude. That is,

$$\omega \equiv \frac{dp}{dt} = \frac{\partial p}{\partial t} + u \frac{\partial p}{\partial x} + v \frac{\partial p}{\partial y} + w \frac{\partial p}{\partial z}$$

(Holton, 1979).

The two terms on the right hand side of equation (2.27) represent the local rate of temperature change ( $\partial T/\partial t$ ), and the vertical temperature advection ( $w\partial T/\partial p$ ). Figure 2.2 is a graphical representation of this equation. The figure contains two serial soundings of the atmosphere over a particular point. Let  $T_{t_o}(p)$  denote the initial temperature sounding, and let  $T_{t_1}(p)$  denote the temperature profile at some time later. The local rate of temperature change at pressure  $p_o$  is calculated by taking the difference in the temperature at a particular level ( $p_o$ ), and then dividing it by the time interval between the serial soundings ( $t_1 - t_o$ ). That is,

$$\frac{\partial T}{\partial t} \doteq \frac{T_{t_1}(p_o) - T_{t_o}(p_o)}{t_1 - t_o}. \quad (2.28)$$

To find the vertical advection term, ( $w\partial T/\partial p$ ), we consider a parcel initially at point A with temperature  $T_A(p_o)$ . If this parcel is lifted dry adiabatically until it intersects the later sounding at point L, (with pressure  $p_1$  and temperature  $T_{t_1}(p_1)$ ), the vertical advection term is given by

$$\omega \left( \frac{\partial T}{\partial p} \right)_t \simeq \left[ \frac{T_L(p_1) - T_B(p_o)}{t_1 - t_o} \right] \quad (2.29)$$

The vertical velocity is obtained by simply solving for the change in pressure (or height) of the lifted parcel and dividing by the time interval.

In addition to vertical motion, the temperature profile can be altered by horizontal advection and diabatic processes. If the modified adiabatic method is applied to cases in which diabatic processes or baroclinic conditions are prevalent, inaccurate vertical velocity computations will ensue. Consequently, it is essential to recognize the limitations of this method, that this technique should only be applied when the conditions are such that the horizontal advection and diabatic effects can be

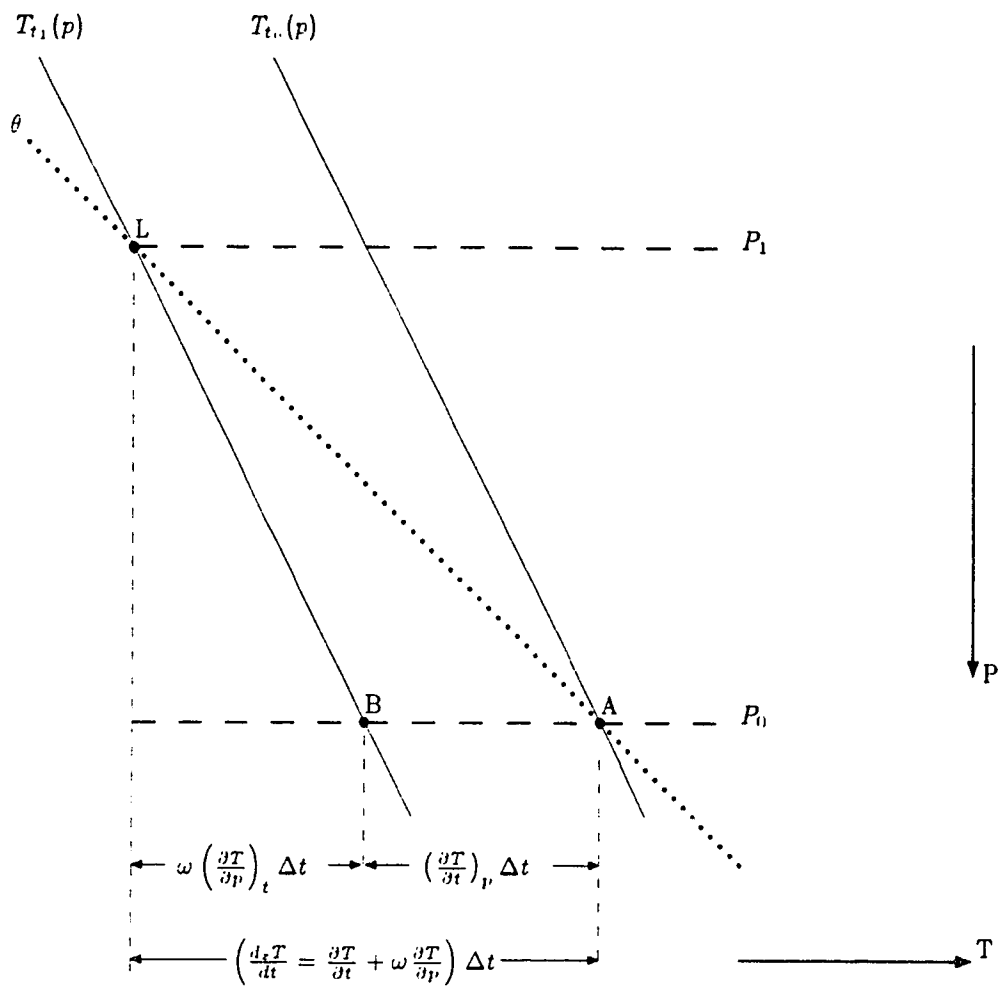


Figure 2.2: Schematic representation of modified adiabatic computations. The sequential modification of two soundings at a single site through adiabatic vertical motion. (Adapted from Strong, 1986).

ignored. In the following section, the author will attempt to justify the assumption that the horizontal temperature advection is negligible in non-baroclinic situations.

### **2.3.5 Importance of the Horizontal Temperature Advection Term**

It has been suggested by Strong (1986) that in the absence of a significant baroclinic zone, the horizontal temperature advection term can be neglected in the adiabatic technique. In his study, Strong estimated that the temperature changes due to advection are of the order 0.1 to 0.2 degrees Celsius per hour, depending upon the magnitude of the temperature gradient and the strength of the wind field. Strong (1986) used synoptic scale upper air charts to estimate the magnitude of the thermal advection and considered it to be small enough to ignore in the cases he studied.

Taking a slightly more rigorous approach, the author performed a detailed, three-dimensional mesoscale analysis of the temperature advection field on the LIMEX storm day July 11, 1985. The method involved the following steps:

1. using a standard gridding technique, the u and v components of the grid wind were determined;
2. using the mesoscale objective map analysis technique outlined in Section 2.6, the u and v components of the wind field and the temperature field were analyzed;
3. using a simple finite-difference technique, the gradient of the temperature field was estimated;



4. the advection of the temperature field was calculated;
5. the station values of temperature advection were estimated from the advection field.

This analysis was performed at 10 mb intervals from approximately 10 mb above the surface to the 800 mb level, and at 50 mb intervals from the 800 mb to 350 mb levels. The 50 mb data were then interpolated to 10 mb intervals assuming a linear relationship. The result of this laborious process was a “sounding” of the change of temperature due to advection for a particular period. Using the 1600 and 1800 UTC soundings, a mean 1700 UTC sounding was generated for each upper air station. These mean soundings, believed to be representative of the mean conditions between 1600 and 1800 UTC, were then used to perform the analysis mentioned above.

The change of temperature due to advection at a point was found to average less than the 0.5 degrees Celsius ( $^{\circ}\text{C}$ ) for the two-hour period. That is, the change of temperature due to advection was less than the RMS error for rawinsonde data ( $0.5^{\circ}\text{C}$ ).

The next step in this process of determining the importance of the advection term involved calculating the adiabatic vertical velocity. This was accomplished using the method outlined below:

1. the change of temperature due to advection was added to the 1800 UTC sounding;
2. using the 1600 and “adjusted” 1800 UTC soundings, the environmental vertical velocity was calculated for each LIMEX upper air station using the adiabatic

technique as described in Section 2.3;

3. the resulting vertical velocity computations were compared with the results obtained using the modified adiabatic method.

It was found that including the advection term (that averaged less than  $0.5^{\circ}\text{C}$  in this case), did not affect the vertical velocity computations significantly. By inspection of the resulting data, it was found that below 600 mb the maximum difference in vertical velocity computations was less than 1 centimetre per second ( $\text{cm s}^{-1}$ ). The average difference in the vertical velocity computations was found to be less than  $0.5 \text{ cm s}^{-1}$ . The results confirmed Strong's (1986) assertion, that in the absence of fast moving fronts, the advection term in the adiabatic method can be ignored.

### **2.3.6 Disadvantages of the Modified Adiabatic Technique**

Neglecting the advection term in the adiabatic technique simplifies calculations, but there are other major drawbacks to this method. Difficulties in computing the vertical velocity still occur when the lapse rate approaches the dry adiabatic rate ( $9.8^{\circ}\text{C km}^{-1}$ ). Complications also arise when non-adiabatic processes are occurring. Diabatic heating in the lower levels of the atmosphere and latent heat release (due to cooling to saturation) in the mid-troposphere are two critical non-adiabatic processes that cause errors in vertical velocity computations using this technique.

The problem of dealing with dry or super-adiabatic lapse rates in the lower troposphere was rectified by designing a subroutine that would modify the upper air sounding. The modification was based on the following argument. Super-adiabatic

lapse rates occur predominantly in two different areas: in the planetary boundary layer (where they are generated by strong solar insolation), and in the mid-troposphere (where they are observed when a sonde comes out of cloud and finds itself in a relatively cooler environment). In processing the LIMEX-85 data, the author did not attempt to compute the adiabatic vertical velocity in the lowest 60 mb of the surface layer (where super-adiabatic lapse rates were frequently observed). However, it was revealed that even above this 60 mb layer, super-adiabatic lapse rates were occasionally found in very shallow layers (10-30 mb). It was determined that if the temperature was adjusted<sup>3</sup> by 0.1 to 0.4°C, the super-adiabatic rates in these shallow layers could be removed. With a dry bulb temperature RMS error of 0.5°C, it does not seem unreasonable to allow for a slight modification of a sounding to remove a super-adiabatic lapse rate that may be spurious. This modification procedure had a positive effect on the overall performance of the software designed for this study.

Miller and Panofsky (1958) indicate that in a cloud-free environment, non-adiabatic effects are negligible above the surface boundary layer. However, once clouds begin to form, the adiabatic cooling process becomes saturated-adiabatic as latent heat is released during the condensation process. This release of latent heat partially counteracts cooling from other processes such as lift or advection.

In spite of the disadvantages of the adiabatic technique, Petterssen (1956) in-

---

<sup>3</sup> A modification routine was written by the author that compared the potential temperature at each level (above surface pressure - 70 mb) with the potential temperature of the previous level. If the potential temperature decreased with height, then the dry-bulb temperature at that level was increased by 0.05°C and the potential temperature at that level was recalculated. The potential temperatures would be compared again and adjustments made as necessary. This process was carried out on each sounding.

dicates that it is still an adequate method for obtaining estimates of the vertical motion field. Besides, the kinematic technique raises some equally serious uncertainties, especially when applied in the vicinity of convective storms (Strong, 1986).

## 2.4 Method of Measuring the Divergence

In a Cartesian coordinate system, the wind velocity field ( $\vec{V}$ ) has components  $u, v$ , and  $w$  in the  $x, y$ , and  $z$  directions, respectively. The mathematical expression for divergence is obtained by operating on the wind velocity field with the divergence operator  $\nabla \cdot$  :

$$\nabla \cdot \vec{V}. \quad (2.30)$$

The operator  $\nabla$  is defined as:

$$\nabla = \hat{i} \frac{\partial}{\partial x} + \hat{j} \frac{\partial}{\partial y} + \hat{k} \frac{\partial}{\partial z} \quad (2.31)$$

where  $\hat{i}$ ,  $\hat{j}$ , and  $\hat{k}$  are the unit vectors defined in the  $x, y$ , and  $z$  directions respectively. By definition (Huschke, 1959), "divergence is the expansion or spreading out of a vector field. In mathematical discussion, divergence is taken to include *convergence* which is negative divergence."

In general, the magnitude of the horizontal velocity in the atmosphere is two to three orders of magnitude greater than the magnitude of the vertical velocity. Huschke (1959) notes that "because of the predominance of horizontal motions, the divergence usually refers to the two-dimensional horizontal divergence of the velocity field." The divergence of the two-dimensional horizontal velocity field can

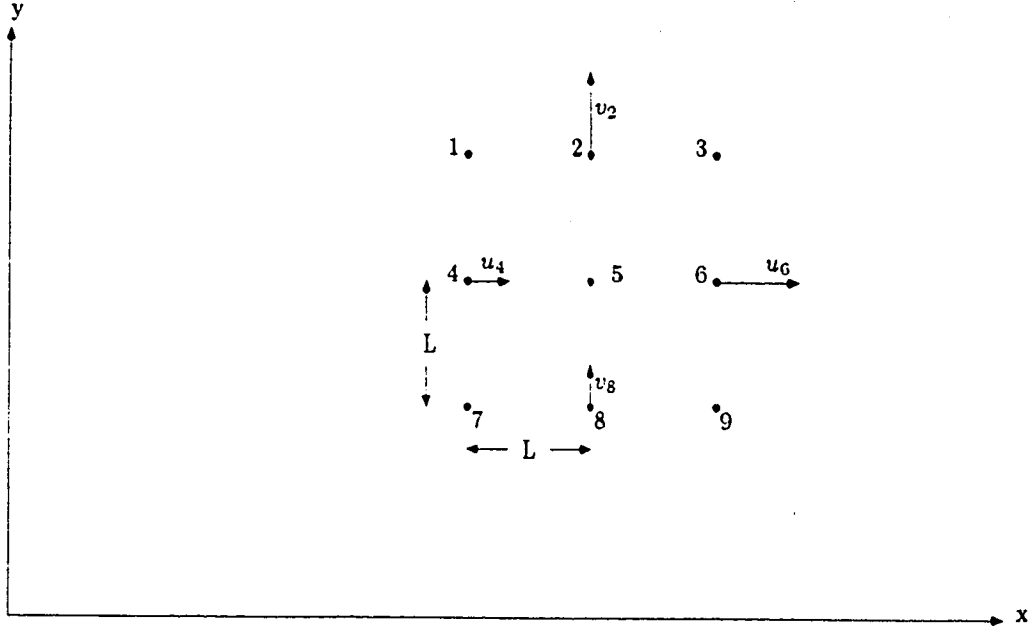


Figure 2.3: A simple analysis grid used for estimating the divergence.

be written:

$$\nabla_H \cdot \vec{V}_H = \frac{\partial u}{\partial x} + \frac{\partial v}{\partial y}. \quad (2.32)$$

The common operational method for estimating the horizontal divergence is to use finite differences to evaluate the partial derivatives in equation (2.32). That is, the partial derivatives  $\partial u / \partial x$  and  $\partial v / \partial y$  are approximated by the finite difference values  $\Delta u / \Delta x$  and  $\Delta v / \Delta y$ . Consider a common array of grid points on a conformal map projection (Figure 2.3). Let:

- $u_4$  denote the component of velocity in the x direction at point 4,
- $u_6$  denote the component of velocity in the x-direction at point 6,
- $v_8, v_2$  denote the components of velocity in the y-direction,

- $L$  denote a unit length of grid.

The divergence at point 5 is approximated by:

$$\nabla_H \cdot \vec{V}_H \doteq \frac{u_6 - u_4}{2L} + \frac{v_2 - v_8}{2L}. \quad (2.33)$$

If one were to use the geostrophic winds,  $(u_6 - u_4)$  would be equal to  $(v_2 - v_8)$  and the divergence would be zero. Consequently, one must use the real winds to calculate the divergence and not the geostrophic winds. The main contribution to the divergence is due to the ageostrophic component of the wind field.

The numerical technique employed to determine the mesoscale surface convergence will now be outlined. The essence of the method involves the following steps:

1. the cartesian grid location of each input station is determined;
2. the  $u$  and  $v$  components of the wind for each station are calculated;
3. a mesoscale objective map analysis routine is used to spatially analyze the  $u$  and  $v$  components of the velocity field;
4. a simple first-order centred-difference scheme is used to calculate the divergence.

The gridded divergence field was then contoured using the SurfaceII graphics facility (Sampson, 1978).

In the atmosphere, the magnitude of the horizontal divergence can range from on the order of  $10^{-6}\text{s}^{-1}$  for near geostrophic wind flow, to  $10^{-5}\text{s}^{-1}$  for the wind field associated with migratory cyclonic systems, to  $10^{-4}\text{s}^{-1}$  or  $10^{-3}\text{s}^{-1}$  for motions associated with mesoscale phenomena (reference Table 1.2)

#### **2.4.1 The Significance of Mesoscale Surface Convergence**

It has been indicated by McNulty (1985) that there are four (inter-related) factors necessary for the occurrence of significant convection. These factors are:

- unstable air or a source of destabilization,
- moisture,
- synoptic scale lift aloft, and
- low-level convergence.

McNulty goes on to state that low-level convergence may be the most important of the four factors. He identifies surface convergence as a mechanism for lifting moist, unstable air beyond the level of free convection where it becomes thermally buoyant. In essence, mesoscale surface convergence can initiate mechanical lift near the surface. This localized, forced lift is generally required for potentially unstable air to reach a level where it becomes thermally buoyant.

Along the foothills of western Alberta, topographically-induced low level forcing is a common occurrence. It has been theorized that cells of surface convergence develop along the foothills several hours prior to thunderstorm development (Barker and Banta, 1984). However, due to the lack of a high density data network, this hypothesis has never been verified. As mentioned in Section 1.4, one of the main objectives of this study is to investigate the temporal and spatial evolution of the mesoscale surface convergence field.

In the Chapter 4, the author will diagnose a case study of the July 11 storms that moved through central Alberta during LIMEX-85. The investigation will not

only involve a study of the temporal and spatial evolution of convergence cells in the LIMEX-85 area, but whether the location of the convergence cells is correlated with regions of enhanced vertical motion.

## **2.5 Measuring the Stability**

### **2.5.1 Static Stability**

A radiosonde ascent gives a detailed “instantaneous” profile of the vertical structure of the atmosphere “at a given point”. The instruments measure the pressure, temperature and humidity, giving a thermodynamic profile of the atmosphere. From this profile, the stability of the atmosphere is determined by inspecting the stratification of temperature and moisture. The static stability, as determined from the sonde, reflects the tendency of the atmosphere to dampen or oppose vertical displacement of air parcels.

There are three categories that characterize the static stability of the atmosphere: stable, unstable, and neutrally stable. Using the analogy of a ball resting on a potential energy surface, Verlarde and Normand (1980) eloquently demonstrate the physical meaning of static stability (refer to Figures 2.4 and 2.5).

### **2.5.2 Stability Indices**

Operational meteorologists indicate the local static stability of the atmosphere by using a *stability index*. The stability index (Chen, 1982) “is a single number calculated from a mathematical formula which accounts for the important meteorological parameters which influence the static stability.”



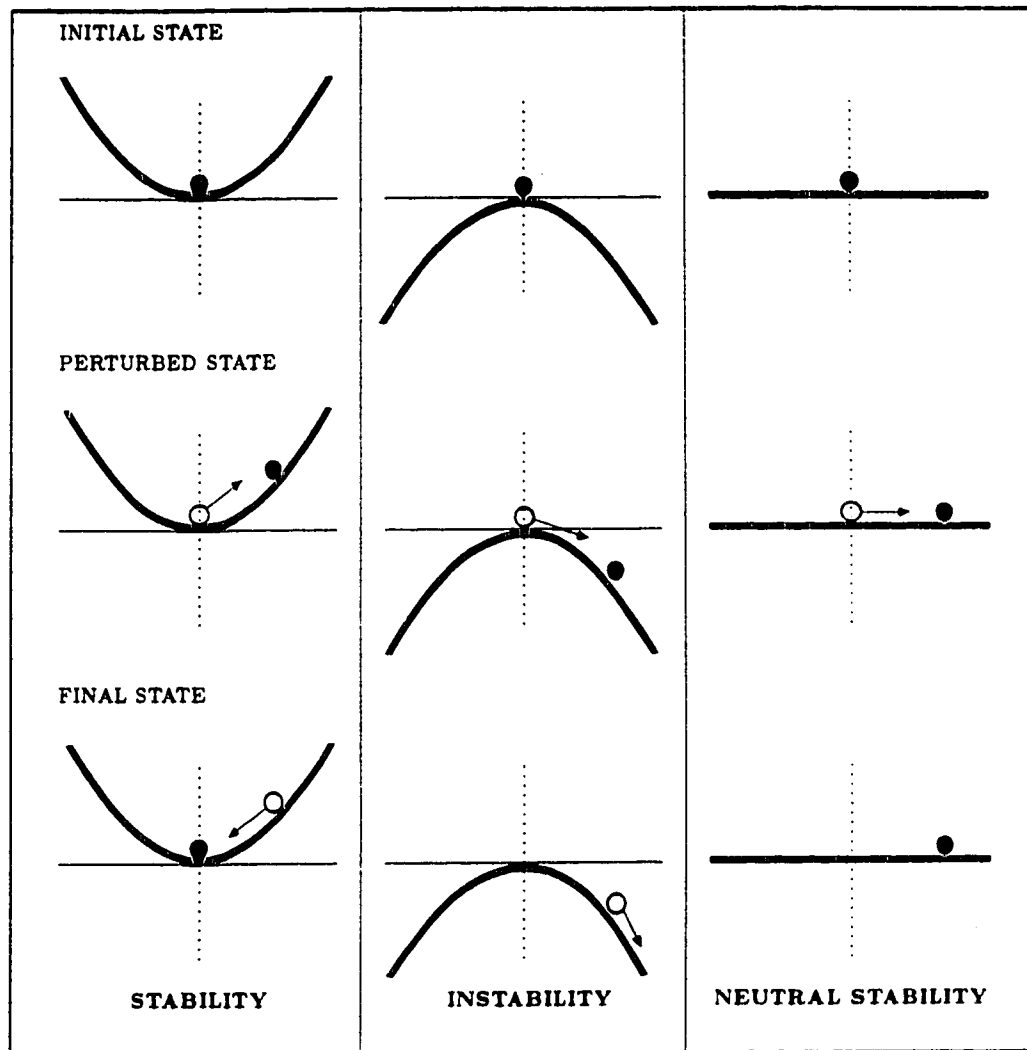


Figure 2.4: The stability of a physical system can be judged from its response to an arbitrary perturbation, such as a small displacement of a marble at rest on a surface. If the surface is concave, the marble eventually returns to its equilibrium position at the bottom of the bowl, and so that position is said to be one of *stable* equilibrium. On a convex surface the marble can be balanced at the apex, but the equilibrium there is *unstable*: the slightest disturbance is amplified as the marble reduces its potential energy by rolling downhill. On a flat surface the marble neither returns to its starting position nor moves farther away from it; the surface exhibits *neutral* stability. (Adapted from Verlarde and Normand, 1980.)

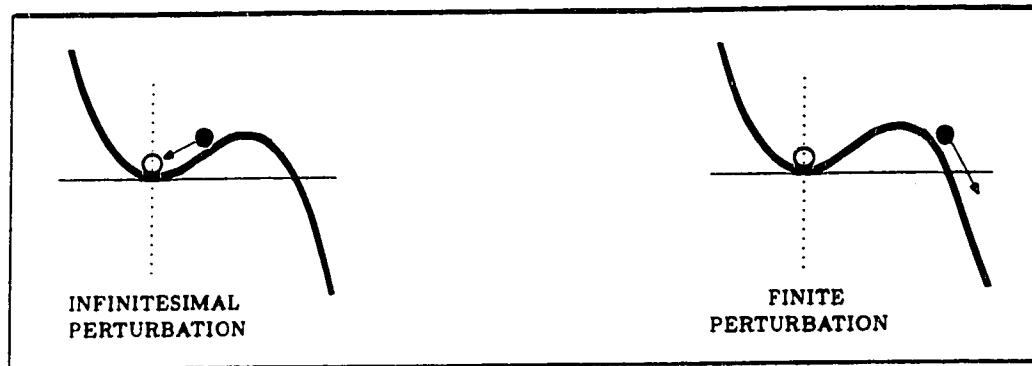


Figure 2.5: A system can be stable with respect to some perturbations but not to others, as in the case of a surface with both concave and convex regions. In a simple fluid a necessary condition for the onset of convection is an unstable distribution of some property such as density. (Adapted from Verlarde and Normand, 1980.)

A few of the more commonly used stability indices are the following:

- Lifted Index (Galway, 1956)
- Showalter Index (Showalter, 1953)
- Total Totals Index (Miller, 1972)
- George's K Index (George, 1960)
- Sly Index (Sly, 1964)
- Convective Stability Index (Goldstein, 1976)

Some of these indices can be calculated directly from the sounding's mandatory data, (e.g. the Total Totals Index involves the algebraic difference between the dry bulb temperature at 850 and 500 mb and the difference between the dew point temperature at 850 mb and the dry bulb temperature at 500 mb). Others, such as the Lifted Index and the Showalter Index are derived from the parcel method<sup>4</sup>

<sup>4</sup> The parcel method (or parcel theory) involves the theoretical vertical displacement of a parcel

The utility of a stability index is based upon its historical application. That is, using a large data set, each stability index has been correlated with different types of convective weather. These correlations have been found to be quite useful as a forecast tool for predicting convective events. The calculated value of an index reflects the static stability of the environment and indicates the type of clouds and weather that tend to be correlated with it.

### The Lifted Index

The Lifted Index (LI) is one of the simplest and most widely used of all the stability indices. It is given by the following expression:

$$LI = T_5 - LT_5 \quad (2.34)$$

where  $T_5$  is the 500 mb dry bulb temperature ( $^{\circ}C$ ); and  $LT_5$  is the temperature ( $^{\circ}C$ ) a surface parcel<sup>5</sup> would acquire if lifted adiabatically from the surface to 500 mb. Table 2.1 gives the stability and type of convective weather to expect for a given estimated Lifted Index.

The Lifted Index tends to faithfully represent low-level moisture, and because it is derived from the parcel method, it accounts for the latent heat that would be available to the parcel. In essence, the Lifted Index is an elementary measure of the of air to a particular reference level. This displacement is assumed to be adiabatic. The algebraic difference between the temperature of the parcel and the environmental temperature at that reference level is then calculated.

There are two assumptions involved in the parcel method: 1) the parcel is sufficiently small that no compensating motions occur in the environment as the parcel moves, and 2) the parcel of air does not mix with its environment in any way as it moves; it therefore maintains its identity (Iribarne and Godson, 1981).

<sup>5</sup> The surface parcel should represent the moisture in the lowest 50 to 100 mb of the atmosphere. This mean low-level moisture is usually determined using an area-balance calculation on the tephigram (Galway, 1956).

| VALUE OF<br>LIFTED<br>INDEX | GENERAL<br>CHARACTERISTIC<br>STABILITY | TYPE OF<br>CONVECTIVE<br>WEATHER  |
|-----------------------------|--|-----------------------------------|
| > 3                         | stable                                 | no showers                        |
| 3 to 0                      | slightly unstable                      | possible showers                  |
| 0 to -2                     | unstable                               | thunderstorms likely              |
| < -2                        | very unstable                          | severe thunderstorms<br>may occur |

Table 2.1: Characteristic stability and expected type of convective weather associated with a given Lifted Index value. Adapted from Chen (1982).

latent instability.

## 2.6 Mesoscale Objective Map Analysis

### 2.6.1 Methodology

The mesoscale objective map analysis technique used in this study is based on a scheme developed by Barnes (1964, 1973). In simple terms, the scheme interpolates unevenly spaced data to a regular grid point array. This involves assigning a weight to each station observation. The value of the weight is a function of the distance ( $D$ ) from the grid point to the stations Cartesian location ( $x, y$ ); refer to Figure 2.6.

The value of the weight assigned to each station observation is determined from the distance-dependent weight factor ( $W$ ),

$$W = 0.1^{(D^2/R^2)}, \quad (2.35)$$

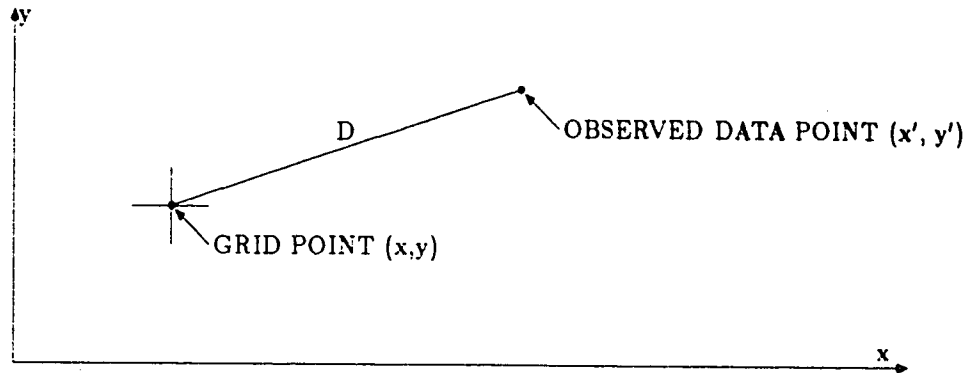


Figure 2.6: The weight of each observed data point is a function of the distance  $D$  from the grid point to the observed data point. Adapted from Harwood (1981).

where  $D$  is the distance between the grid point and the observed data point, and  $R$  is the radius of influence. In essence,  $R$  is the radius at which the weighting factor equals 0.1. Figure 2.7 is a graph of the weight factor ( $W$ ) as a function of distance ( $D$ ) for various values of  $R$ .

The estimated value at each Cartesian grid location  $(x, y)$  is calculated by multiplying each station data point by the weight for that datum, then summing the results and normalizing by the sum of all the weights. The algorithm is summarized by the following equation:

$$f(x, y) = \frac{\sum_{i=1}^N w_i f_i}{\sum_{i=1}^N w_i}$$

where  $w_i$  is the weight for the  $i^{th}$  station,  $f_i$  is the station data value for the  $i^{th}$  station,  $N$  is the total number of stations, and  $f(x, y)$  is the estimated value at the Cartesian grid location  $(x, y)$ .

The initial pass generates an estimate at each Cartesian grid location, using the actual station value as input datum. Each subsequent pass uses, as the input

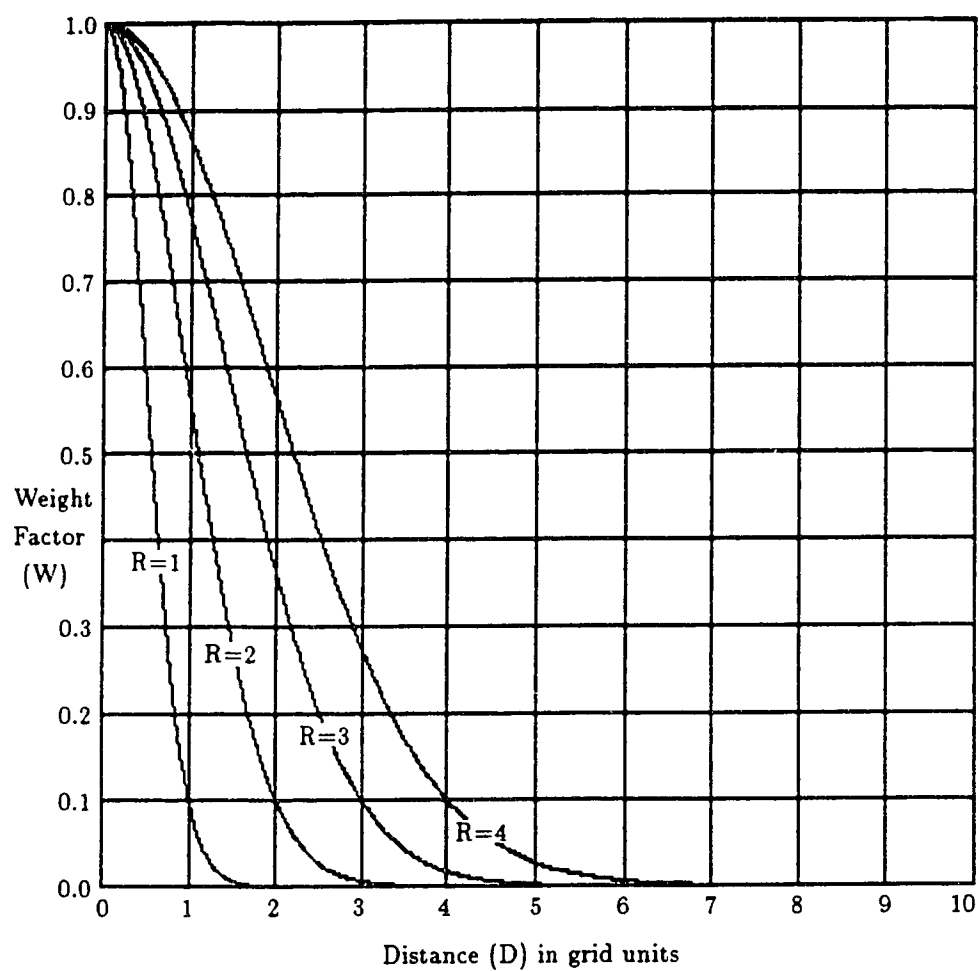


Figure 2.7: Graph of distance-dependent weight factor ( $W$ ) as a function of distance ( $D$ ) for various radii of influence ( $R$ ).

datum, the difference (or residual) between the station value and the value the station would have if it was interpolated from the present grid values. Using the array of residuals as input, the objective analysis program is called and the resultant field of gridded residuals is used to modify the current grid of Cartesian estimates. This iterative procedure is repeated for a subjectively specified number of passes, or until the residual increases. The documentation suggested that four passes would generate a rapid yet faithful analysis.

Upon completion of this iterative improvement procedure, a spatial filter is applied to the gridded data. The central filter is a linear 5 point filter that has the following formula in vector space:

$$Y(M) = 0.625 * Y(M) + 0.25 * (Y(M+1) + Y(M-1)) - 0.0625 * (Y(M+2) + Y(M-2)),$$

where  $M$  is the point on which the filter is acting. The boundary filter is computed using a mirror extension and has the following formulae when applied to the grid points on and neighbouring the border:

$$Y(1) = 0.875 * Y(1) + 0.1875 * Y(2) - 0.0625 * Y(3)$$

$$Y(2) = 0.1875 * Y(1) + 0.625 * Y(2) + 0.25 * Y(3) - 0.0625 * Y(4)$$

This filter is an adapted version of a multi-dimensional low-pass filter designed by Jim Leise of the National Centre for Atmospheric Research (NCAR) in Boulder, Colorado. It was subsequently modified for general use on the LIMEX-85 data set from a complex NCAR program designed to run on a CRAY computer.

When a meteorologist subjectively analyzes surface or upper air charts, he or she first places the previous analysis under the current analysis and then begins to

perform a spatial analysis of the data. The previous analysis is thus used as guidance by the meteorologist to maintain continuity of features; it also tends to shorten the time required to complete the current analysis. In essence, the previously analyzed chart is a first guess field that the analyst uses as guidance when performing a spatial analysis.

When executing a numerical spatial objective analysis, the lack of a first guess field can prove to be somewhat of a problem. For the LIMEX-85 data set, the author rectified this problem by running the objective analysis routine twice for each required analysis. The first run would generate an unrefined, highly smoothed analysis of the data, following the steps previously described. The second run would utilize the initial run output as a first guess field, and then generate a faithful spatial analysis of the input data. It would do this analysis by first determining the residuals at each station (i.e. the difference between the station data value and the value the station would have if interpolated from the first guess field). This residual is then used as the input data for the objective analysis routine. By using this method, it was deemed unnecessary to use post filtering on the second run; this resulted in a superior analysis.

A cursory assessment of the integrity of the mesoscale objective map analysis scheme was performed by the author. A brief description of the method of assessment and its results are given in Appendix A.



### 2.6.2 Objective Map Analysis of LIMEX-85 Data

As mentioned in Section 2.1, the Limestone Mountain Experiment was carried out over a small region along the Alberta foothills. The first task in designing the objective analysis routine was to determine an appropriate grid length to resolve mesoscale features from the high density LIMEX data. Based upon previous studies, it was decided that the grid length should be approximately fifty percent of the average station spacing. Once the grid length was determined, the location of the southwest corner of the grid was chosen such that the grid network would be centred over the LIMEX region. After the southwest location was determined and the grid length was chosen, it was trivial to determine the number of grid points required to construct the grid network. The location of the objective analysis grid is displayed in Figure 2.8.

The mesoscale objective analysis grid, with upper air station locations posted, is displayed in Figure 2.9. The projection is the standard polar-stereographic secant projection true at 60°N, with a grid length of 25 km.

When performing an objective analysis of mesoscale upper air data, one must also take into account balloon drift. That is, as the sonde rises, it is carried horizontally by the prevailing winds aloft. Depending upon the speed of the upper winds, the balloon drift can be significant when performing a spatial objective analysis of the data. A study by Fankhauser (1969), indicated that failure to account for balloon drift could result in a 0.5°C error in the temperature at the 500 mb level (for the particular case he studied). That is, the spatial positioning of isotherms on the

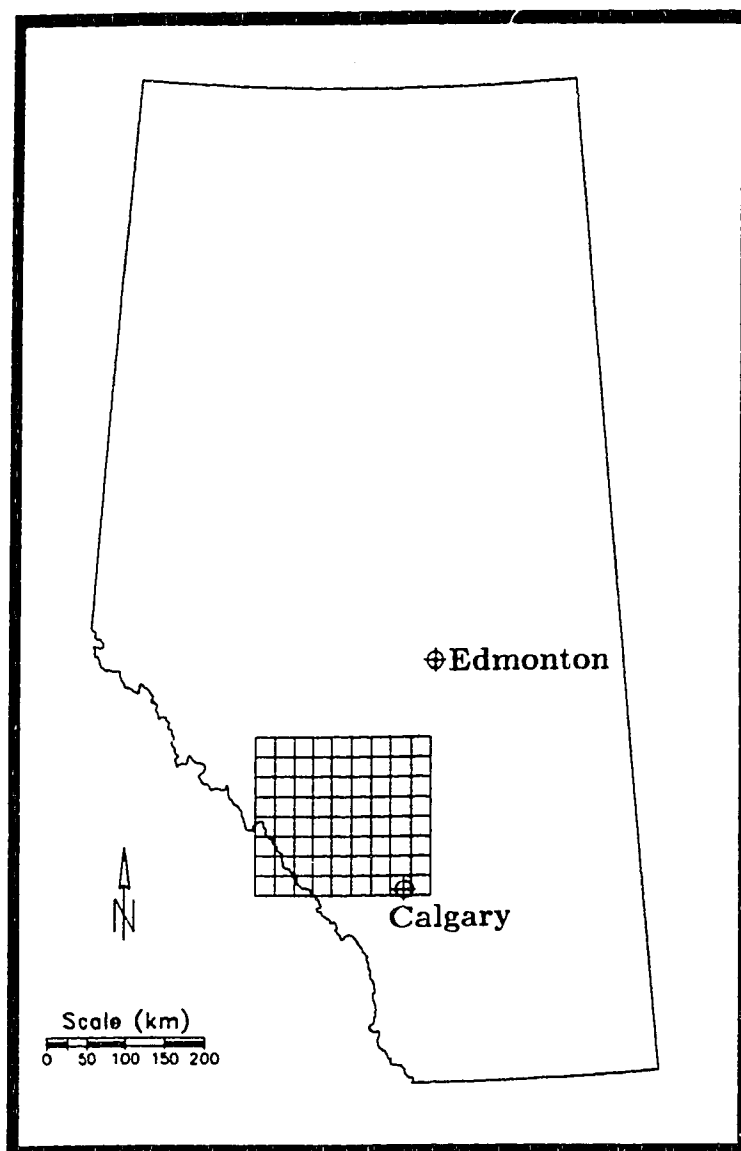


Figure 2.8: Location of LIMEX-85 mesoscale analysis grid.

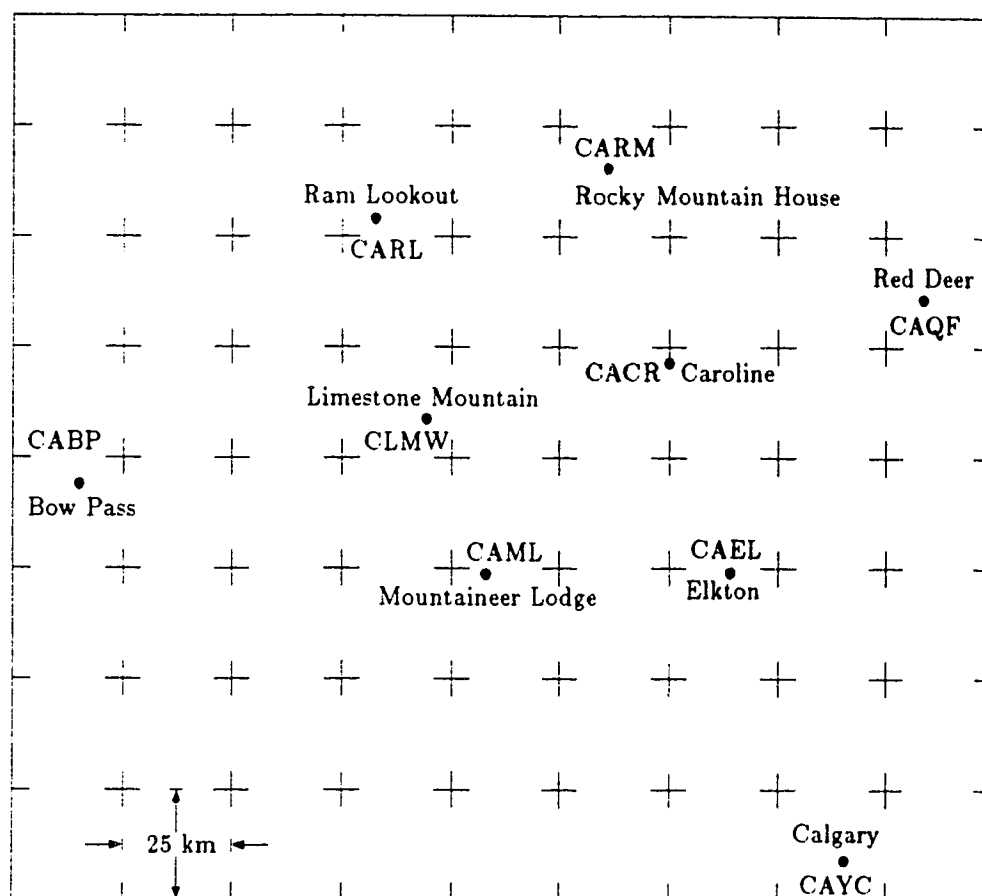


Figure 2.9: LIMEX-85 Analysis Grid with Upper Air Station Locations. The grid length is 25 kilometres.

500 mb level could be out by  $0.5^{\circ}\text{C}$ . In analyzing the LIMEX-85 upper air data, the author developed an objective analysis scheme that calculated balloon drift at each 10 mb interval for which there was data. The spatial objective analysis routine incorporated this information and positioned the station data point accordingly. It was found that the balloon drift below the 600 mb level was less than 15 km.

## 2.7 Summary

The Limestone Mountain Experiment, conducted during the month of July, 1985, has provided scientists with a meso- $\beta$  upper air data set and a meso- $\gamma$  surface data set, according to the Orlanski criteria (see Table 1.1). Using a spatial objective analysis technique designed by Barnes (1976), the author will investigate the mesoscale low-level vertical velocity and surface divergence fields in the pre-thunderstorm environment. But first, the author will briefly investigate the errors involved in calculating vertical motion using the adiabatic technique.

## Chapter 3

### Error Analysis

As indicated by Pedder (1981), it is bad practice scientifically to apply any form of analysis technique without being aware of the magnitude of the probable error on each estimation. He also points out that the interpretation of results should always be considered in relation to the probable errors of estimation. In the following section the author will briefly review a few definitions of error analysis.

#### 3.1 Definitions

Misapplication of concepts is likely the most important source of error in data analysis. If one assumes that the application of a given concept has been carried out without violating its fundamental principals, then the primary source of error is likely associated with the *inaccuracy* of the measuring instrument itself. The *inaccuracy* of an instrument is defined by Huschke (1959) as the difference between the input quantity applied to a measuring instrument and the output quantity indicated by that instrument. At times, the inaccuracy of a measuring instrument is due to a single cause (or a small number of causes) and is usually of the same sign, and hence, in principle is correctable. This type of error is known as a *systematic*

*error*, it tends to affect the whole of a series of observations in nearly the same way. Another type of systematic error can arise due to the characteristics of the observer, these are known as systematic *observational errors*. Huschke (1959) points out that observational errors can be ascertained by a statistical analysis of the observer's readings.

Secondary errors arise from the method of sampling and the model used to perform the analysis. One such error is *random error* which is related to the inherent imprecision of a given process of measurement; it is the unpredictable component of repeated independent measurements on the same object under sensibly uniform conditions. Computational errors are introduced into the analysis when a real number is broken off at a certain decimal position (rounding off). However, these errors are usually relatively small. In comparison, the so-called human factor is responsible for most of the error.

### **3.2 LIMEX-85 Data Uncertainty**

Quality control and error checking of the LIMEX-85 data set has eliminated or corrected most of the systematic and observational errors. Some of the surface data had errors associated with equipment malfunctioning. This data could not be corrected and subsequently was omitted from the analysis.

### **3.3 Uncertainty of Upper Air Data**

The accuracy of upper air data is generally stated in terms of the "root-mean-square (RMS) error", which is simply the square root of the error variance. Strong (1986)

| PARAMETER         | ESTIMATED RMS ERROR  |
|-------------------|--|
| Temperature       | 0.5°C, all levels  |
| Pressure          | 1.3 mb, Surface to 400 mb<br>1.1 mb, 400–100 mb<br>0.7 mb, 100–10 mb |
| Humidity          | 10%, not computed if $T < -40^{\circ}\text{C}$                       |
| Pressure Altitude | 10 gpm at 500 mb<br>20 gpm at 300 mb<br>50 gpm at 50 mb              |

Table 3.1: Estimates of the RMS error in SESAME rawinsonde data as reported by Sienkiewicz et al. (1981). Adapted from Strong (1986).

reproduced the estimates of the RMS errors in the SESAME rawinsonde data that were originally provided by Sienkiewicz et al. (1981). Strong (personal communication) has suggested that the same estimates can be used for the LIMEX-85 data set. Table 3.3 indicates the estimated errors in the thermodynamic parameters used to calculate the vertical velocity using the adiabatic technique. Table 3.3 indicates the estimated error in the wind data that was used to calculate the kinematic fields.

Strong (1986) indicates that a temperature uncertainty of  $0.5^{\circ}\text{C}$  results in an uncertainty in the vertical velocity computation of  $\pm 0.5 \text{ cm s}^{-1}$ . The author has some difficulty accepting this value. Consider the Figures 3.1 and 3.2; where one is estimating the vertical velocity from two serial soundings. The pair of short dashed lines parallel to each temperature profile represent the estimated RMS error in the measured temperature ( $0.5^{\circ}\text{C}$ ). The large dotted line represents a dry adiabat. This adiabat represents the path that an air parcel (at the initial height  $Z_0$ ) would

| PRESSURE<br>LEVEL<br>(mb) | ESTIMATED RMS ERROR IN<br>WIND DIRECTION (degrees)<br>For balloon elevations of: |            | ESTIMATED RMS ERROR<br>IN WIND SPEED ( $\text{m s}^{-1}$ )<br>For balloon elevations of: |            |
|---------------------------|--|------------|--|------------|
|                           | 10 degrees   | 40 degrees | 10 degrees   | 40 degrees |
| 700                       | 09.5   | 1.3        | 2.5  | 0.5        |
| 500                       | 13.4   | 1.8        | 4.5  | 0.8        |
| 300                       | 18.0   | 2.5        | 7.8  | 1.0        |

Table 3.2: Estimates of the RMS errors of the SESAME rawinsonde wind data as reported by Sienkiewicz et al. (1981). Adapted from Strong (1986).

take if it were lifted and cooled adiabatically. The two small dotted lines parallel to the dry adiabat represent error in the adiabat due to the RMS error in the dry bulb temperature. The RMS dry bulb temperature error of  $0.5^{\circ}\text{C}$  agrees with results obtained by Sackiw (1986) using the Alberta Research Council rawinsonde equipment.

These figures clearly indicate that the error in estimating the displacement of the parcel is a function of the lapse rates of the soundings. As the temperature profile approaches the dry adiabatic lapse rate, the possible error in determining  $\Delta Z$  grows rapidly. It should also be apparent that for temperature changes less than the RMS error, the error in estimating  $\Delta Z$  is of the same magnitude as  $\Delta Z$  itself. That is, for small temperature changes ( $<0.5^{\circ}\text{C}$ ), no useful information can be obtained.



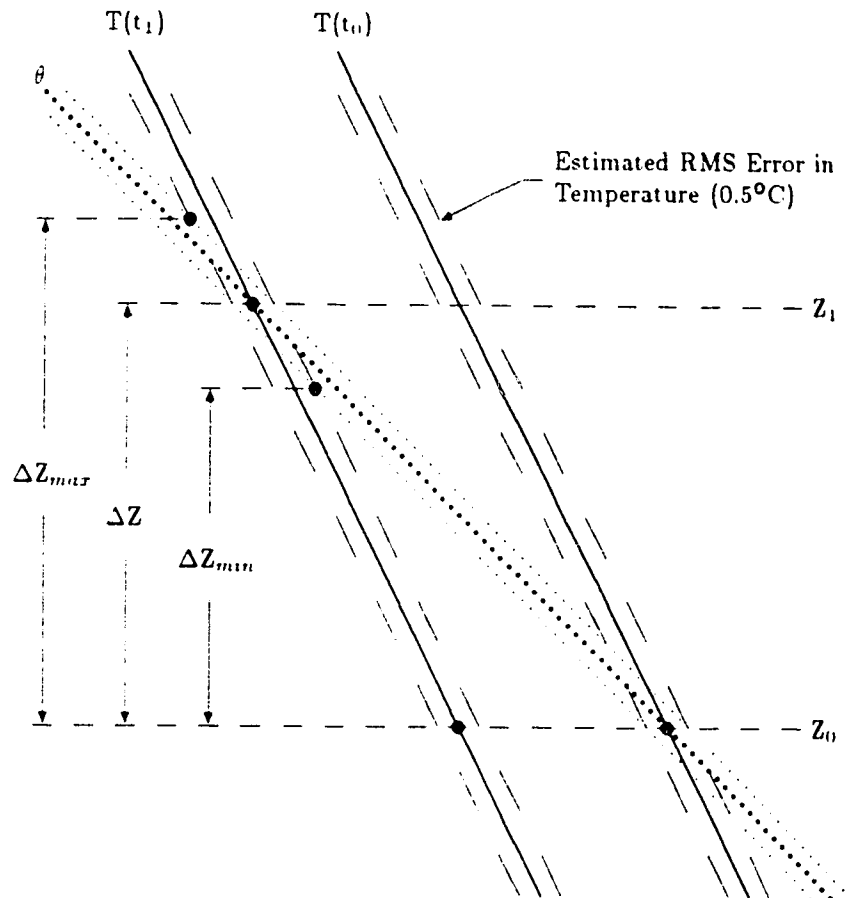


Figure 3.1: Error involved in calculating the adiabatic displacement of a parcel. The error is a function of the estimated RMS error of the temperature and of the lapse rate of the sounding (see Figure 3.2).

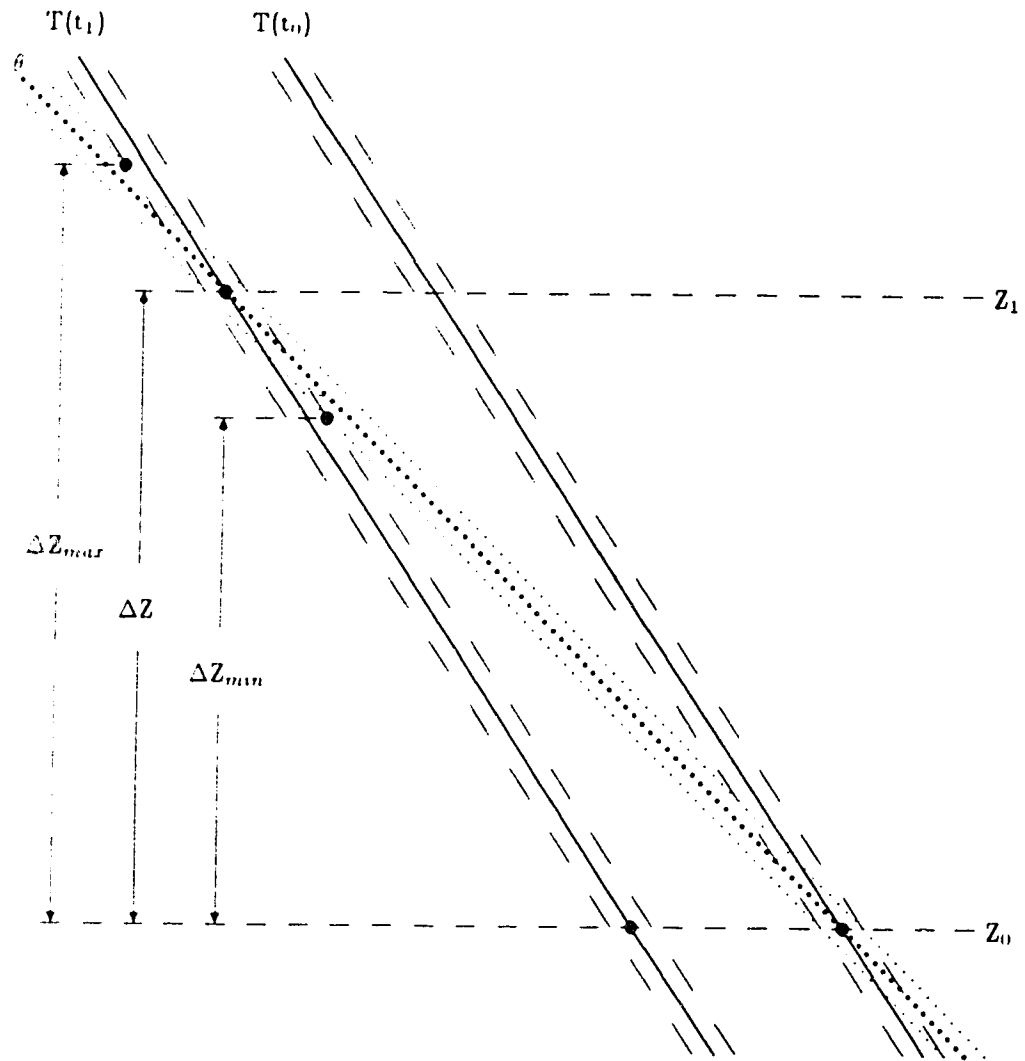


Figure 3.2: Same as Figure 3.1 except the lapse rates of both soundings have been increased. Note the increase of the error in estimating  $\Delta Z$ .

| SOURCE<br>OF<br>ERROR | UNCERTAINTY                      |                                  |
|-----------------------|----------------------------------|----------------------------------|
|                       | Minimum<br>(cm s <sup>-1</sup> ) | Maximum<br>(cm s <sup>-1</sup> ) |
| Diabatic Heating      | -0.3                             | +4.0                             |
| Cloud Penetration     | 0.0                              | +0.5                             |

Table 3.3: Uncertainties in the modified adiabatic vertical velocity calculation due to cloud penetration and diabatic heating. Adapted from Strong (1986).

### 3.4 Uncertainty in the Modified Adiabatic Vertical Velocity Computations

When one considers the sources of error in estimating the vertical velocity using the adiabatic technique, one finds that the most significant errors are associated with the assumptions involved with the technique itself. That is, when the adiabatic assumption is breached the vertical velocity estimates can become extremely inaccurate. Two processes that have a profound effect on the temperature change in the atmosphere are diabatic heating and latent heat release. Diabatic heating of the atmosphere is most prevalent in the surface layer where solar insolation is absorbed by the earth's surface which in turn heats the lower layers of the atmosphere. Latent heat release prevails in the mid-troposphere when cloud formation is occurring. Strong (1986) investigated the effect these two diabatic processes had on the estimation of the vertical velocity. His results are summarized in Table 3.3.

Strong (1986) also cites two other sources of error that occur in the estimation of vertical velocity: balloon drift and off-schedule release time. Through careful

data analysis techniques, both of these errors were eliminated or minimized in this analysis of the LIMEX-85 data. Actual balloon positions were calculated for each 10 mb level. These *new* balloon positions were used in all subsequent spatial analyses. It should be noted that in the lower-troposphere, where the winds aloft are not too strong, the balloon drift was not significant. However, in the mid-troposphere, balloon drift could result in a horizontal displacement of 10 to 15 km. A displacement of this magnitude is not important when considering synoptic scale analyses, but on the mesoscale it can have a profound effect on the spatial analyses.

The problem associated with off-schedule release times refers to the fact that not all balloons were released at exactly the same time, and not all the balloons reach the mandatory levels simultaneously. Consequently, an analysis of the 500 mb data, for example, is not an analysis of the instantaneous conditions at that level. Two steps can be taken to deal with this problem. One can assume that the small differences in release times, and the small differences in the elapsed time required to reach the level of interest are negligible; or one can interpolate the rawinsonde data at a particular level for a given time. The latter approach was used in this study.

The method of interpolation involved generating a *new sounding* from the temporal trend of two serial soundings. For each 10 mb data level, all sonde data were interpolated to a specified time. The result was an instantaneous sounding over station valid for a specified time. It is important to note that this method did not involve extrapolation of the data, which tends to yield erroneous values. The time of the interpolated sounding was usually within 5 to 10 minutes of an actual

sounding.

The underlying assumption, in using this temporal trend interpolation scheme, is that changes in the measured variables are assumed to vary linearly over short time intervals. It was not possible to investigate the validity of this assumption with the data from this experiment.

### **3.5 Uncertainty in Horizontal Divergence Calculations**

The estimated RMS error of the LIMEX-85 wind data is given (by Strong, personal communication) as  $0.5 \text{ ms}^{-1}$ . This value is approximately 10 percent of the mean winds in the surface boundary layer. Holton (1981) indicates that a 10 percent error in the wind data could result in a 110 percent error in the calculated divergence values. This important fact should be kept in mind when diagnosing the surface and 800 mb horizontal divergence fields analyzed in Chapter 4.

## **Chapter 4**

### **Case Study: 11 July 1985**

July 11, 1985 is the most interesting LIMEX-85 case in terms of significant convective activity and completeness of the data set. On that day, the Red Deer S-band research radar detected intense echoes with reflectivity factors in excess of 50 dBZ over northern sections of the experimental area. More intense storms were detected just north of the LIMEX-85 region. From the radar PPI summaries, it appears that these storms developed along the foothills, in the lee of the Rockies, and then moved east-northeastward across the northern half of the LIMEX-85 mesoscale network. Satellite imagery, diagnosed in Section 4.4, supports this scenario. The NOAA 8 satellite images indicate cumuliform cloud developed along the foothills during the mid-afternoon, and thunderstorms moved over northern sections of the LIMEX-85 network in the evening.

#### **4.1 The Synoptic Situation**

The author will initially focus on the synoptic situation 12 to 24 hours before the storm event (the pre-storm environment). The synoptic scale analyses for 0000 UTC and 1200 UTC, July 11, 1985 are shown in Figures 4.1 and 4.2. These analyses

(retrieved from microfilm) were originally produced by the Canadian Meteorological Centre (CMC).

The CMC 250 mb objective synoptic analysis for 0000 UTC July 11, 1985 is shown in Figure 4.1 (a). It indicates a jet<sup>1</sup> maximum just southwest of Port Hardy, B.C. (northern tip of Vancouver Island), with wind speeds in excess of 100 knots ( $50 \text{ m s}^{-1}$ ). By 1200 UTC, the CMC 250 mb analysis indicates the jet maximum over southeastern British Columbia. At this time, the jet stream axis lies in a line from central Vancouver Island to Red Deer. This position places the right exit<sup>2</sup> of the jet over the southern half of the LIMEX-85 network, a region in which subsidence prevails. The jet axis appears to lie directly over extreme northern sections of the LIMEX-85 network.

The CMC 500 mb analyses for 0000 UTC and 1200 UTC on July 11, 1985 are indicated in Figure 4.1 (c) and (d). At this level, central Alberta was under the influence of an upper ridge at 0000 UTC, with a moderate westerly flow of 25 to 35 knots. By 1200 UTC, the upper ridge was beginning to collapse over western Alberta as a short wave trough approached from British Columbia.

The 500 mb absolute vorticity analyses, shown in Figure 4.3, were locally produced at the Alberta Weather Centre. The 0000 UTC analysis indicates a vorticity

---

<sup>1</sup> A *jet* is an "intense", "narrow", quasi-horizontal current of wind which is associated with "strong" vertical shear (Reiter, 1961). By "intense" we usually mean at least  $30 \text{ ms}^{-1}$  for the upper portions of the troposphere (Berggren, et al., 1958). A "narrow" current is one whose width is approximately half to an order of magnitude less than its length. "Strong" vertical shear is at least  $5\text{--}10 \text{ ms}^{-1} \text{ km}^{-1}$ . An isotach maximum embedded within a jet is called a *jet streak* (Palmén and Newton, 1969). From Bluestein, (1984).

<sup>2</sup> The wind speed in a jet streak is faster than the speed with which the jet streak moves. Therefore the region downstream from a jet streak, where air parcels decelerate, is called the *exit region*; the region upstream from a jet streak, where air parcels accelerate is called the *entrance region*. The further subdivision of a jet streak into the *left* and *right sections* is often used, and is valid for an observer facing the downstream direction (Bluestein, 1984).

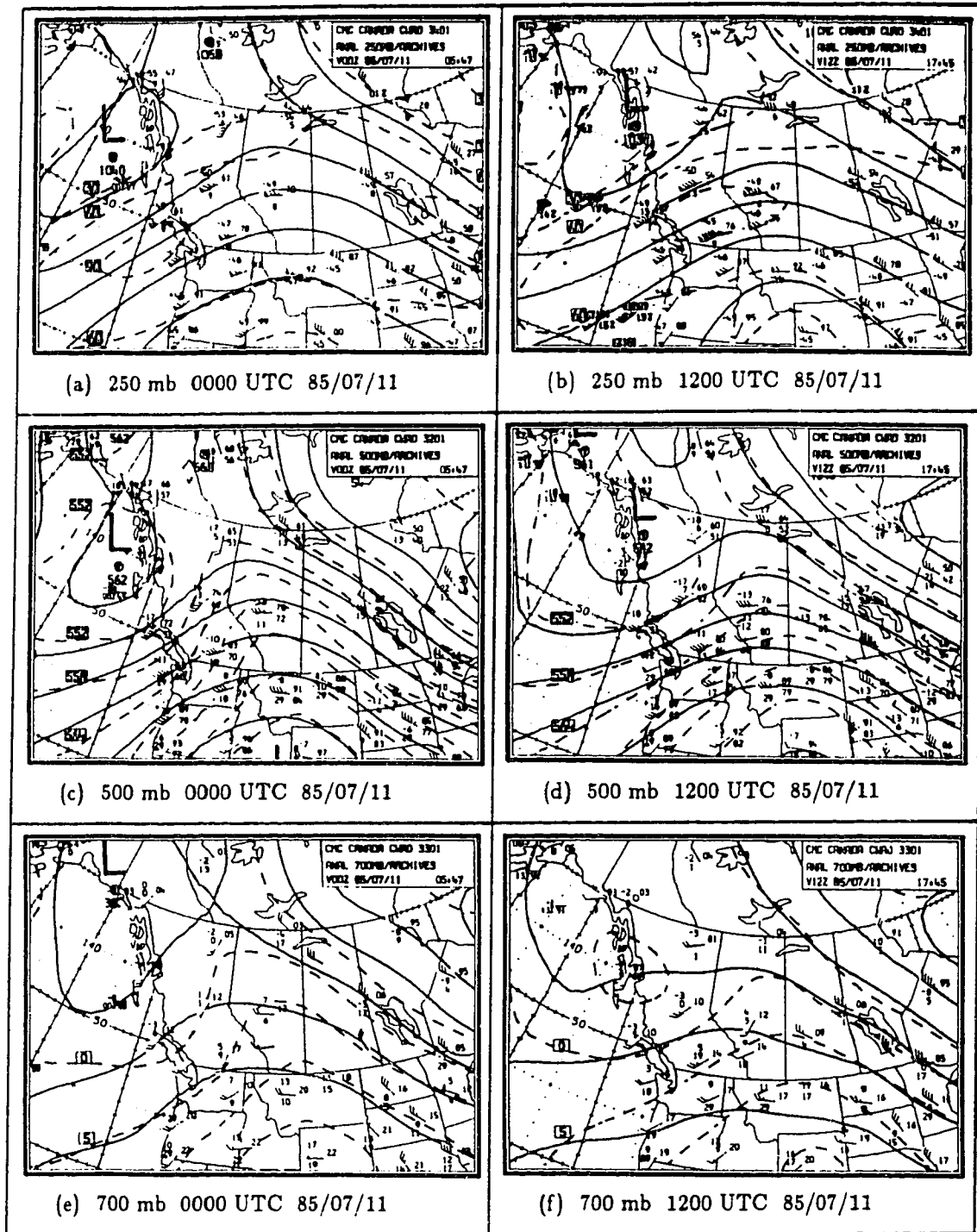


Figure 4.1: Canadian Meteorological Centre (CMC) objective synoptic analyses of the mid- and upper-troposphere. Valid time 0000 UTC and 1200 UTC, July 11, 1985.



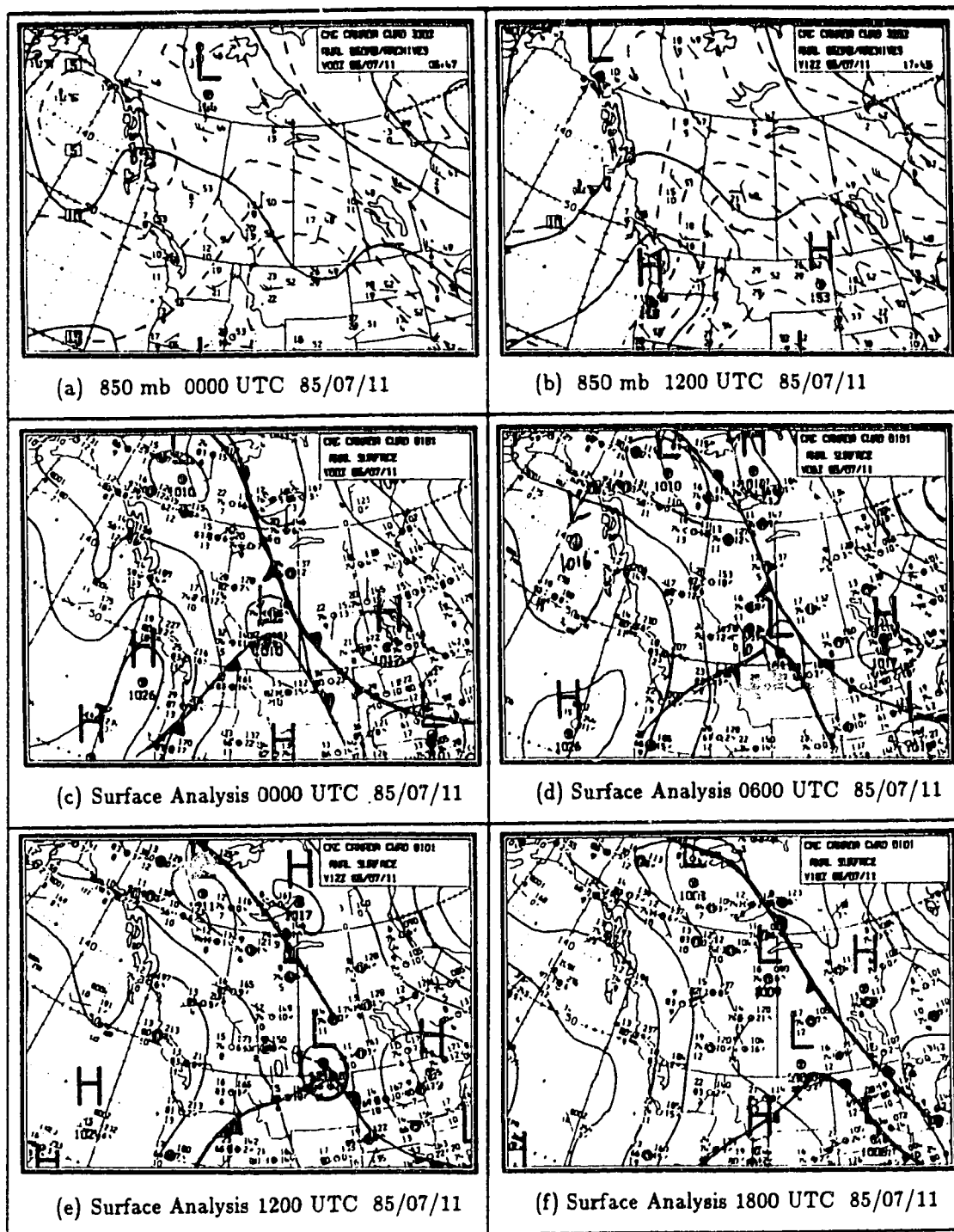


Figure 4.2: Canadian Meteorological Centre (CMC) objective synoptic analyses of the lower-troposphere. Valid time 0000 UTC and 1200 UTC, July 11, 1985.

minimum over east-central British Columbia (in the left entrance of the 250 mb jet). This centre moved eastward at 15 to 20 knots and was just west of Red Deer at 1200 UTC. To the west of this feature, at 0000 UTC, a vorticity maximum was analyzed north of Vancouver Island (note due to the lack of data west of British Columbia the analyzed position of the vorticity maximum is questionable). A trough extended southeast from the maximum along the British Columbia coast. Strong positive vorticity advection, normally associated with large scale ascent, is indicated over central British Columbia associated with this trough and vorticity maximum. At 1200 UTC, the vorticity maximum appeared to remain quasi-stationary north-west of Vancouver Island; however, the trough moved eastward over southern British Columbia and weakened. The reduction in the strength of the positive vorticity advection over central British Columbia can be noted.

The CMC 700 mb analyses are shown in Figure 4.1 (e) and (f). These analyses indicate that the thermal ridge, lying through central Alberta at 0000 UTC, moved eastward to lie along the Alberta-Saskatchewan border by 1200 UTC. The figures also exhibit a west to southwesterly flow over central Alberta on the morning of July 11.

The CMC surface analyses at 0000 UTC, 0600 UTC, 1200 UTC, and 1800 UTC 11 July, are shown in Figure 4.2 (c), (d), (e), and (f), respectively. The 0000 UTC analysis indicates a 1010 mb low pressure system near Calgary, with a weak trough of low pressure extending north and southward from the low pressure centre. By 0600 UTC, the low has moved into southwestern Saskatchewan, (moving at a speed of 25 knots), leaving an amorphous trough of low pressure over Alberta.

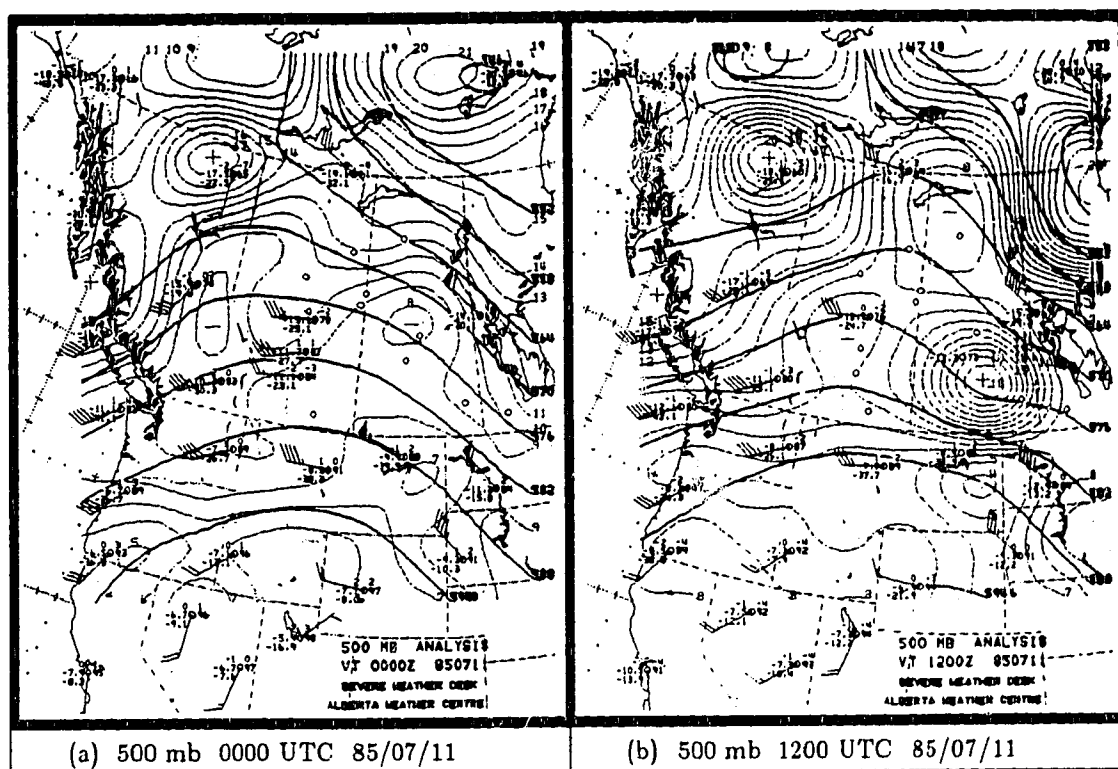


Figure 4.3: Alberta Weather Centre 500 mb analysis for July 11, 1985 at 0000 UTC (a) and 1200 UTC (b). Heavy solid lines are height contours. Light dashed lines are contours of absolute vorticity (in increments of  $1 \times 10^{-5} \text{s}^{-1}$ ). A "+" indicates a vorticity maximum and a "-" indicates a vorticity minimum.

At 1200 UTC, this weak trough is in a northwest to southeast line through the province. A ridge of high pressure appears to be pushing into Alberta from central British Columbia. By 1800 UTC the trough of low pressure extends from the low in southern Saskatchewan to another weak low near Fort McMurray.

Both the CMC surface analyses indicate a maritime frontal wave associated with the low pressure system that moved from southern Alberta into southern Saskatchewan. The CMC 850 mb analyses at 0000 UTC and 1200 UTC (Figure 4.2 (a) and (b)), indicate a relatively strong baroclinic zone associated with this front. The 850 mb analyses also support the CMC surface frontal positions (which are done subjectively).

Enhanced convective activity developed over northern sections of the LIMEX-85 network shortly after 0000 UTC July 12, 1985 (see Figure 4.12). The CMC synoptic objective analyses for this "mature" storm period are shown in Figure 4.4. At 250 mb, the west-southwest jet axis (with winds in excess of 100 knots) is analyzed along a line from central Vancouver Island to Red Deer. This quasi-stationary position has likely maintained continuous positive synoptic scale vertical motion north of the jet axis, while subsidence prevailed south of it.

The mid-tropospheric conditions (Figure 4.4 (b) and (c)), indicate a persistent westerly flow over south-central Alberta. The CMC analyses of the lower troposphere (Figure 4.4 (d), (e), and (f)), indicate that the trough extending through northern Alberta (from the low in southern Saskatchewan) has remained quasi-stationary. This pattern would suggest a persistent, weak cyclonic flow over central Alberta. However, it is also noteworthy to mention that the pressure gradients are

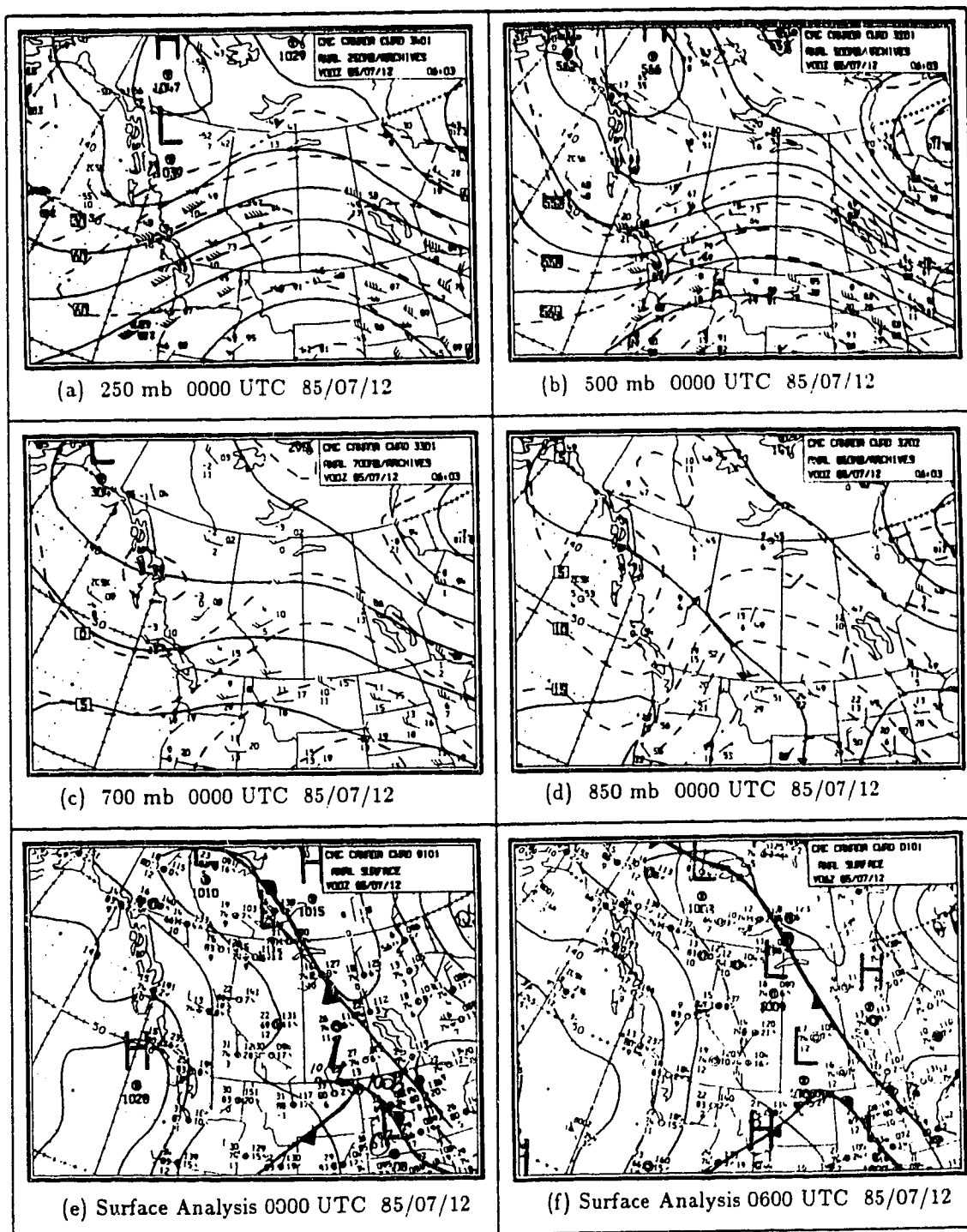


Figure 4.4: Canadian Meteorological Centre (CMC) objective synoptic analyses during the mature storm period. Valid time 0000 UTC July 12, 1985.

weak and the surface pressure pattern is somewhat amorphous.

Summarizing, the key features of the synoptic scale analyses are:

- a jet maximum, with speeds in excess of 100 knots, over the extreme northern section of the LIMEX-85 area;
- a weak area of positive vorticity advection approaching from central British Columbia;
- a west-southwesterly flow in the mid- to upper troposphere;
- a weak cyclonic flow over central Alberta in the lower troposphere.

The general synoptic pattern for July 11, especially the upper trough - surface low combination, fit the typical patterns described by Strong (1985, 1986) as being most favourable for severe convective storms over central Alberta.

## **4.2 Mesoscale Stability Analysis**

The spatial objective mesoscale analysis of the Lifted Index, for 1500 UTC July 11, 1985, is shown in Figure 4.5. This figure indicates that the southwestern corner of the LIMEX region was very stable early in the day, with Lifted Indices greater than +3. It also suggests that the region northwest of Ram Lookout is unstable. Recall that Lifted Indices of less than zero indicate that thunderstorms are likely (refer to Table 2.1). The validity of the analysis in this data sparse region might be questioned, however. The extreme northeastern section of the LIMEX-85 network also appears to be unstable with a Lifted Index less than -1 at Red Deer. The remainder of the region is marginally unstable, with Lifted Indices of 0 to +3

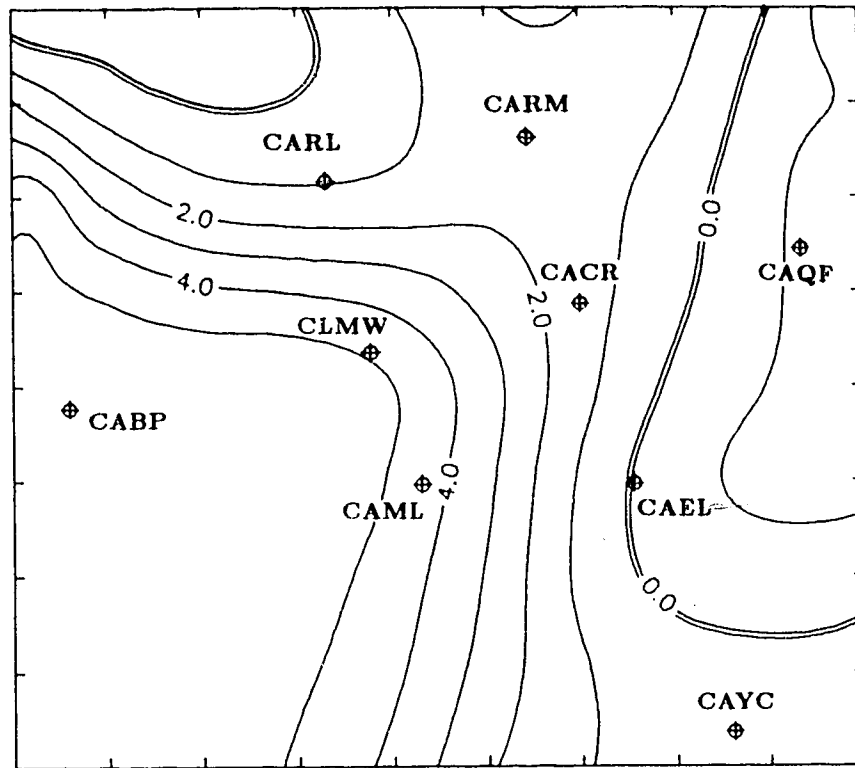


Figure 4.5: Spatial objective analysis of the Lifted Indices calculated from the LIMEX-85 upper air data. Valid for 1500 UTC (0900 MDT) July 11, 1985. The indicated grid length is 25 km. LEGEND: CABP-Bow Pass, CACR-Caroline, CAEL-Elkton, CAML-Mountaineer Lodge, CAQF-Red Deer Airport, CARL-Ram Lookout East, CARM-Rocky Mountain House, CAYC-Calgary, CLMW-Limestone Mountain West.

indicating that showers are possible later in the day.

The 1800 UTC spatial objective mesoscale analysis of the Lifted Index is shown in Figure 4.6. It is clear from this figure that the northern sections of the network have become quite unstable. The Lifted Indices at Red Deer, Rocky Mountain House, and Ram Lookout are all less than  $-2.0$ . Recall that a Lifted Index of less than  $-2$  indicates that the environment is very unstable (refer to Table 2.1) and suggests that severe thunderstorms could develop. It is also interesting to note the destabilization that has taken place at Calgary.

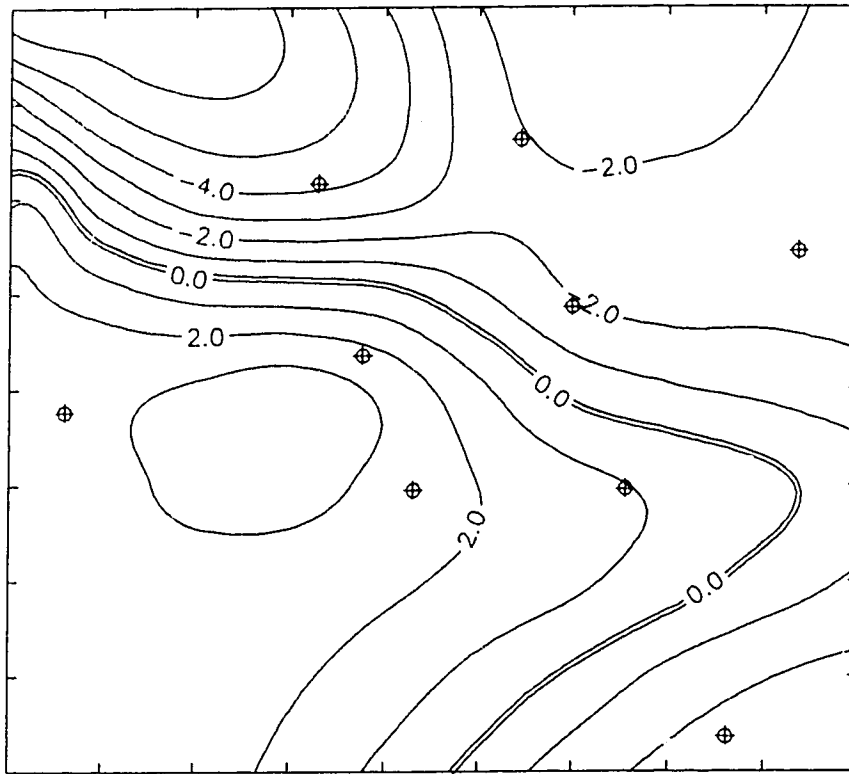


Figure 4.6: Spatial objective analysis of the Lifted Indices calculated from the LIMEX-85 upper air data. Valid for 1800 UTC July 11, 1985. The indicated grid length is 25 kilometres.



### 4.3 S-band Radar PPI Summaries

The Alberta Research Council S-band radar PPI's, Figures 4.7 through 4.18, provide a meso-*gamma* scale (storm scale) summary, at 30-minute intervals, for central Alberta on July 11. This series of summaries begins with first echoes detected northwest of Rocky Mountain House at 2200 UTC (Figure 4.7), and ends with the last decaying echoes moving away from the LIMEX-85 network at 0330 UTC, July 12 (Figure 4.18).

The series of large storms northwest of Red Deer (north of the LIMEX-85 network) was very intense with reflectivities in excess of 60 dBZ. These storms moved eastward at approximately  $40 \text{ km hr}^{-1}$ , and appeared to advance as a series of waves. These storms were 30 to 40 km north of the LIMEX-85 mesoscale network, and it is difficult to ascertain the influence they may have had on the conditions over the network.

The series of PPI summaries (Figures 4.7 through 4.18) indicate that showers initially developed over northern sections of the LIMEX-85 network after 2300 UTC. The reflectivity echoes were initially less than 30 dBZ; however, by 0100 UTC, July 12, the reflectivities increased to greater than 50 dBZ. This evolution suggests that one of the cumulus clouds (towering cumulus) giving the showers at 2300 UTC, matured to a thunderstorm by 0100 UTC. This thunderstorm then moved east-northeastward out of the network at a speed of  $40 \text{ km hr}^{-1}$ . In the wake of this storm, a "cluster" of smaller (but equally intense) storms developed south of Rocky Mountain House (marked RM on the PPI summaries). These storms also moved

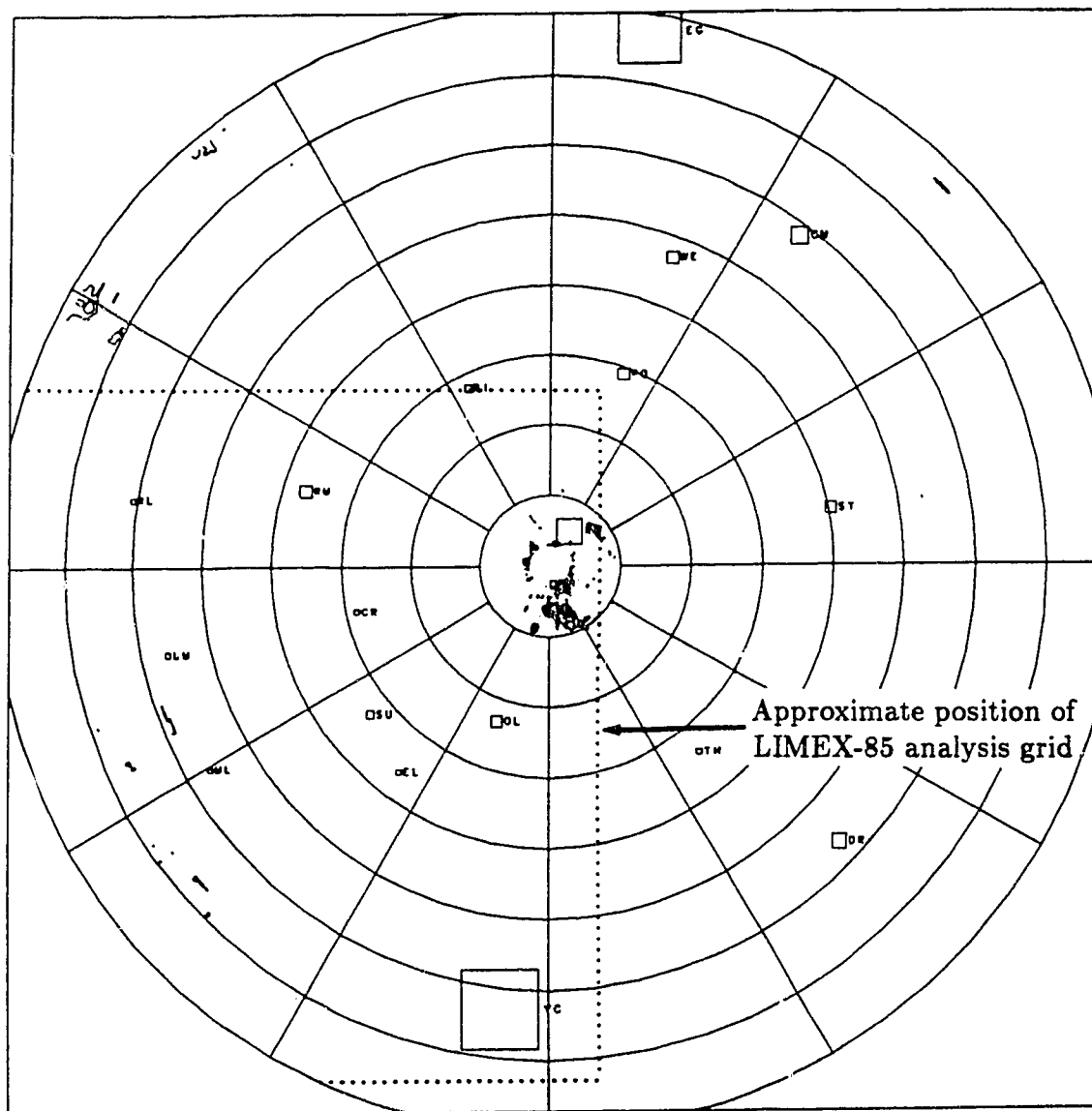


Figure 4.7: 2200 UTC S-band radar PPI summary for July 11, 1985; (1600 MDT July 11, 1985). Indicated distance rings are spaced at 20 km. Reflectivities are contoured in intervals of 10 dBZ starting at 20 dBZ. Radar elevation angle is approximately  $1.5^\circ$ .

LEGEND: RM-Rocky Mountain House, RL-Ram Lookout, LM-Limestone Mountain, CR-Caroline, ML-Mountaineer Lodge, EL-Elkton, C-Calgary.

NOTE: The echoes in the southwest quadrant (near Mountaineer Lodge) are radar reflections off mountains.

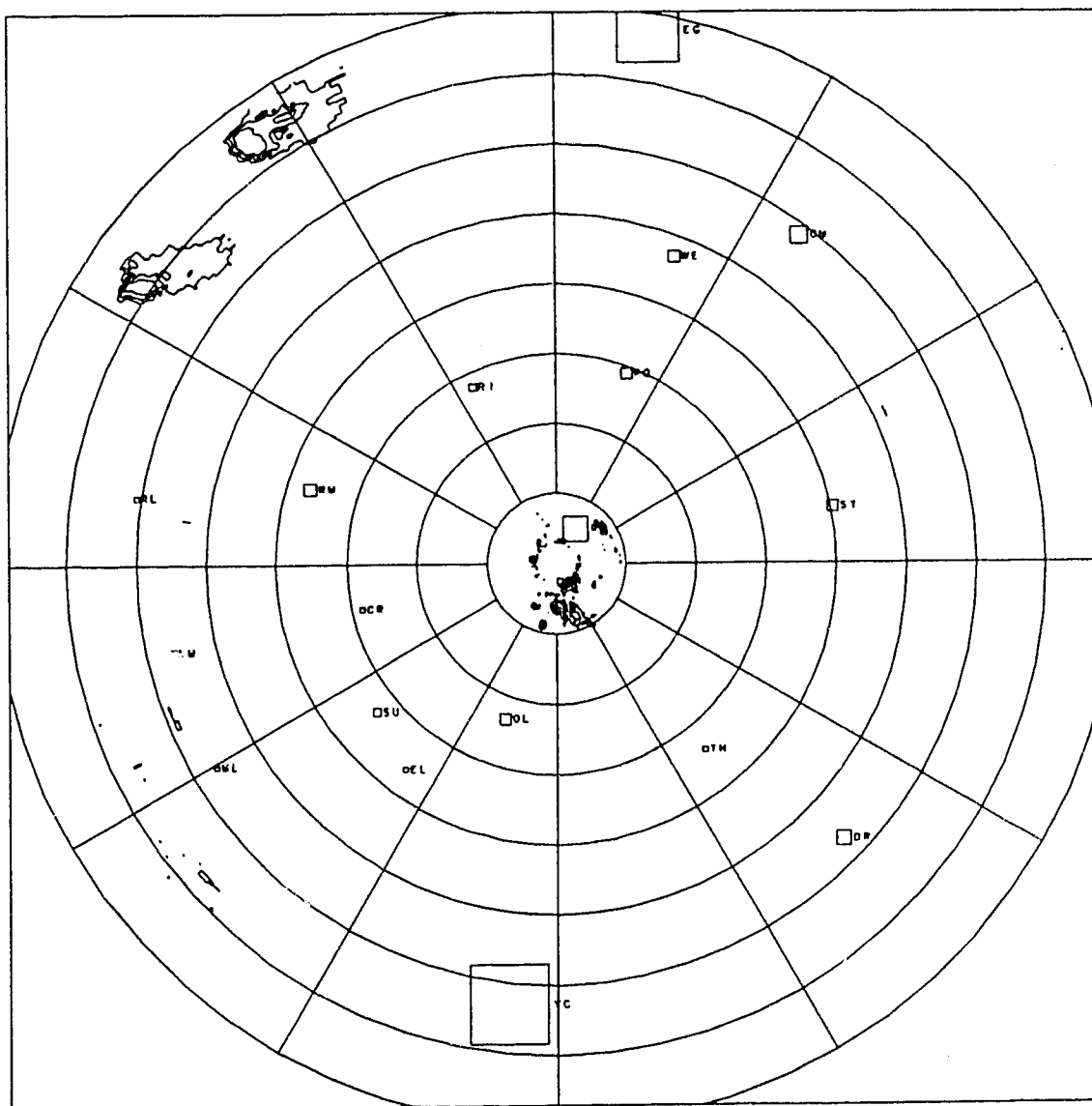


Figure 4.8: 2230 UTC S-band radar PPI summary for July 11, 1985; (1630 MDT July 11, 1985). Indicated distance rings are spaced at 20 km. Reflectivities are contoured in intervals of 10 dBZ starting at 20 dBZ. Radar elevation angle is approximately 1.5°.

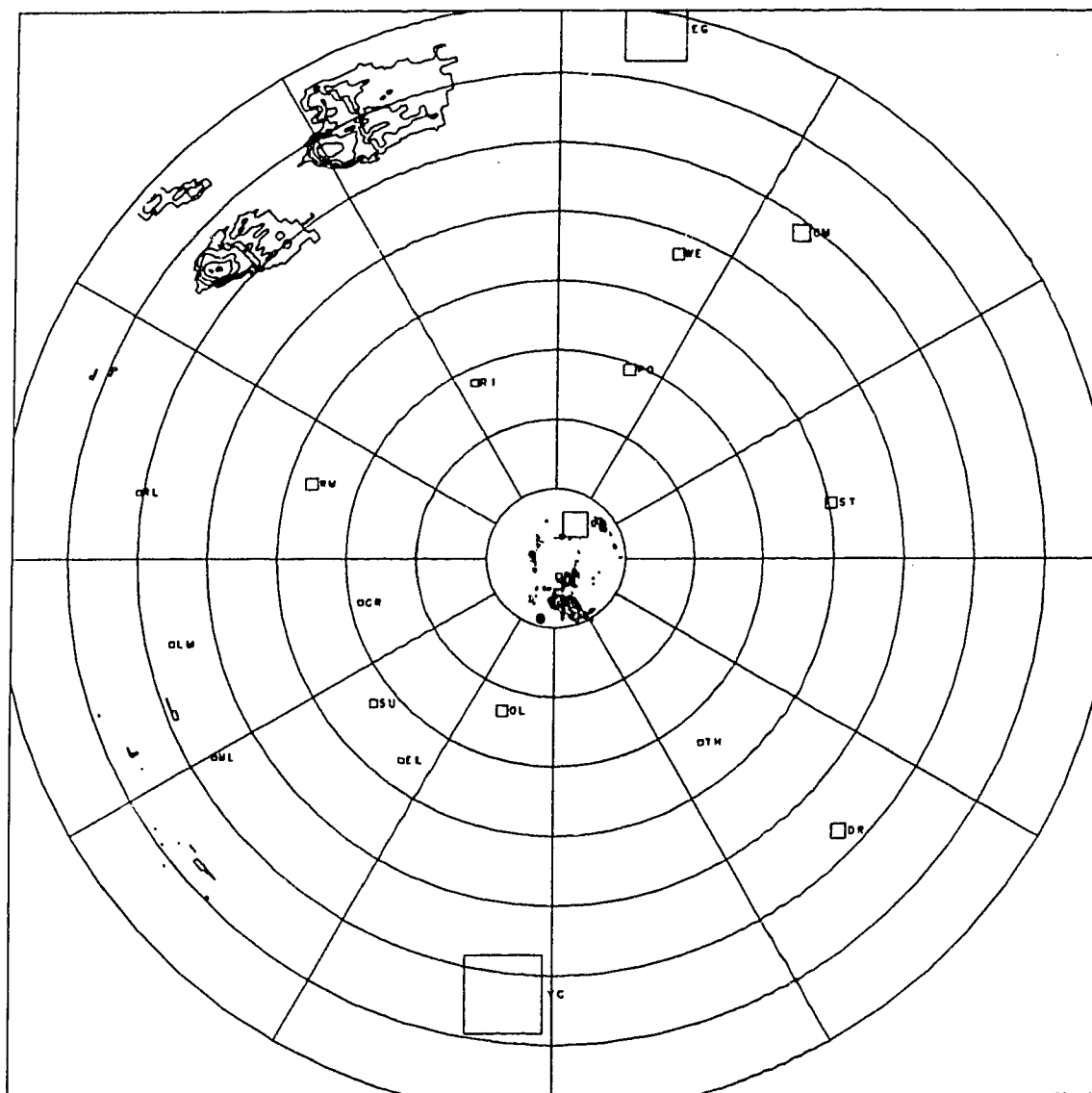


Figure 4.9: 2300 UTC S-band radar PPI summary for July 11, 1985; (1700 MDT July 11, 1985). Indicated distance rings are spaced at 20 km. Reflectivities are contoured in intervals of 10 dBZ starting at 20 dBZ. Radar elevation angle is approximately 1.5°.

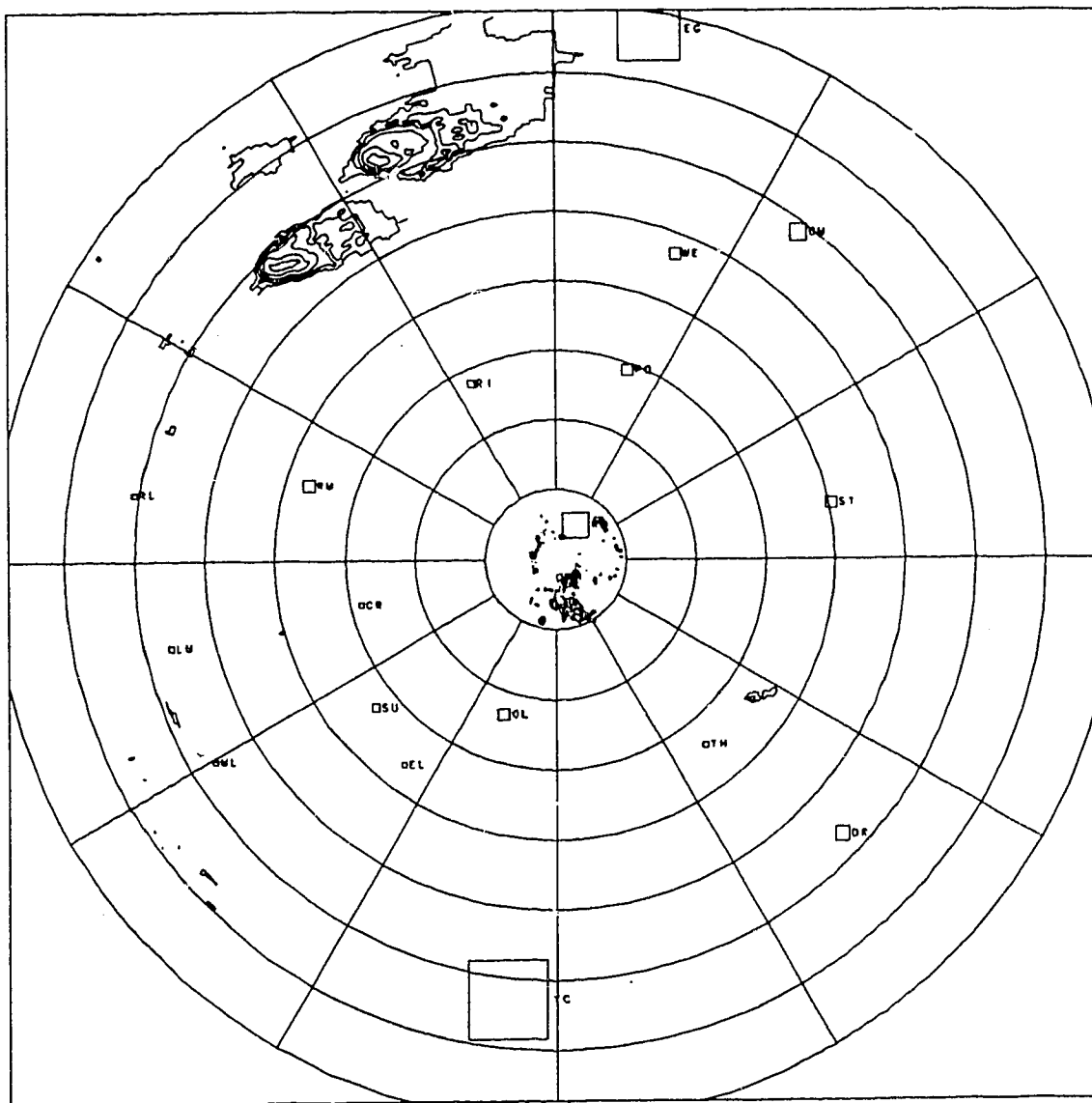


Figure 4.10: 2330 UTC S-band radar PPI summary for July 11, 1985; (1730 MDT July 11, 1985). Indicated distance rings are spaced at 20 km. Reflectivities are contoured in intervals of 10 dBZ starting at 20 dBZ. Radar elevation angle is approximately  $1.5^{\circ}$ .

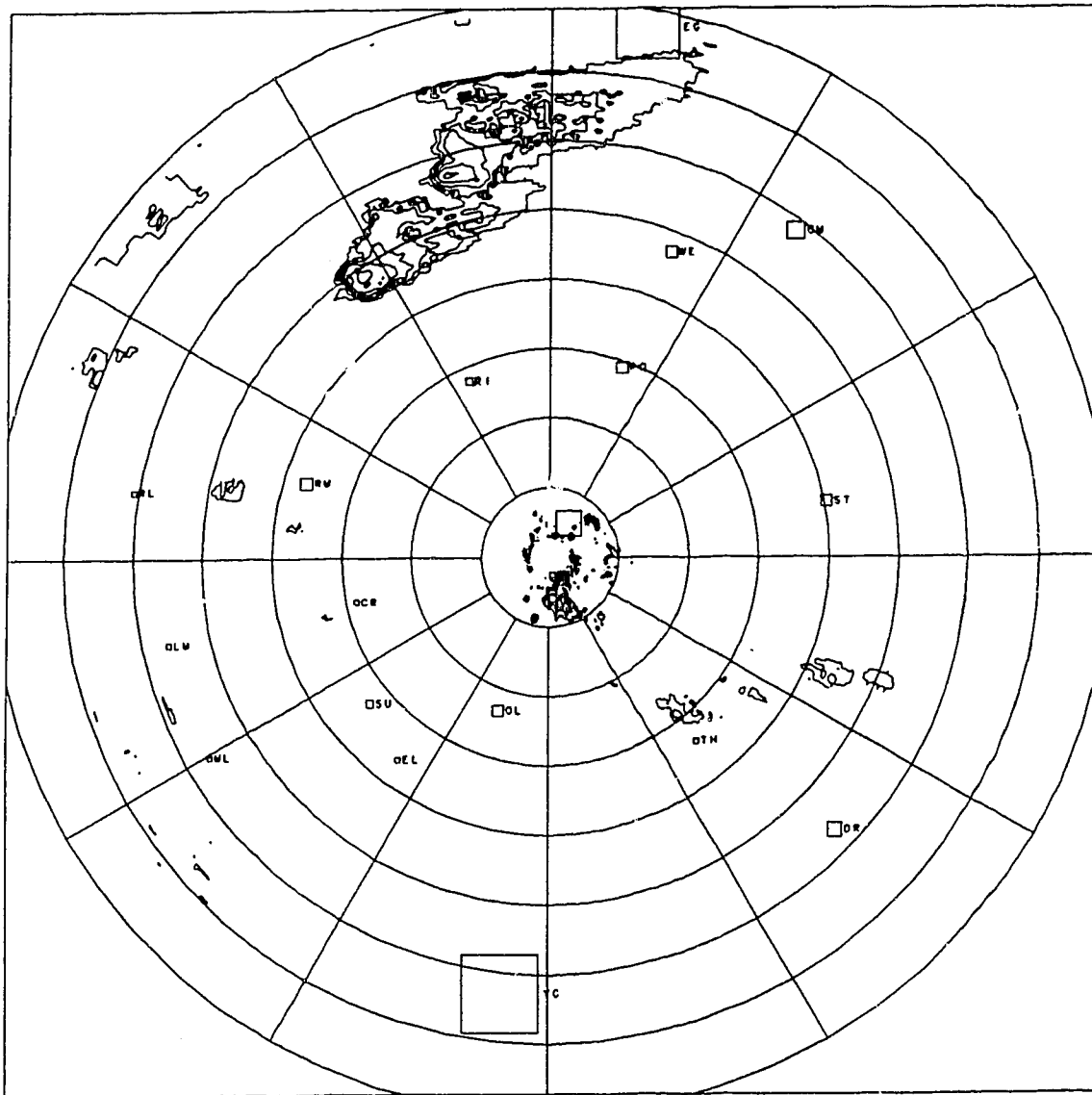


Figure 4.11: 0000 UTC S-band radar PPI summary for July 12, 1985; (1800 MDT July 11, 1985). Indicated distance rings are spaced at 20 km. Reflectivities are contoured in intervals of 10 dBZ starting at 20 dBZ. Radar elevation angle is approximately 1.5°.

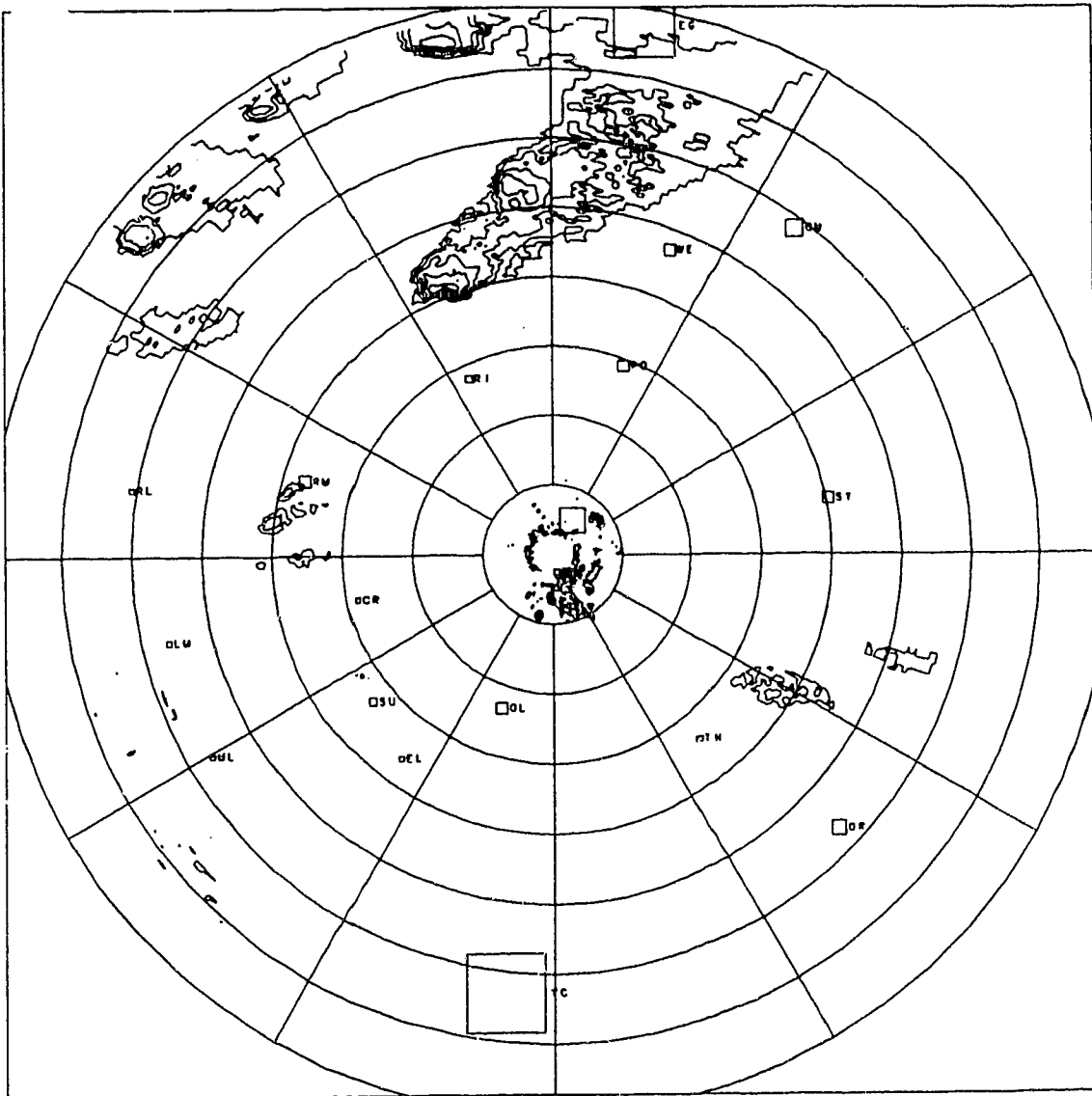


Figure 4.12: 0030 UTC S-band radar PPI summary for July 12, 1985; (1830 MDT July 11, 1985). Indicated distance rings are spaced at 20 km. Reflectivities are contoured in intervals of 10 dBZ starting at 20 dBZ. Radar elevation angle is approximately 1.5°.

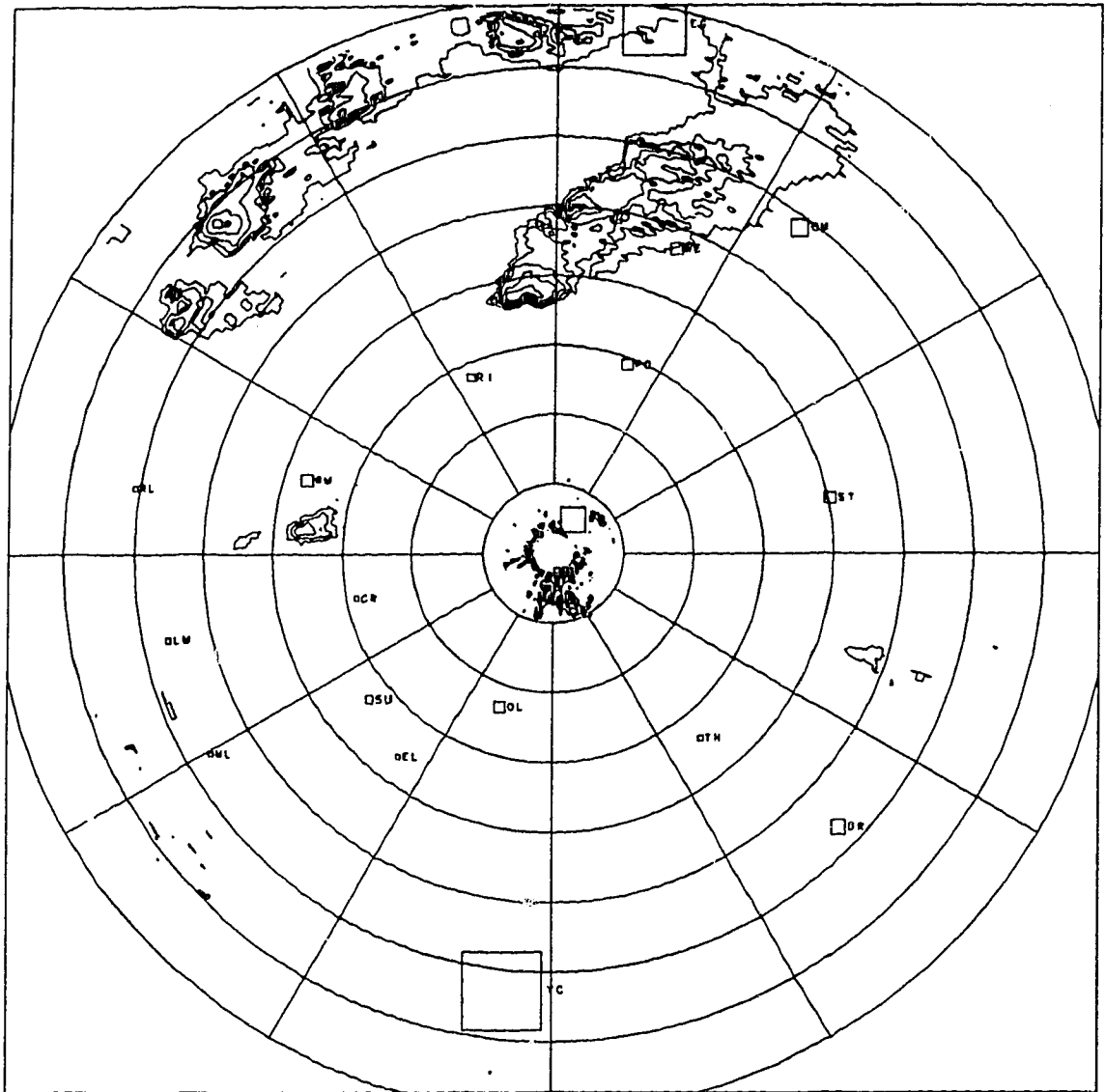


Figure 4.13: 0100 UTC S-band radar PPI summary for July 12, 1985; (1900 MDT July 11, 1985). Indicated distance rings are spaced at 20 km. Reflectivities are contoured in intervals of 10 dBZ starting at 20 dBZ. Radar elevation angle is approximately 1.5°.



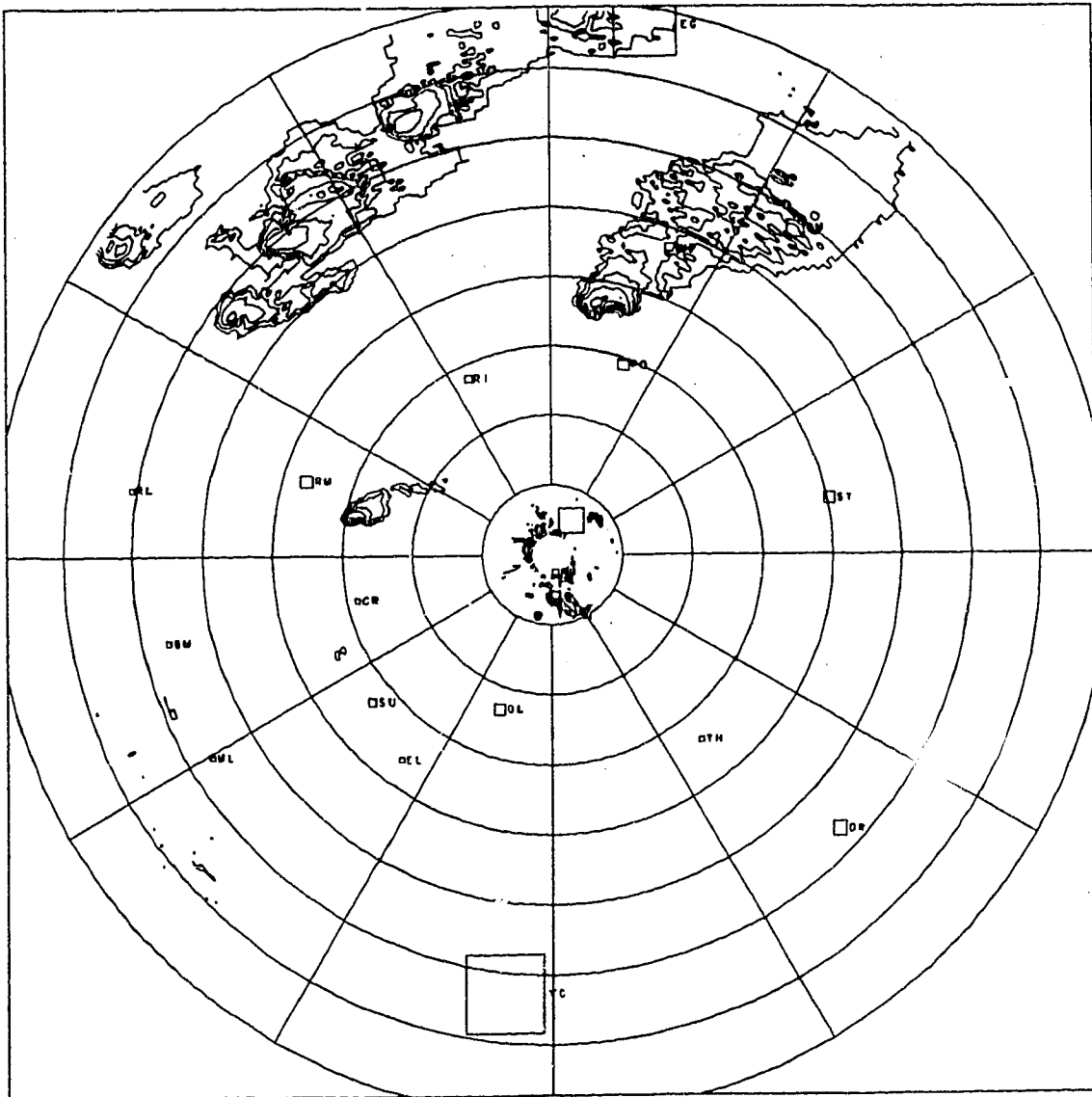


Figure 4.14: 0130 UTC S-band radar PPI summary for July 12, 1985; (1930 MDT July 11, 1985). Indicated distance rings are spaced at 20 km. Reflectivities are contoured in intervals of 10 dBZ starting at 20 dBZ. Radar elevation angle is approximately 1.5°.

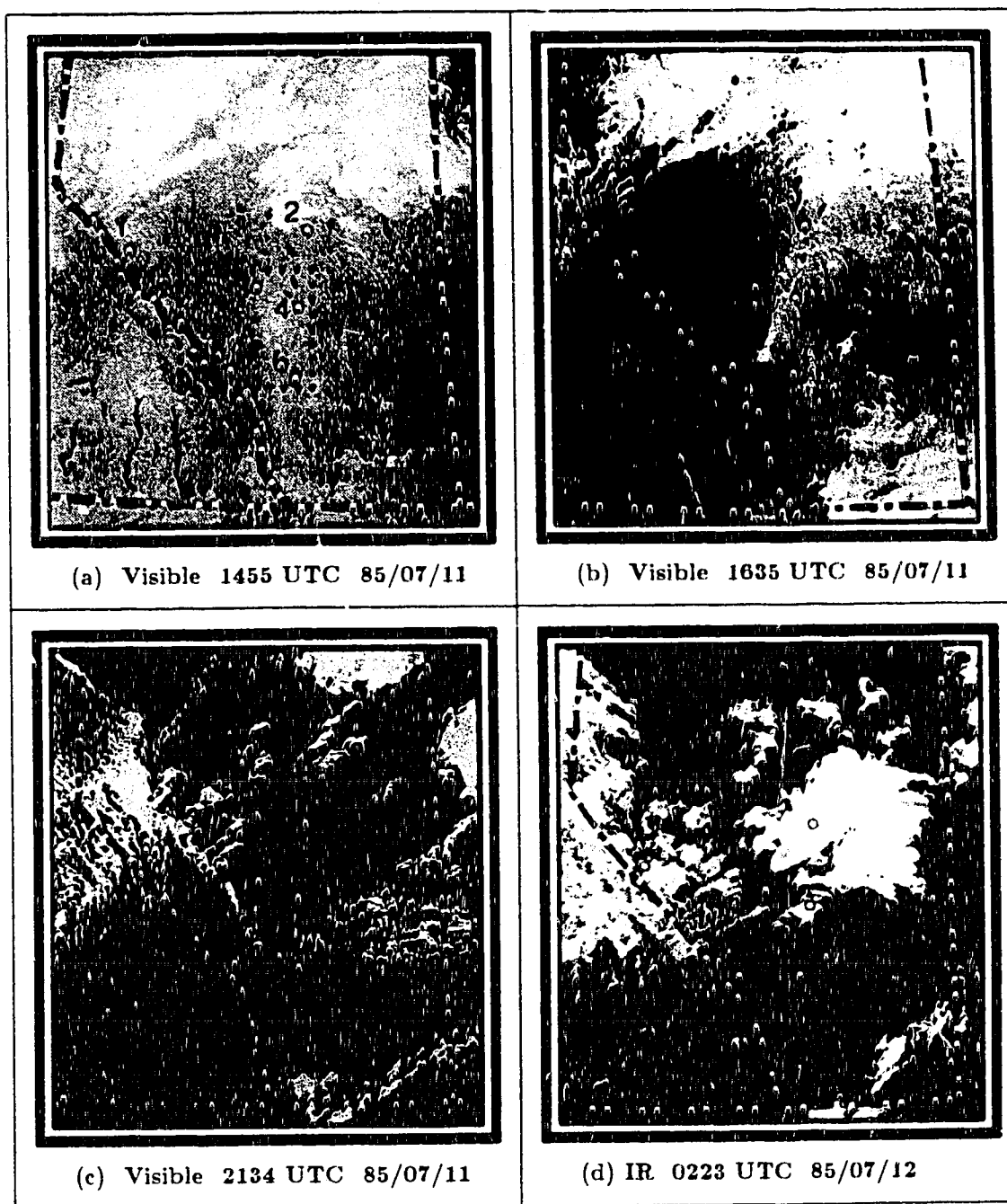


Figure 4.19: NOAA satellite imagery for July 11, 1985. The dotted rectangular box denotes the approximate location of the LIMEX-85 analysis grid. The numbered sites denote AES surface synoptic sites at: (1) Jasper, (2) Edmonton, (3) Rocky Mountain House, (4) Red Deer, (5) Banff, and (6) Calgary.

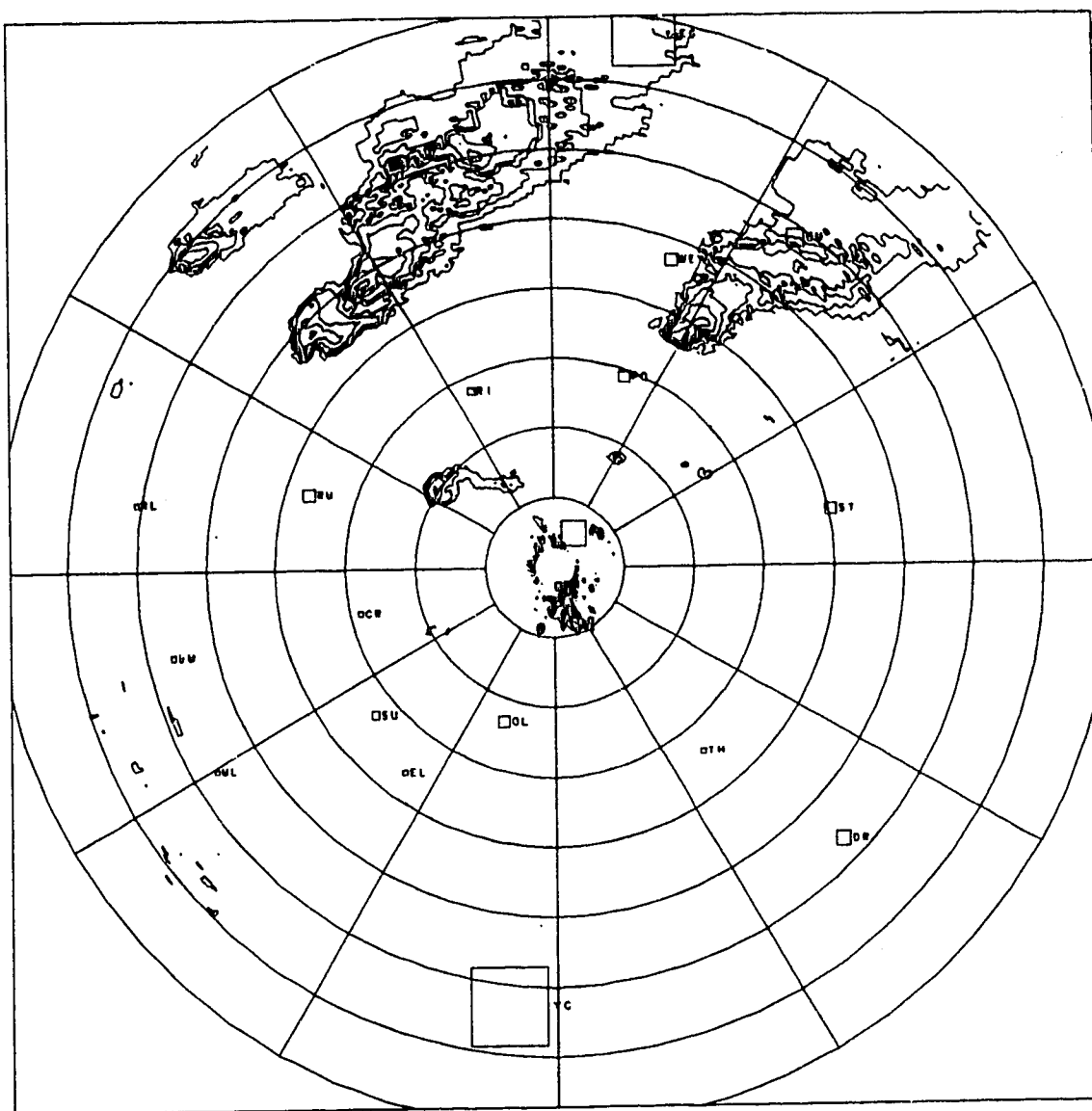


Figure 4.15: 0200 UTC S-band radar PPI summary for July 12, 1985; (2000 MDT July 11, 1985). Indicated distance rings are spaced at 20 km. Reflectivities are contoured in intervals of 10 dBZ starting at 20 dBZ. Radar elevation angle is approximately 1.5°.

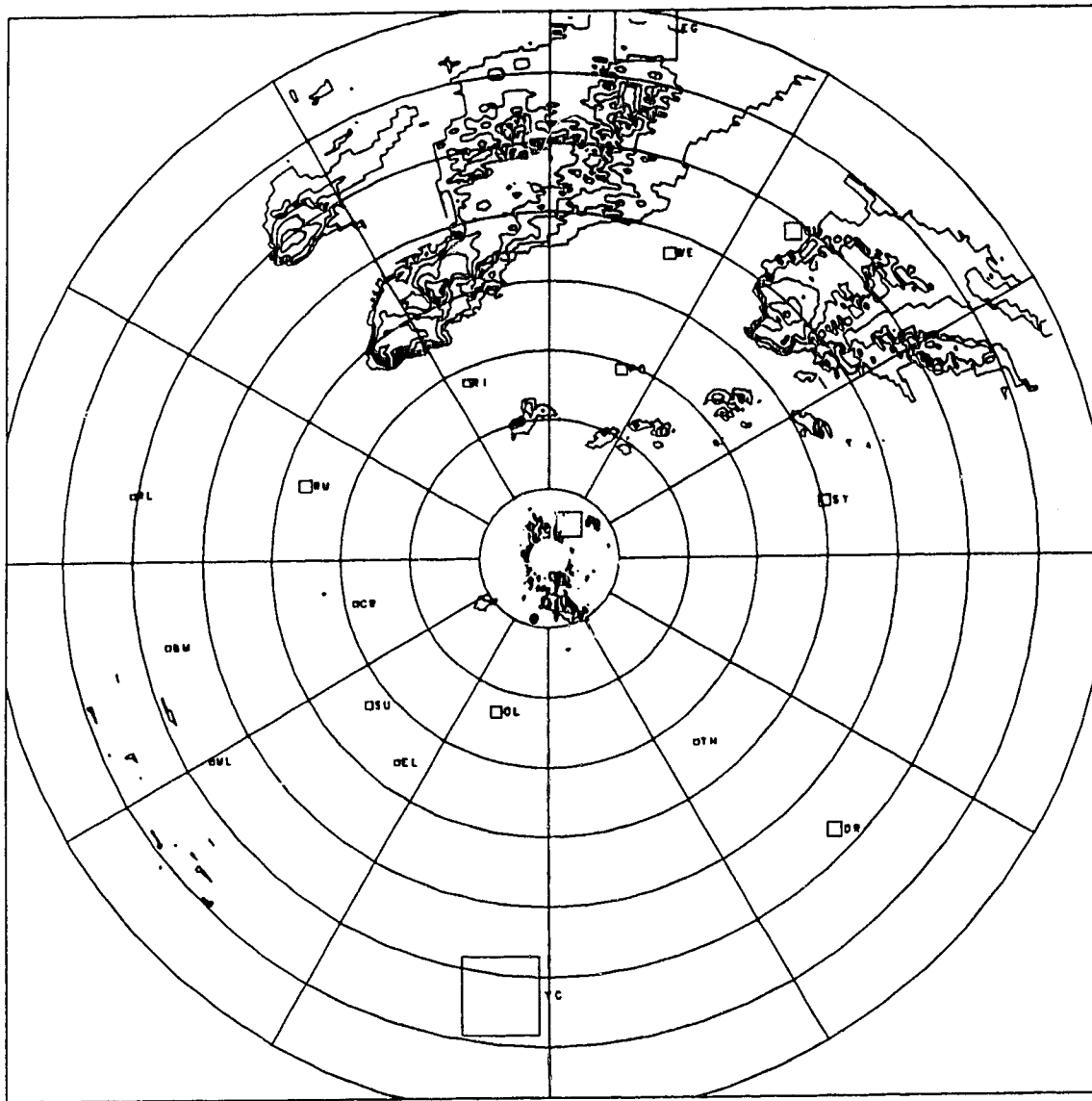


Figure 4.16: 0230 UTC S-band radar PPI summary for July 12, 1985; (2030 MDT July 11, 1985). Indicated distance rings are spaced at 20 km. Reflectivities are contoured in intervals of 10 dBZ starting at 20 dBZ. Radar elevation angle is approximately 1.5°.

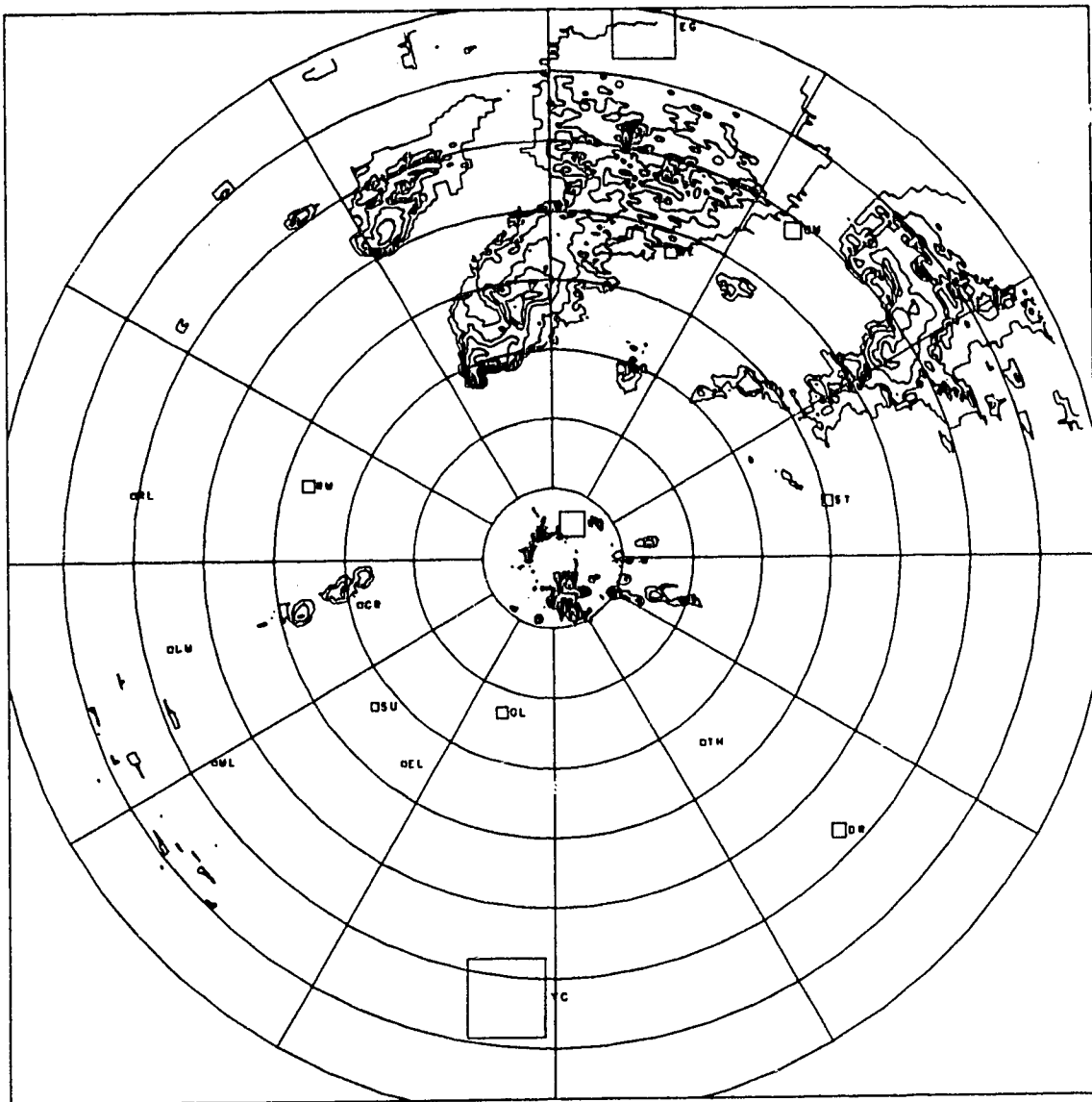


Figure 4.17: 0300 UTC S-band radar PPI summary for July 12, 1985; (2100 MDT July 11, 1985). Indicated distance rings are spaced at 20 km. Reflectivities are contoured in intervals of 10 dBZ starting at 20 dBZ. Radar elevation angle is approximately 1.5°.

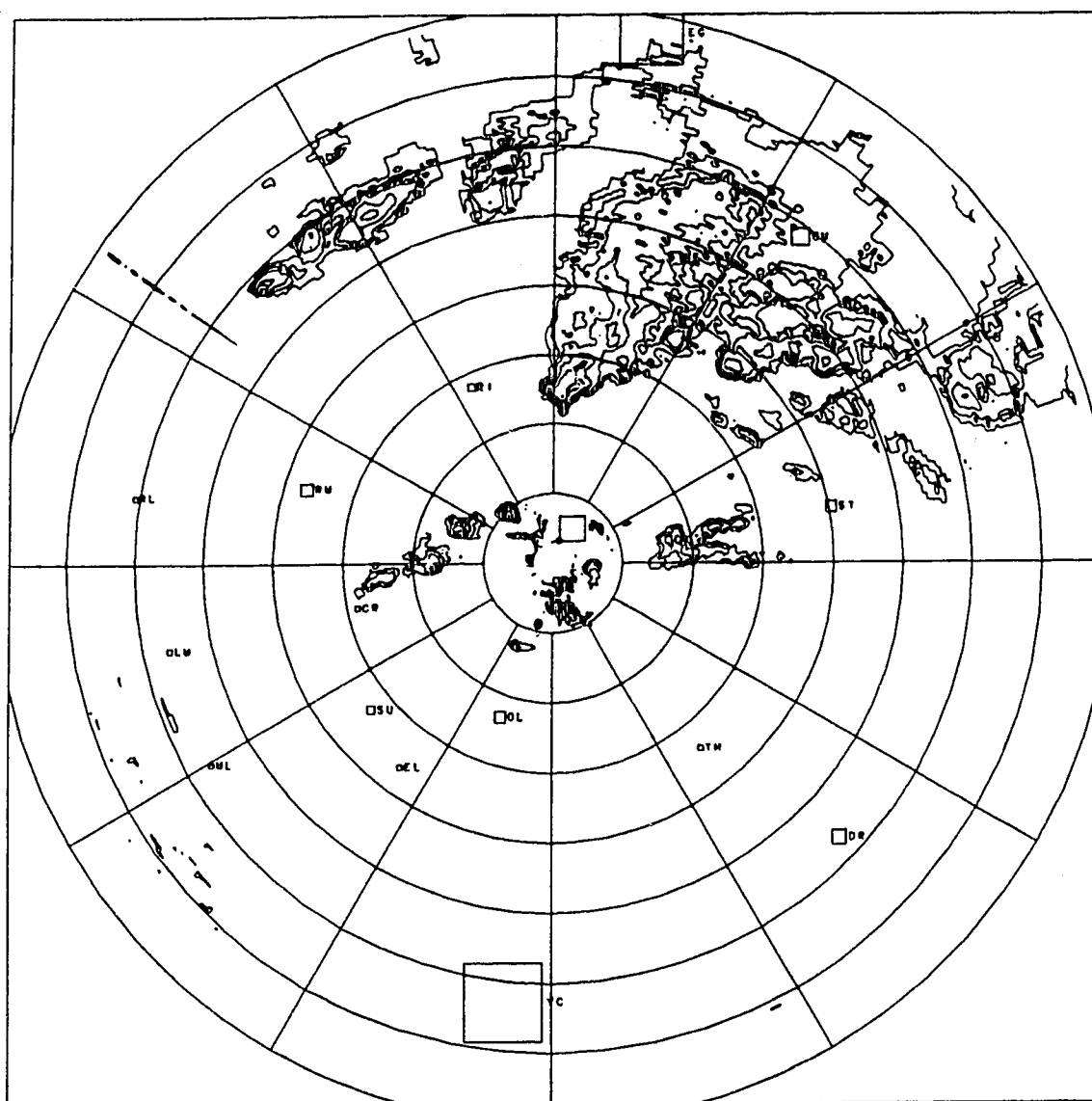


Figure 4.18: 0330 UTC S-band radar PPI summary for July 12, 1985; (2130 MDT July 11, 1985). Indicated distance rings are spaced at 20 km. Reflectivities are contoured in intervals of 10 dBZ starting at 20 dBZ. Radar elevation angle is approximately 1.5°.

east-northeastward.

It is interesting to observe the evolution of the "cluster" of thunderstorms that developed over the network after 0200 UTC. The S-band radar PPI summary for 0230 UTC is shown in Figure 4.16. At this time a small and very weak echo, with a maximum reflectivity near 20 dBZ, was detected approximately 40 km south of Rocky Mountain House. Within 30 minutes, (Figure 4.17), four distinct cells were observed in the same location, with a maximum reflectivity in excess of 40 dBZ. The rapid change in size, and intensity of these echoes suggest that the associated convective cloud is developing quickly. Dr. G. Strong, directing LIMEX-85 operations from Limestone Mountain Ridge, took time lapse photographs of this event, and noted precipitation from the base of the cloud (personal communication). The Caroline (CACR) upper air site also indicated precipitation in the area in its recorded surface observations, while detailed radar data revealed some bin values in excess of 50 dBZ for this storm. It is also noteworthy that these storms appeared to develop in a region where the Lifted Index was less than  $-2$  (refer to Figure 4.6).

At 0330 UTC, shown in Figure 4.18, the "cluster" of echoes detected south and slightly southeast of Rocky Mountain House at 0300 UTC continues to develop and intensify. They appear as a line of cells, each cell having reflectivities in excess of 50 dBZ. This line stretches from 35 km southeast of Rocky Mountain House to 20 km northwest of the Red Deer radar. The line is almost parallel to the trajectory of the storm that tracked northeastward over the same area 2 hours earlier.

Relating the results of the PPI diagnostics to the previous synoptic scale analyses and the mesoscale stability analyses, one notes two distinct relationships. The

1800 UTC spatial objective analysis of the Lifted Index field suggested that only the northern and extreme eastern sections of the LIMEX-85 network were unstable. The position of the 250 mb jet streak (in an east - west line through Red Deer), implied that southern sections of the mesoscale network were under the influence of synoptic scale subsidence while the northern sections were under the influence of synoptic scale ascent. The radar PPI summaries reveal that all thunderstorm activity was restricted to the northern portions of the LIMEX-85 network.

#### **4.4 Mesoscale Analysis of Satellite Imagery**

The satellite images presented in this section were taken by NOAA 8, a polar orbiting satellite that is capable of taking both visible and infra-red (IR) imagery. The provincial and international borders as well as the location of six AES stations have been noted to assist the reader. Due to an oversight, the digital satellite data were not archived; consequently, it is not possible to perform a detailed mesoscale analysis of the cloud formations during the LIMEX-85 period. In future studies, every effort should be made to acquire this high resolution data. The limited number of satellite images presented were obtained from the Alberta Weather Centre of the Atmospheric Environment Service. The author apologizes for the sub-standard quality of these "operational" satellite images.

Figure 4.19 provides a large-scale perspective of the evolution of the cloud development over southern Alberta on July 11. During the early morning hours, clear sky conditions prevailed over the LIMEX-85 network. By mid-afternoon, a band of cumuliform cloud developed along the lee side of the Rockies, over western sections



of the LIMEX-85 network. Several hours later, the imagery indicates the presence of thunderstorms between Rocky Mountain House and Edmonton. The imagery also reveals relatively clear conditions prevailing over the southern portions of the experimental area (south of Red Deer). At this time, the position of the nearly zonal jet axis was in the vicinity of Red Deer. The satellite imagery indicates that all the convective activity is occurring in the vicinity and to the north of the jet axis. It also reveals that the band of cumuliform cloud between Rocky Mountain House and Banff appears to have formed in an arc in the immediate lee of the Rockies.

In the following section, the author will perform a diagnosis of the mesoscale vertical velocity fields in the pre- and early storm period. It has been demonstrated by Strong (1986) and others that, at least in some instances, such as the SESAME cases, pronounced positive vertical motion may be prevalent in the atmosphere up to 6 hours prior to the storm event. One of the objectives of this study is to determine whether such pre-storm dynamics are present for initiating Alberta convective storms.

#### **4.5 Mesoscale Vertical Motion Fields**

Mesoscale vertical velocity fields were objectively analyzed at 50 mb intervals from 800 to 600 mb, inclusive, for 2 hour intervals from 1700 UTC to 0100 UTC. The late morning (1700 UTC) vertical motion fields, shown in Figure 4.20, are characterized by general ascent over regions east of the foothills, no doubt due to synoptic scale influences such as the surface troughing north-south through eastern Alberta (Figure 4.2). This pattern is interrupted by relatively strong subsidence near 750 mb,

just above the capping lid (e.g., see tephigram in Figure 4.21). Given the upper flow at this time and the proximity of the main mountain barrier, it is likely that this subsidence is primarily orographically-induced.

By early afternoon (1900 UTC), this orographic subsidence is gradually giving way to small cells of ascent over northern sections of the LIMEX-85 network, again with maximum values of around  $10 \text{ cm s}^{-1}$  at 750 mb (see Figure 4.22). These well defined cells of ascent appeared approximately 6 hours prior to the development of convective precipitation; recall, that the first significant radar echoes appeared to develop over northern portions of the LIMEX network near 0100 UTC, July 12 (see Figure 4.13). Inspection of the soundings in Figure 4.21 reveals that the capping lid is weakening over the northern sites as well, no doubt due to cooling caused by the ascent. It is not possible, in this analysis, to ascertain with confidence whether the ascent originates from upslope flow (orographic lift), or a strengthening of the larger (synoptic) scale positive vertical motion associated with the trough of low pressure.

By mid-afternoon (2100 UTC), the region of ascent has strengthened further but appears to be moving northward out of the LIMEX-85 network (see Figures 4.23). A small but relatively strong centre of ascent remains in the region between Limestone Mountain and Caroline where the small storm discussed in Section 4.3 forms shortly afterward<sup>3</sup>. However, strong orographic (and possibly synoptic scale) subsidence

---

<sup>3</sup> Strong (personal communication) notes that "the fact that the Caroline storm is intense, but small and rather short-lived, can probably be explained on the basis of this vertical velocity analysis alone. It remains, however, to confirm this suspicion through other analyses such as low-level convergence. It is noteworthy that this case agrees quite well with the conceptual model of Alberta convective storms as hypothesized by Strong (1985, 1986)."



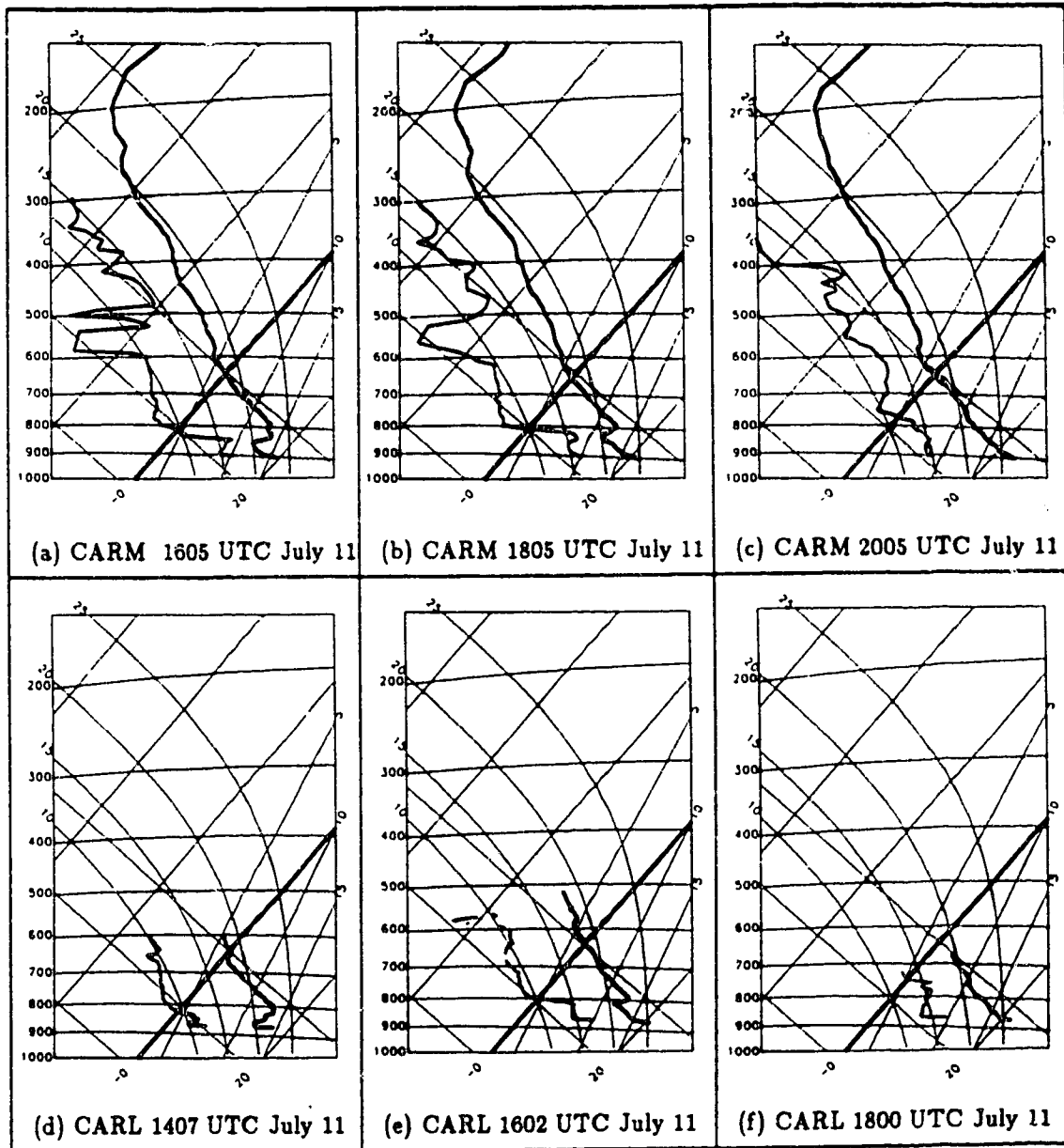


Figure 4.21: Serial soundings from Ram Lookout (CARL) and Rocky Mountain House (CARM). The bold "curve" is the dry bulb temperature profile while the "curve" to its left is the dew point temperature profile. The CARL soundings were generally abandoned above 600 mb.



is being re-established over the western part of the LIMEX-85 region, while, as near as can be determined, most of the mesoscale ascent has moved northward, where a rather large, intense thunderstorm forms a few hours later (see radar PPI summaries, Figures 4.7-4.18).

By late-afternoon (2300 UTC), subsidence prevailed over the network in the lower levels (Figures 4.24 (d) and (e)). In the mid-levels (Figure 4.24 (a), (b), and (c)), strong subsidence was prevalent over northern sections, while ascent began to develop in the area of Mountaineer Lodge. The Mountaineer Lodge soundings at 2205 UTC and 0011 UTC (Figures 4.25 (a) and (b)), indicate the development of a deep dry adiabatic layer (from the surface to 700 mb). At 2205 UTC, a distinct stable layer is apparent between 700 and 600 mb; however, by 0011 UTC, that stable layer has been removed (via cooling), while the lower levels continued to warm through diabatic heating. In the synoptic scale diagnosis, the author found no evidence of any dynamic features that would support this type of vertical motion; in fact, the general conclusion was that synoptic scale subsidence would be expected to prevail over the southern half of the network.

The early evening (0100 UTC, July 12) analyses indicate the re-establishment of ascent over northwestern sections (Figure 4.26). It is noteworthy that north of the LIMEX-85 network, a second "wave" of thunderstorms was developing along the foothills at the same time. The persistent orographic subsidence at Limestone Mountain Ridge was maintained while further to the south, conspicuous vertical motion was analyzed at Mountaineer Lodge. The 0011 UTC and 0206 UTC tephi-grams for Mountaineer Lodge (Figure 4.25 (b) and (c)) indicate a deep dry adiabatic

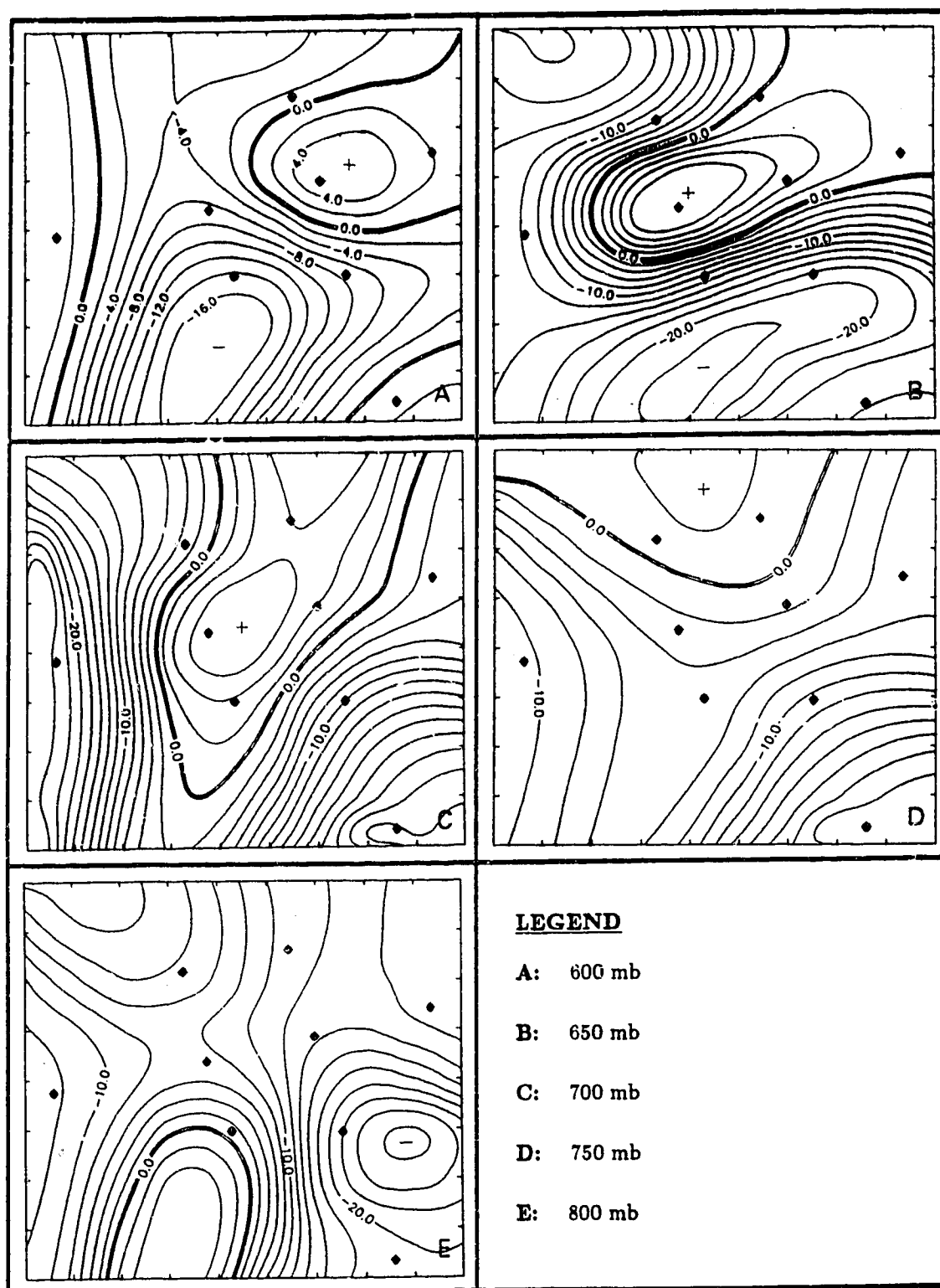


Figure 4.23: Mesoscale vertical velocity fields for 2100 UTC (1500 MDT) July 11, 1985. Contours are in intervals of  $2 \text{ cm s}^{-1}$ . The indicated grid length is 25 km.





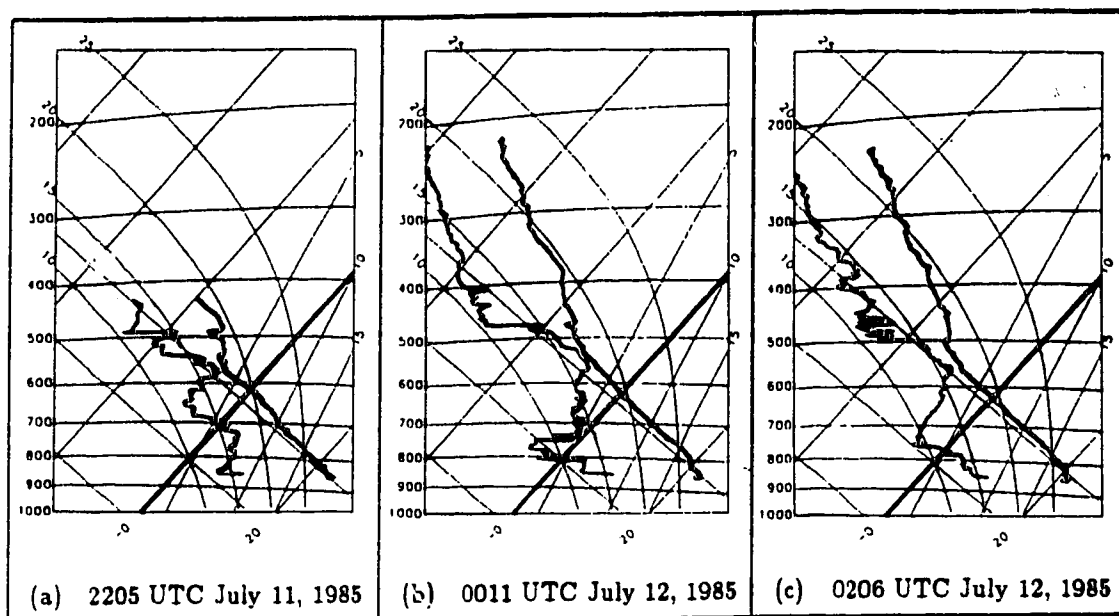


Figure 4.25: Serial soundings from Mountaineer Lodge (CAML) illustrating the removal of a shallow stable layer between 700 and 600 mb.

layer from near the surface to the 600 mb level. As noted in Chapter 3, the accuracy of the adiabatic technique is significantly impaired when applied to such soundings.

The late morning (1700 UTC) spatial mesoscale objective analysis of the 800 mb vertical velocity is shown in Figure 4.20. A relatively strong band of subsidence appears in the lee of the Rockies, stretching from Calgary to Mountaineer Lodge to Limestone Mountain to west of Ram Lookout then northwestward. Weak ascent appears over the northwest corner of the LIMEX-85 analysis region at both Rocky Mountain House and Red Deer.

The subsidence appears to result primarily from orographic downslope flow from the great mountain barrier which starts a few kilometres west of the Limestone Mountain and Mountaineer Lodge sites. The ascent in the eastern portion of the



grid is believed to be an extension of the synoptic scale ascent from the trough over eastern Alberta (Figure 4.2).

During late-morning, (1700 UTC), the orographic subsidence in the lee of the mountains is stronger at 750 and 700 mb (Figures 4.20 (c) and (d)). Computed values of subsidence at Limestone Mountain and at Mountaineer Lodge, for instance, exceed  $25 \text{ cm s}^{-1}$ . Meanwhile, the ascent in the northwest corner of the grid also appears to have intensified. Above 700 mb, the orographic subsidence weakens (Figure 4.20 (b)) and virtually disappears well above mountain elevations at 600 mb (Figure 4.20 (a)). At this level, most terrain-induced vertical motions are lost, and weak ascent prevails, as one might infer from the general synoptic pattern (Figures 4.1–4.3).

By early afternoon (1900 UTC), subsidence still prevails over the mountains. The validity of the 800 mb analysis (Figure 4.22 (e)) over the northwest corner of the grid is questionable as the data for Ram Lookout (CARL) were not available. The strong subsidence that was prevalent in that area just 2 hours prior to this analysis, has weakened considerably. It may be that surface heating by this time has initiated enough convection currents so as to modify the pattern of orographic subsidence over some areas in the northwest portion of the grid. In any event, subsidence has intensified at 750–600 mb over the southwest corner of the grid (Figures 4.22(a)–(d)).

Meanwhile, a cell of weak ascent has emerged at low- to mid-levels between Caroline (CACR) and Elkton (CAEL), with a line of weak ascent extending towards the north (800 mb, Figure 4.22 (e)) or northwest (750 mb, Figure 4.22 (d)) from this

cell. The cell of ascent is confined to lower levels, below the capping lid, but further northwest the ascent extends to well above 650 mb. Lines of convective clouds without radar echoes were observed and photographed in this region at this time (G. Strong, personal communication). A major convective storm commences to the northwest at or shortly after this time, and moves just inside the radar-detectable range northwest of Rocky Mountain House at 2200 UTC (Figure 4.7).

By mid-afternoon (2100 UTC), the weak 800 mb ascent that was prevalent in the Caroline - Elkton region at 1900 UTC (Figure 4.22 (e)) has been replaced by widespread subsidence. This dramatic change may be due, in part, to the effects of solar heating. From the serial soundings shown in Figure 4.27, it is apparent that the capping lid was gradually removed, likely by weak ascent and adiabatic cooling. By mid-afternoon, the time of maximum daytime heating, the lower-levels of the sounding indicated warming, likely due to the strong daytime heating rather than to strong subsidence.

At the mid-levels, 700–600 mb (2100 UTC), a distinct cell of positive vertical motion was centred over the observation network between Limestone Mountain Ridge and Caroline (Figures 4.23 (a)–(c)). It is interesting to note that this is the approximate location in which the storms eventually developed (see PPI summaries, Figures 4.12–4.18). This tends to support the hypothesis presented by Strong (1986) that positive vertical motion develops in the lower-troposphere up to six-hours prior to the storm event. The presence of strong positive vertical motion at the 600 mb level suggests that the main dynamic feature involved here is the upper level jet (which appears to lie directly over this region (see Figures 4.1 and 4.4)).

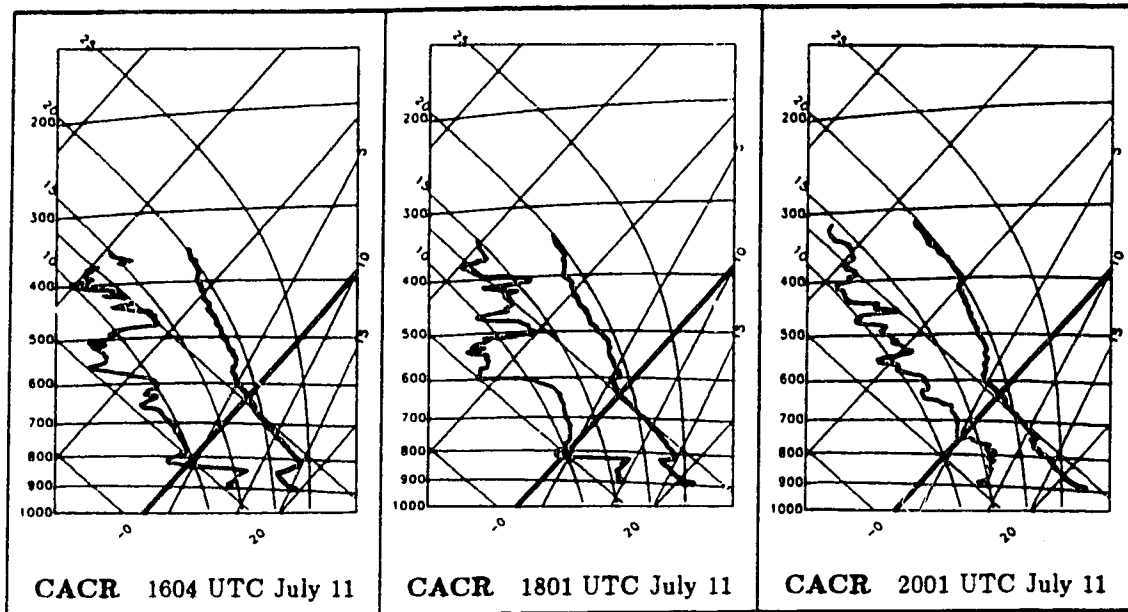


Figure 4.27: Serial soundings from Caroline (CACR) for 1604, 1801, and 2001 UTC illustrating the evolution of the capping-lid.

In the late-afternoon (2300 UTC), subsidence continued to prevail over the analysis region at the 800–750 mb levels (Figure 4.24 (d) and (e)). Meanwhile, in the mid-levels (700–600 mb, Figures 4.24 (a), (b), and (c)), the positive vertical motion that was prevalent between Limestone Mountain Ridge and Caroline on the previous analyses (Figures 4.23 (a), (b), and (c)), has been replaced by strong subsidence. The author is somewhat perplexed in trying to explain the reason for this strong “band” of subsidence. It is analyzed from Red Deer to Caroline with a maximum between Limestone Mountain Ridge and Ram Lookout. It appears to have continuity in the vertical to the 600 mb level, and is dominating the region in which the thunderstorms developed one hour later (see PPI summaries, Figures 4.12–4.18).

Meanwhile, another notable change from the previous analyses is the positive

vertical velocity at Mountaineer Lodge ( $9 \text{ cm s}^{-1}$  at 650 mb and  $14 \text{ cm s}^{-1}$  at 600 mb), see Figures 4.24 (a) and (b). The cell of strong vertical motion analyzed south of Mountaineer Lodge is likely bogus. The strong gradient between Limestone Mountain ( $-13 \text{ cm s}^{-1}$  at 650 mb and  $-15 \text{ cm s}^{-1}$  at 600 mb) and Mountaineer Lodge cannot be discounted; however the subsidence maximum along the southern border of the analysis network appears to be a spurious feature associated with the lack of data in that region.

By early evening (0100 UTC, July 12), an intense thunderstorm was moving eastward over northern sections of the LIMEX-85 network (see PPI summaries, Figures 4.12–4.18). At the time, the spatial vertical motion field appeared quite complicated (Figure 4.26). (Due to missing data, the author was not able to calculate the vertical velocity at Ram Lookout, Mountaineer Lodge, and Elkton at the 800 mb level). At 0100 UTC, positive vertical motion has re-established itself over the northwest sections of the analysis region at all levels above 800 mb. Strong orographic subsidence persists in the Limestone Mountain area, and equally strong ascent persists at Mountaineer Lodge.

#### 4.5.1 Summary

This limited study of the vertical motion field over the LIMEX-85 network has revealed two interesting points:

- as suggested as a possibility by Strong (1985, 1986), mesoscale ascent has been found to be present in the lower-atmosphere up to six hours prior to the storm event;

- the orographic subsidence in the immediate lee of the Rockies can be extremely strong (exceeding  $25 \text{ cm s}^{-1}$ ); this strong subsidence is a major contributing factor to the development and maintenance of the capping lid;

In the following section, the author will diagnose the meso-beta 800 mb divergence fields.

#### **4.6 Meso-beta 800 mb Divergence Fields**

The late-morning (1700 UTC) and early afternoon (1900 UTC) 800 mb divergence fields are characterized by the presence of a strong convergence cell centre between Limestone Mountain Ridge and Caroline (see Figures 4.28 (a) and (b)). It is interesting to note that the 700 and 650 mb vertical velocity fields at 2100 UTC indicate ascent over this same area.

By mid-afternoon (2100 UTC), the cell of convergence appears to have shifted southwestward to the vicinity of Mountaineer Lodge (see Figure 4.28 (c)). It seems to remain quasi-stationary in that area for the remainder of the analysis period (see Figures 4.28 (d) and (e)). This persistent convergence may have been partly responsible for the strong ascent that developed at Mountaineer Lodge in the early evening (see Figures 4.24–4.26), though it is difficult to verify such a claim.

#### **4.7 Meso-gamma Surface Divergence Fields**

Analysis of the mesoscale surface divergence fields was performed using surface observations from seven of the nine upper air sites, five automatic surface sites, and 22 A.E.S. surface stations. Of the 22 A.E.S. surface stations, only 4 were in the

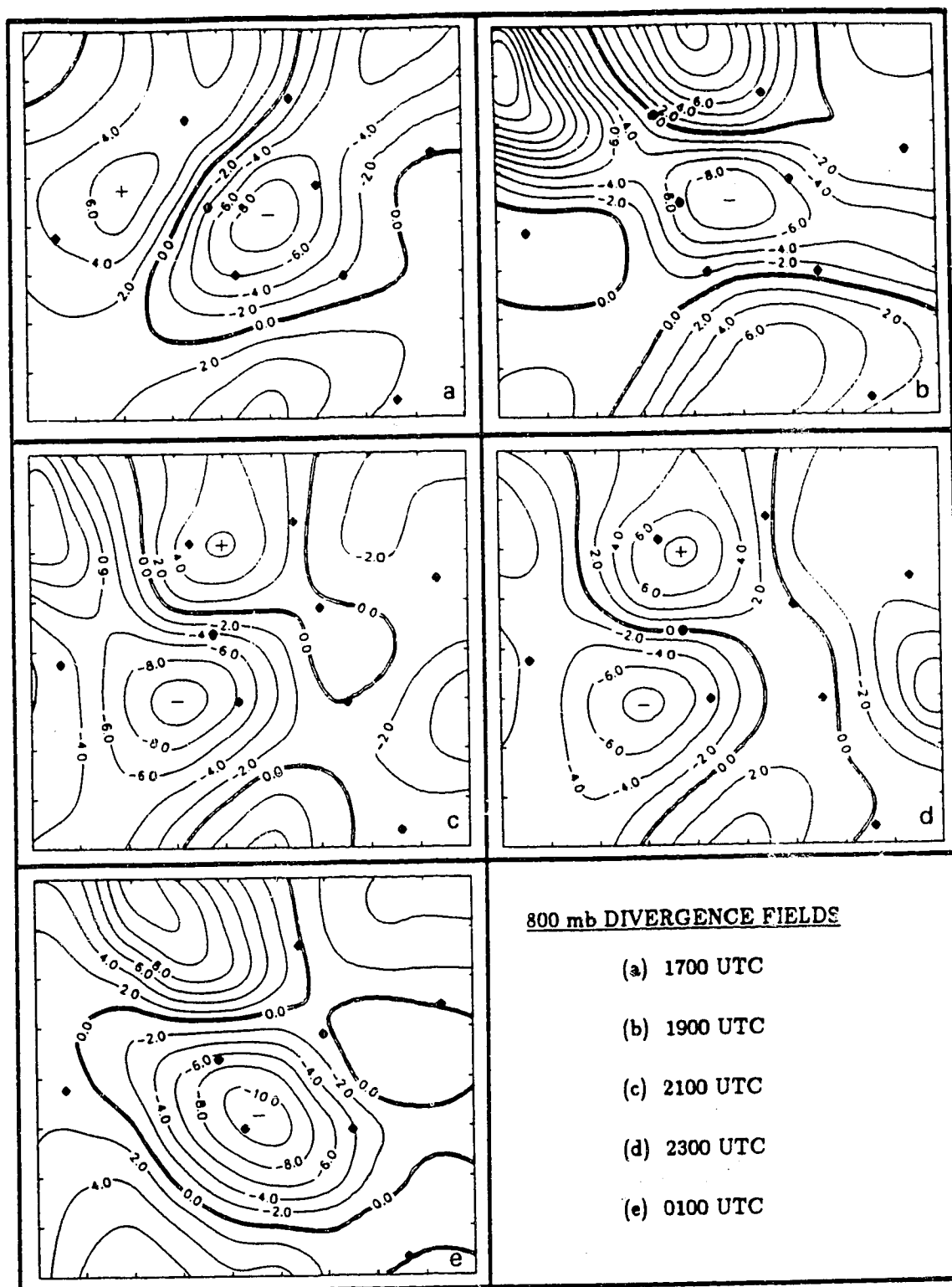


Figure 4.28: Spatial objective analysis of the 800 mb divergence fields valid 1700 UTC (1100 MDT) July 11 to 0100 UTC July 12, 1985. Contours are in intervals of  $3 \times 10^{-5} \text{ s}^{-1}$ . The indicated grid length is 25 km.



LIMEX-85 mesoscale network. The remaining stations were included to influence the border points of the objective analysis grid.

The meso- $\gamma$  surface divergence fields, from 1700–2300 UTC (Figures 4.29 (a)–(d)), are characterized by a strong “line” of convergence that extends from the northwest corner of the grid to Limestone Mountain Ridge to Mountaineer Lodge and thence southeastward. It is interesting to compare the position of this strong “line” of convergence with the 2134 UTC visible satellite image (see Figure 4.19 (c)). The satellite image clearly indicates a band of cumuliform cloud in the region of strong surface convergence.

When one compares these analyses with the topography of the area (see Figure 2.1), it becomes apparent that the line of convergence (and band of cumuliform cloud) developed over the foothills in the immediate lee of the Rockies. This tends to support previous work by Barker and Banta (1984, 1985), who have hypothesized that in mountainous terrain, zones of convergence occur on the leeward side of mountain ranges where the upslope airflow encounters well-mixed downslope flow at the surface. Barker and Banta found that zones of convergence precede the development of convective storms, and concluded these zones were the regions of thunderstorm initiation. The LIMEX-85 data set appears to support their hypothesis.

By 0100 UTC, the objective analysis indicates a significant change in the area of Ram Lookout. This may be due, in part, to a missing data point southwest of Ram Lookout (Ram Falls Ranger Station ARF). The apparent lee side convergence, that prevailed for the previous six hours, is no longer evident. In its place, a



divergence cell now appears between Ram Lookout and Caroline, while a strong cell of convergence remains in the Limestone Mountain - Mountaineer Lodge area. It could also be argued that the developing thunderstorms between Rocky Mountain House and Caroline (see Figure 4.13) may be generating a mesoscale divergence field in its wake (associated with its strong down drafts).

#### **4.7.1 The Utility of Existing Sub-Synoptic Data Sources**

To determine the utility of standard operational surface weather sites, the author performed the following analyses. First the mesoscale surface divergence for 1700 UTC 11 July was calculated using all available LIMEX-85 data (see Figure 4.29 (a)). Then, the author used only the regular Alberta Forestry and AES data and re-calculated the surface divergence for the same time. The objective analysis of this existing sub-synoptic data is shown in Figure 4.30 (b). It is noteworthy that all but one of the LIMEX-85 surface stations that were omitted in Figure 4.30 (b), were "inside" the existing sub-synoptic data network. The omission of this single station (CABP-Bow Pass) along the western border of the analysis grid, appears to have had a significant effect on the surface divergence field in that area. Elsewhere, the omission of the remaining LIMEX-85 stations had little effect on the overall pattern.

A subjective comparison of the high density data analysis with the existing sub-synoptic data analysis reveals some interesting points. Though the analysis using the existing sub-synoptic data set appears unrefined, it continues to contain the same general information that the high density analysis contains. Strong con-

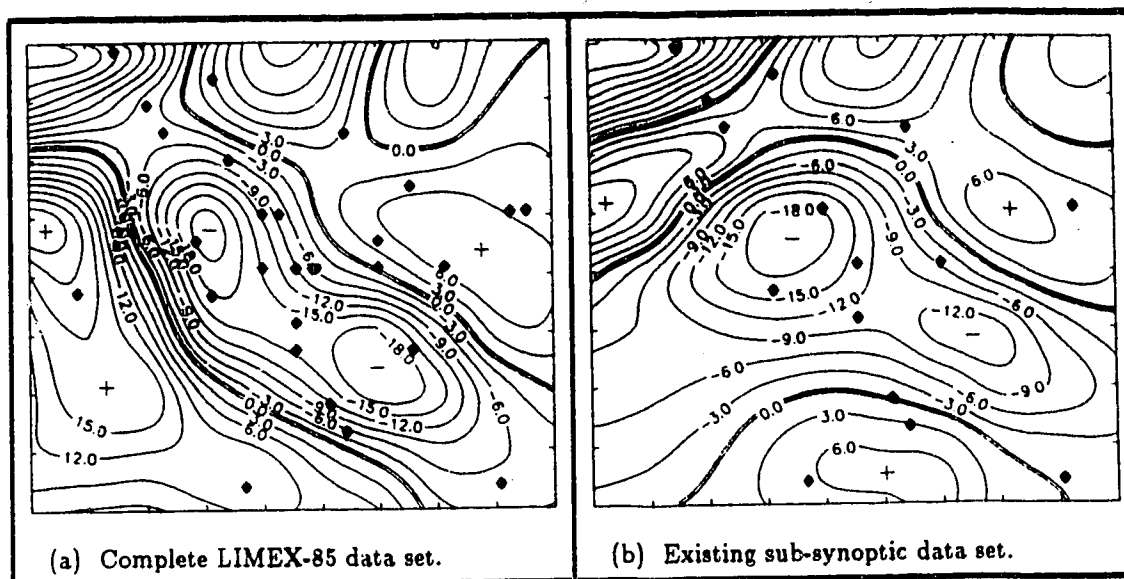


Figure 4.30: Comparison of surface divergence fields using (a) the high density LIMEX-85 data set, and (b) existing operational AES and Alberta Forestry data. Contours are in intervals of  $3 \times 10^{-5} \text{s}^{-1}$ . The indicated grid length is 25 km.

vergence is evident in the Limestone Mountain area, with a line of convergence extending east-southeastward. The divergence cell west of Red Deer is still clearly defined and of the same magnitude. The overall pattern is quite similar to the high density analysis. The gradients are not as intense and the maximum values not as high, but the analysis contains useful information.

#### 4.7.2 Summary

This limited study of the surface divergence field over the LIMEX-85 network revealed several interesting points:

- as suggested by Barker and Banta (1984, 1985), mesoscale surface convergence develops along the leeward side of mountain ranges and tends to precede the initiation of thunderstorms;

- the “line” of strong surface convergence along the lee side of the Rockies displays temporal continuity throughout the analysis period;
- the apparent correlation of surface convergence “cells” with “cells” of positive vertical motion does not appear very strong.

## **Chapter 5**

# **Conclusions and Recommendations**

### **5.1 Summary and Conclusions**

The purpose of this research was to utilize surface and upper air mesoscale data, collected during the Limestone Mountain Experiment (1985), to accomplish several objectives. The following conclusions may be drawn:

1. The temporal and spatial evolution of the vertical motion field in the pre-thunderstorm environment was diagnosed. Though the study was limited to one day, the initial results indicate the presence of strong positive vertical motion five hours prior to the storm event. The cellular structure of the positive vertical velocity fields displayed spatial continuity, however with the exception of a single 2 hour period, temporal continuity appeared to be lacking.

The general magnitude of subsidence in the lee of the Rocky Mountains was clearly illustrated. Strong subsidence appeared to “hug” the leeward side of the Rockies, especially during the morning hours (before diabatic heating affected the lower levels significantly). The mid- and upper-level synoptic flow was particularly conducive to the strong orographic subsidence observed.

2. The surface and 800 mb divergence fields displayed reasonably good temporal continuity. The most conspicuous feature was the strong surface convergence in the immediate lee of the Rockies. The high density analysis, at 1900 UTC, clearly defined a strong convergence line along the foothills. This result verified the previous works of Barker and Banta (1984, 1985), who hypothesized that zones of convergence develop on the leeward side of mountain ranges.

The 800 mb divergence analyses indicated strong convergence centred over the LIMEX-85 region early in the day. However, this pattern appeared to have poor spatial and temporal continuity later in the analysis period.

The presence of strong surface convergence along the lee side of the Rocky Mountains tends to support the premise that links surface convergence with initial thunderstorm development. The S-band radar initially detected the developing thunderstorms west and southwest of Rocky Mountain House. It is reasonable to assume that these cells initially developed upstream of the position where the first echoes were observed. This leads one to conclude that the thunderstorms may have originally developed as cumulus cloud over the area of strong surface convergence (along the lee slopes of the Rockies). However, it is difficult to ascertain the region of initial development. The 2034 UTC satellite photo supports this scenario, showing a band of cumuliform cloud developing along the lee slopes of the Rocky Mountains early in the day.

3. The author performed a rigorous, yet limited examination of the importance of the advection term in the adiabatic method of calculating vertical velocity.

The results support the assumption made by Strong (1986) that the advection term is relatively insignificant in weakly baroclinic environments.

4. A cursory look at the operational utility of existing sub-synoptic data sources had an interesting outcome. Initial results indicate that the Alberta Forestry weather data could be used to obtain a rough, yet useful, analysis of surface divergence fields in the lee of the Rockies. Though the Alberta Forestry and AES surface data lack the detail and resolution of the high density LIMEX-85 data set, it was possible to use this low resolution data to resolve the strong surface convergence over the foothills.

## 5.2 Recommendations

Further research could be focused in the following areas:

- The role of the capping lid in the development of severe thunderstorms has been documented by Strong (1986), and Chen (1982). One of the primary goals of the LIMEX-85 was to diagnose the mesoscale dynamics of the pre-thunderstorm environments of Alberta hailstorms, with special emphasis on the creation, breakdown, and role of the capping lid.
- Performing an objective comparison of the adiabatic and kinematic techniques of computing vertical velocity could enhance further diagnostic studies. This could involve applying a new method of determining vertical velocities from series radiosonde data as outline by Ragette (1985). It could also involve calculating the terrain-induced vertical velocity and using that as a boundary



condition for the kinematic technique.

- Exploring the reliability of surface divergence fields calculated from existing sub-synoptic data sources. The study could also investigate problems and deficiencies with existing operational data networks.
- Examining the numerical methods of spatially analyzing mesoscale data. The method applied in this study has some obvious problems in data sparse regions. Perhaps the analysis scheme could be improved to rectify this problem.

## Bibliography

- [ ] Barker, C.L. and R.M. Banta, 1984: The role of mesoscale convergence in convective cloud initiation in mountainous terrain. *Preprints, 10<sup>th</sup> Conf. on Wea. Forecasting and Analysis*. Amer. Meteor. Soc., 555-558.
- [ ] Barker, C.L. and R.M. Banta, 1985: Preferred regions of thunderstorm initiation over the Colorado Rockies. *Preprints, 14<sup>th</sup> Conf. on Severe Local Storms*. Amer. Meteor. Soc., 17-20.
- [ ] Barnes, S.L., 1964: A technique for maximizing details in numerical weather map analysis. *J. Appl. Meteor.*, 3, 396-409.
- [ ] Barnes, S.L., 1973: Mesoscale objective analysis using weighted time-series observations. NOAA Tech. Memo. ERL NSSL-62, 60 pp. [NTIS COM-73-10781].
- [ ] Barnes, S.L., 1976: Severe local storms: concepts and understanding. *Bull. Amer. Meteor. Soc.*, 57, 412-419.
- [ ] Berggren, R., W.J. Gibbs, and C.W. Newton, 1958: Observational characteristics of the jet stream. A survey of the literature. WMO, TN No. 19.
- [ ] Bluestein, H.B., 1984: Fronts and Jet Streaks: A Theoretical Perspective. School of Meteor., Univ. of Oklahoma, Norman, Okla., 59 pp.
- [ ] Byers, H.R. and R.R. Braham, 1949: The thunderstorm. Final Report, Dept. Meteor., Univ. Chicago, Chicago, Ill., 287 pp.
- [ ] Chen, P., 1982: Summer Severe Weather Correspondence Course. Atmospheric Environment Service, Downsview, Ontario (mailing address: 4905 Dufferin St., Downsview, Ont. M3H 5T4).
- [ ] Cotton, W.R., R.L. George, P.J. Wetzell, and R.L. McAnelly, 1983: A long-lived mesoscale convective complex. Part I: the mountain-generated component. *Mon. Wea. Rev.*, 111, 1893-1918.
- [ ] Doneaud, A.A., J.R. Miller, D.L. Priegnitz, and L. Viswanath, 1983: Surface mesoscale features as potential storm predictors in the northern great plains: two case studies. *Mon. Wea. Rev.*, 111, 273-292.
- [ ] Doswell, C.A., 1987: The distinction between large-scale and mesoscale contribution to severe convection: a case study example. *Weather and Forecasting*, 2, 3-16.
- [ ] Emanuel, K.A., 1986: Overview and definition of mesoscale meteorology. In *Mesoscale Meteorology and Forecasting*. Edited by P.S. Ray. Amer. Meteor. Soc., Boston, 1986. 1-17.
- [ ] Fankhauser, J.C., 1969: Convective processes resolved by a mesoscale rawinsonde network. *J. Appl. Meteor.*, 8, 778-798.

- [ ] Field Program Report 1985, Atmospheric Sciences Dept., Alberta Research Council. Ed. R. Deibert. Edmonton Alberta.
- [ ] Fuelberg, H.E., and W.S. Lee, 1982: A comparison of adiabatic and kinematic vertical motions using mesoscale data. *Preprints, 9<sup>th</sup> Conf. on Weather Forecasting and Analysis*. Amer. Meteor. Soc., 417-423.
- [ ] Fujita, T.T., 1981: Tornadoes and downbursts in the context of generalized planetary scales. *J. Atmos. Sci.*, 38, 1512-1534.
- [ ] Fujita, T.T., 1986: Mesoscale classifications. In *Mesoscale Meteorology and Forecasting*. Edited by P.S. Ray. Amer. Meteor. Soc., Boston, 1986. 18-35.
- [ ] Galway, J.G., 1956: The Lifted Index as a predictor of latent instability. *Bull. Amer. Meteor. Soc.*, 37, 528-529.
- [ ] George, J.J., 1960: *Weather Forecasting for Aeronautics*. Academic Press, New York, p. 407.
- [ ] Goldstein, M.G., 1976: Severe storm development and the importance of differential advection. Ph.D. Thesis, New York University, 70 pp.
- [ ] Hadley, G., 1735: Concerning the cause of the general trade-winds. *Philosophical Transactions*, Royal Society of London, 29, 58-62.
- [ ] Harwood, R.S., 1981: Atmospheric vorticity and divergence. In *Dynamical Meteorology*, Ed. B.W. Atkinson. Methuen, New York, 228 pp.
- [ ] Henz, J.F., 1973: Characteristics of severe convective storms on Colorado's High Plains. *Preprints, 8<sup>th</sup> Conf. Severe Local Storms*, Denver, Amer. Meteor. Soc., 96-103.
- [ ] Hobbs, P.V., 1981: Mesoscale structure in midlatitude frontal systems. In *Nowcasting: Mesoscale observations and short-range prediction*. Proceedings of an International Symposium, 25-28 August, Hamburg, Germany, 29-36.
- [ ] Holton, J.R., 1979: *An Introduction to Dynamic Meteorology*. Academic Press, New York, 391 pp.
- [ ] Huschke, R.E., 1959: *Glossary of Meteorology*. Amer. Met. Soc., Boston, Mass., 638 pp.
- [ ] Iribarne, J.V. and W.L. Godson, 1981: *Atmospheric Thermodynamics*, Second Edition. D. Reidel Publishing Co., Boston, Mass., 259 pp.
- [ ] Ligda, M.G.H., 1951: Radar storm observations. In *Compendium of Meteorology*, American Meteorological Society, Boston, 1265-1282.
- [ ] McNulty, R.P., 1985: A conceptual approach to thunderstorm forecasting. *National Wea. Digest*, 10, 26-30.
- [ ] Miller, A. and H.A. Panofsky, 1958: Large-scale vertical motions and weather in January, 1953. *Bull. Amer. Meteor. Soc.*, 39, 8-13.
- [ ] Miller, R.C., 1972: Notes on analysis and severe weather forecasting procedures of the Air Force Global Weather Central. AFGWC Tech. Rep. 200 (rev.).
- [ ] Moore, J.T., 1985: The effect of diabatic heating/cooling on vertical motions in the severe storm environment. *Preprints, 11<sup>th</sup> Conf. Weather Forecasting and Anal.* Amer. Meteor. Soc., 211-216.

- [ ] Orlanski, I, 1975: A rational subdivision of scales for atmospheric processes. *Bull. Amer. Meteor. Soc.*, 56, 527-530.
- [ ] Palmén, E., and C.W. Newton, 1969: *Atmospheric Circulation Systems*. Academic Press, New York, 603 pp.
- [ ] Pedder, M.A., 1981: On the errors of kinematic vertical motion estimation using divergence bias adjustment procedures. *Mon. Wea. Rev.*, 109, 1813-1816.
- [ ] Petterssen, S., 1956: *Weather Analysis and Forecasting, Vol. I, Motion and Motion Systems*. McGraw-Hill Book Co., Toronto, 428 pp.
- [ ] Ragette, G., 1985: A new method of determining vertical velocities from series radiosonde data. *Arch. Meteor. Geoph. and Biocl., Ser. A* 34, 159-166.
- [ ] Reiter, E.R., 1961: *Jet-Stream Meteorology*. Univ. of Chicago Press, Chicago, 515 pp.
- [ ] Richardson, L.F., 1922: *Weather Prediction by Numerical Process*. Cambridge University Press, London, 236 pp. Reprinted by Dover.
- [ ] Rossby, C.-G., 1942: The scientific basis of modern meteorology. *Climate and Man*, Yearbook of Agriculture for 1941, U.S. Government Printing Office, Washington, D.C.
- [ ] Sikdar, D.N., and Fox, D., 1983: An evolving severe storm complex during SESAME: its large scale environment and momentum budget. *Preprints, 19<sup>th</sup> Conf. on Severe Local Storms*. Amer. Meteor. Soc., 312-315.
- [ ] Sampson, R.J., 1978: *Surface II Graphics System (Revision One)*. Kansas Geol. Survey, Lawrence, Kan., 240 pp.
- [ ] Showalter, A.K., 1953: A stability index for thunderstorm forecasting. *Bull. Amer. Meteor. Soc.*, 34, 250-252.
- [ ] Sly, W.K., 1964: A convective index as an indicator of cumulonimbus development. *J. Appl. Meteor.* 5, 839- 846.
- [ ] Strong, G.S., 1985: The Limestone Mountain Experiment, July 1985 (LIMEX-85). Part 1: Scientific planning: hypothesis and objectives. Unpublished document. Resource Technologies Dept., Alberta Research Council, Edmonton, Alberta, Mar. 1985, 10 pp.
- [ ] Strong, G.S., 1986: Synoptic to Mesoscale Dynamics of Severe Thunderstorm Environments: A Diagnostic Study with Forecasting Applications. Ph.D. thesis, Univ. of Alberta, Edmonton, Alberta, 345 pp.
- [ ] Strong, G.S. and W.D. Wilson, 1983: The Synoptic Index of Convection: Part I. Evaluation of the single-valued index, 1978-1982. Presented at 17<sup>th</sup> Annual Congr. Can. Meteor. and Oc. Soc., Banff, Alberta, 03-05 May, 1983, published by Alberta Research Council, Edmonton, 27-37.
- [ ] Tucker, G.E., 1973: Vertical velocities and vertical eddy fluxes derived from serial soundings at one station. *Quart. J. Roy. Meteor. Soc.*, 99, 520-539.
- [ ] Ulanski, S.L. and M. Garstang, 1978: The role of surface divergence and vorticity in the life cycle of convective rainfall. Part I: observation and analysis. *J. Atmos. Sci.*, 35, 1047-1062.

- [[ Verlarde, M.G., and C. Normand, 1980: Convection. *Scientific American*, 243, 92-108.

## Appendix A

### Assessment of Spatial Analysis Scheme

#### A.1 Method

Following a suggestion made by the examining committee, the author designed a scheme to subjectively assess the credibility of the mesoscale objective map analysis routine used in this study. The method simply involved applying the objective analysis routine on a “known” topographic surface. The routine’s ability to interpolate the “known” or “actual” topography from irregularly spaced station data points on that topography could thus be observed. This assessment scheme involved several steps which are listed below.

1. Grid point data were generated from the following sinusoidal equation:

$$f(x, y) = 10 \sin \left( \frac{n \pi x}{l} \right) \sin \left( \frac{n \pi y}{m} \right), \quad (\text{A.1})$$

where  $l$  is the number of grid points in the x-direction,  $m$  is the number of grid points in the y-direction, and  $n$  is a parameter to be varied<sup>1</sup>. In this study,  $l = 10$ ,  $m = 9$ , and the grid spacing was set at 25 kilometres.

2. The equation was solved for  $x = 1$  to  $l$  and  $y = 1$  to  $m$ . This resulted in a two-dimensional array containing data for each grid point. The gridded data

---

<sup>1</sup> A series of different topographic surfaces are generated as  $n$  is varied. When  $n = 1$ , a single dome, or “maximum cell”, is generated over the grid network. When  $n = 2$ , two “maxima cells” and two “minima cells” are generated, etc.

were then contoured using the SurfaceII Graphics System (Sampson, 1978), resulting in a topographic map of the surface. These contoured fields are hereafter referred to as the “actual” data fields.

3. Equation (A.1) was then solved using the  $x$  and  $y$  grid locations of the irregularly spaced LIMEX-85 surface and upper air stations, as indicated in Figure 2.1. This resulted in a data set that contained the station values of the given topographic surface.
4. The derived station data values were then used by the objective analysis routine to generate a two-dimensional array containing data for each grid point. That is, the mesoscale objective analysis routine “interpolated” the grid point values from the irregularly spaced station data values. The gridded data were then contoured and are hereafter referred to as the “interpolated” data field.
5. Several different “topographic” surfaces were generated by allowing  $n$  to vary ( $n = 1, 2, 3, \dots$ ). The “interpolated” data fields were then analyzed using a variety of values for the radius of influence ( $R$ ) in the objective analysis routine. This was done to subjectively determine a reasonable radius of influence with which to analyze the LIMEX-85 data.
6. The “actual” data fields were then visually compared with the “interpolated” data fields.

## A.2 Results

The initial spatial analysis of the actual gridded data, derived from the sinusoidal equation (equation (A.1)) using  $n = 1$ , is shown in Figure A.1 (a). This dome-shaped topography, centred over the analysis network, was then compared to several different “interpolated” analyses. Figure A.1 (b) is the topographic surface that was generated using the high density surface data network to interpolate the gridded data. In this particular case, a radius of influence of two grid units was used<sup>2</sup>. Figures A.1 (c)-(f) are the contoured topographic surfaces that were “interpolated” from the low-resolution upper air station data points. These analyses indicate two interesting points.

1. The analysis scheme is unable to properly resolve the “known” topographic surface in the data sparse regions. The scheme has distinct difficulties in three data sparse regions: the northwest corner, the southern border south of Mountaineer Lodge, and the eastern border between Red Deer and Calgary.
2. As the radius of influence is varied<sup>3</sup>, the accuracy of the objective analysis scheme varies. When  $R = 1$ , (see Figure A.1 (c)), the analysis is extremely poor in data sparse regions. As the radius of influence is increased,  $R = 2$  and  $R = 3$ , the analysis gradually improves along the borders (see Figures A.1 (d) and (e)). However, as the radius of influence is further increased ( $R = 4$  in Figure A.1 (f)), the scheme begins to spuriously sharpen the ridg-

---

<sup>2</sup> The author experimented by using several different values for the radius of influence and found that  $R = 2$  gave the best results.

<sup>3</sup> When interpolating the gridded data from the irregularly spaced station data points, the author used 10 different values for the radius of influence ( $R$ ). The analyses shown in this appendix are for  $R = 1, R = 2, R = 3$ , and  $R = 4$  grid units.



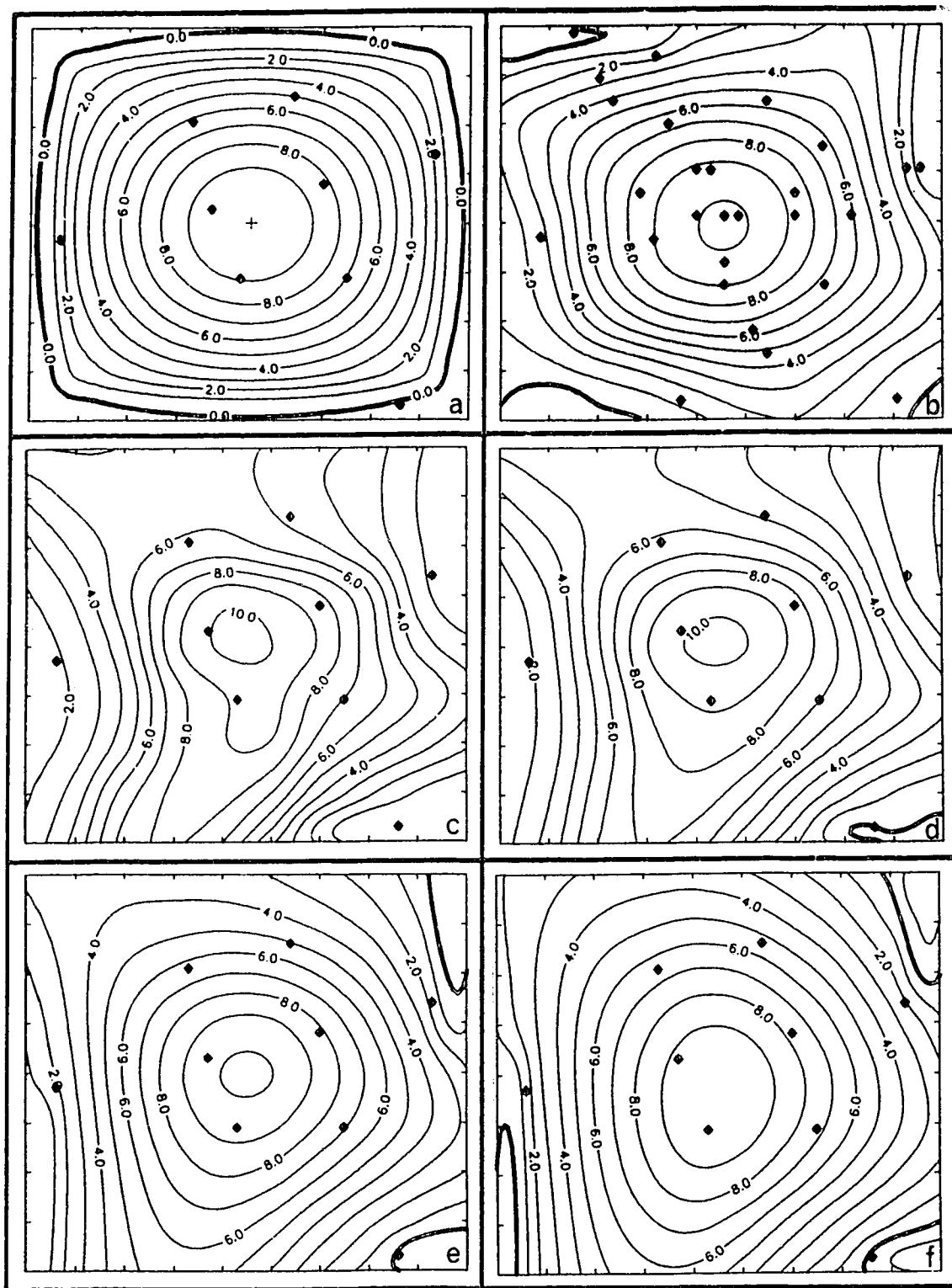


Figure A.1: Spatial analysis of equation (A.1) with  $n = 1$ ,  $l = 10$ , and  $m = 9$ . Legend: a: actual gridded data, b: high-resolution data with  $R = 2$ , c: low-resolution data with  $R = 1$ , d: low-resolution data with  $R = 2$ , e: low-resolution data with  $R = 3$ , f: low-resolution data with  $R = 4$ .

ing south of Mountaineer Lodge. As the radius of influence was increased to  $R = 5$  and  $R = 6$ , the ridging from the centre of the dome increased more and more into the data sparse regions.

The second spatial analysis was derived from the sinusoidal equation using  $n = 2$ . The contoured fields are shown in Figure A.2. The "actual" data field is a couplet of "maxima" and "minima" as shown in Figure A.2 (a). Using a radius of influence of two grid units, the objective analysis scheme was able to clearly resolve the two minimum centres in the northwest and southeast quadrants of the analysis network (see Figure A.2 (b)). The two maxima in the southwest and northeast east quadrants were also resolved, but were not as well defined. This lack of definition is likely due to insufficient data to accurately resolve the features in those quadrants.

Based on these initial findings it becomes apparent that the low-resolution data, which only contains the nine upper air stations, lacks the necessary density to resolve the detail of the actual data field. There appears to be good definition of the minima cells in the northwest and southeast quadrants, and reasonably good definition of the maximum cell in the northeast quadrant. However, due to the lack of data in the southwest quadrant, the objective analysis scheme has distinct difficulty resolving the maximum in that quadrant. Notice that as the radius of influence is increased, the scheme seems to interpolate extreme values into the data sparse regions. That is, in the absence of control points, the analysis scheme spuriously interpolates maximum or minimum values with each pass.

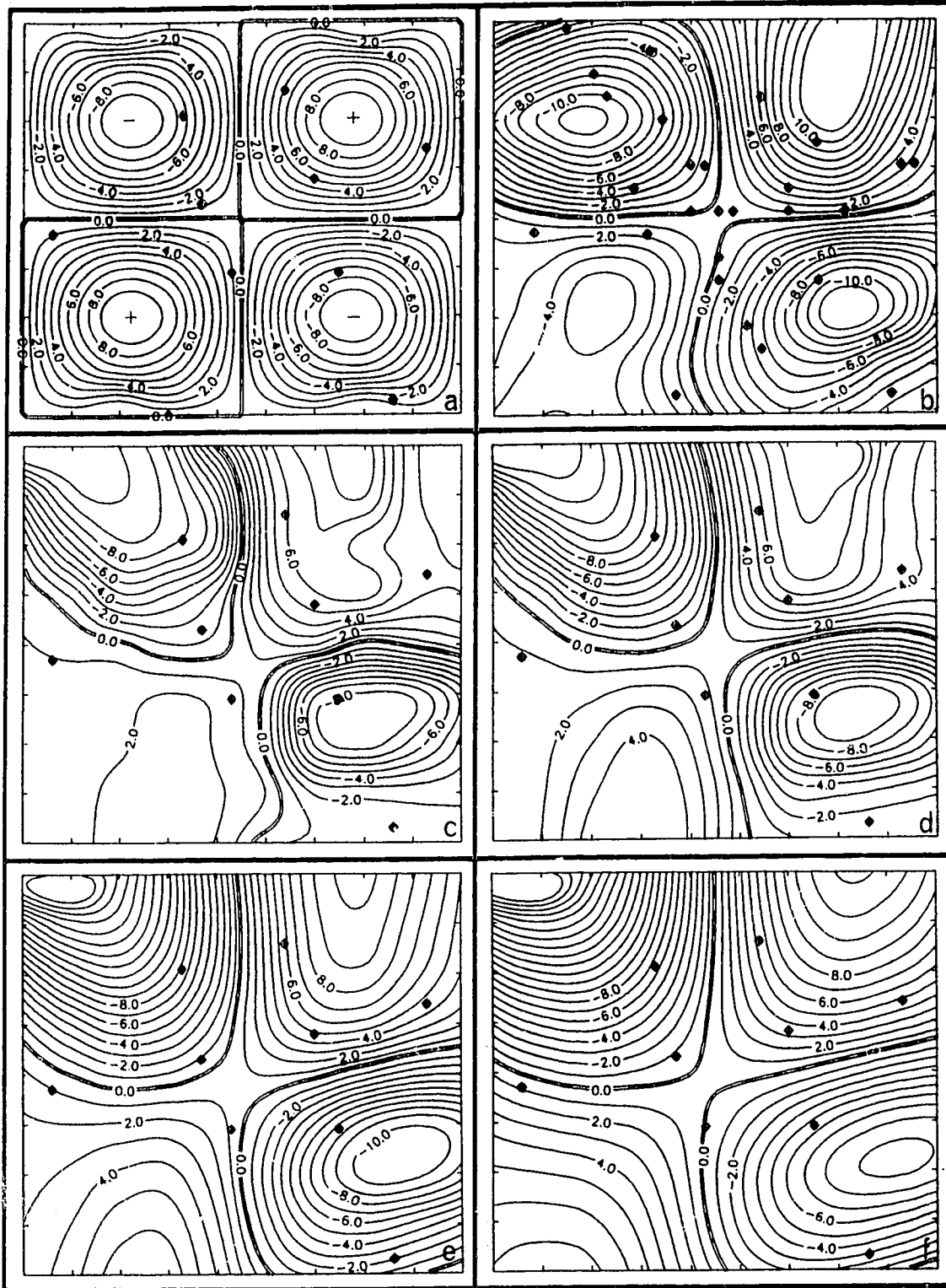


Figure A.2: Spatial analysis of equation (A.1) with  $n = 2$ ,  $l = 10$ , and  $m = 9$ . Legend: a: actual gridded data, b: high-resolution data with  $R = 2$ , c: low-resolution data with  $R = 1$ , d: low-resolution data with  $R = 2$ , e: low-resolution data with  $R = 3$ , f: low-resolution data with  $R = 4$ .

The ability, or inability, of the low-resolution data to resolve small scale features ( wavelength less than 150 km ) is indicated in Figure A.3. With an average upper air station spacing of 50 to 60 kilometres, one would expect to be able to resolve wavelengths as small as 120 kilometres, provided that the data had reasonable coverage over all regions of the analysis grid. However, it is quite apparent from the map of the mesoscale network (Figure 2.1) that distinct data sparse regions exist. Consequently, the routines ability to resolve features as small as 120 kilometre is questionable. The spatial analyses shown in Figure A.3 were performed using  $n = 3$  in the sinusoidal equation. In order to accurately resolve the complicated cellular structure of the "actual" data field (see Figure A.3 (a)), one would require several station data points strategically placed in each maximum and minimum "cell". The nine upper air station data points are obviously insufficient, as reflected the analyses shown in Figures A.3 (c)–(f). The analysis scheme is able to resolve the maximum cell centred over the analysis grid, while the minima to the east and north of the central cell are only partially resolved. In the remaining areas, the analysis scheme was unable to ascertain the location or intensity of the individual cells; however, there do appear to be "hints" of their existence.

In sharp contrast, the high-resolution surface data was capable of resolving the maxima-minima cellular structure in all but the extreme southwest corner<sup>4</sup> of the analysis grid. The high resolution data produced stronger gradients which allowed the analysis scheme to interpolate maxima in regions where there were no control points.

---

<sup>4</sup> This data sparse region of the LIMEX-85 data network is a mountainous, wilderness area. The research team found that it was not feasible to deploy and operate data instruments in this region.

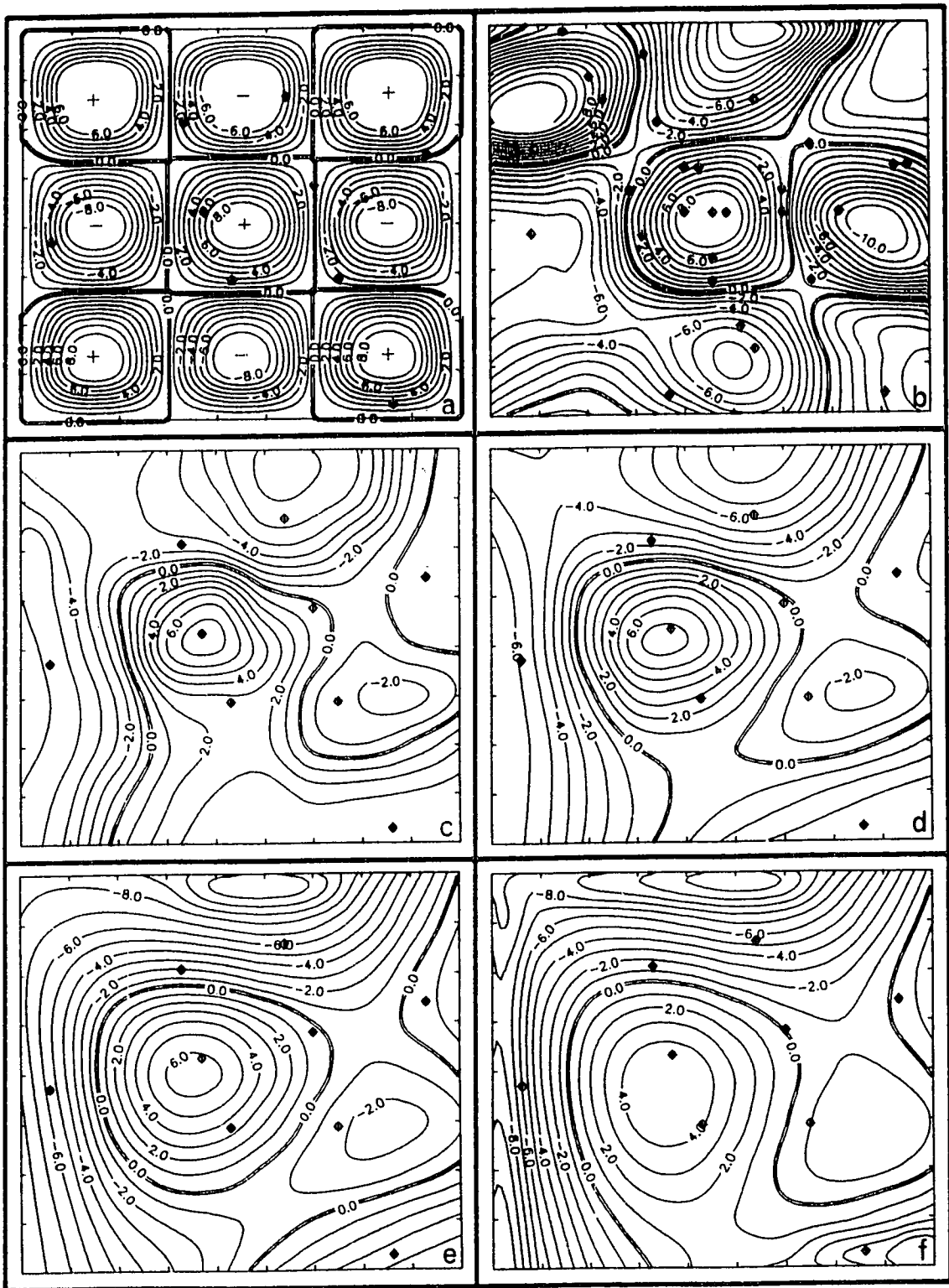


Figure A.3: Spatial analysis of equation (A.1) with  $n = 3$ ,  $l = 10$ , and  $m = 9$ . Legend: a: actual gridded data, b: high-resolution data with  $R = 2$ , c: low-resolution data with  $R = 1$ , d: low-resolution data with  $R = 2$ , e: low-resolution data with  $R = 3$ , f: low-resolution data with  $R = 4$ .

### A.3 Conclusions

Though a rigorous statistical diagnosis of the analysis scheme may have enhanced the results, it was found to be beyond the scope of this study. The key points ascertained from this cursory subjective assessment are listed below.

- For the LIMEX-85 data set, a radius of influence of two grid units appeared to produce the most faithful objective analyses<sup>5</sup>.
- The low-resolution upper air data network was able to resolve features with wavelengths of 150 km and larger over central portions of the analysis grid. The ability of the analysis scheme was to resolve features over other portions of the analysis grid was limited by the lack of control points in those regions.
- The high-resolution surface data network appeared to handle features with wavelengths of 150 km and larger throughout all but the extreme southwest corner of the analysis grid.
- Unfaithful analyses were produced in regions with no control points.
- Conclusions regarding the output fields should be restricted to central portions of the analysis grid where the objective analysis scheme has some credibility.

Based on these findings it is reasonable to conclude that the mesoscale vertical velocity fields analyzed over central portions of the analysis grid are faithful (provided that the wavelength of the feature is greater than 120 to 150 km).

---

<sup>5</sup> It is interesting to note that the station spacing of the upper air network was approximately two grid units.